11-2023

Computational Methodology for Generating Patient-Specific Soft Tissue Representations

Ahilan Anantha Krishnan

Computational Methodology for Generating Patient-Specific Soft Tissue Representations

Abstract

This dissertation focused on modeling specimen-specific soft tissue structures in the context of joint replacement surgery. The research addressed four key aspects. The first study involved developing a workflow for creating finite element models of the hip capsule to replicate its torque-rotational response. Experimental data from ten cadaveric hips were used to calibrate the models, resulting in improved accuracy and relevance for surgical planning and implant design. The second study tackled the challenge of expediting the calibration of mechanical properties of the hip capsule to match patient-specific laxities. A statistical shape function model was proposed to generate patient-specific finite element models, demonstrating potential for instant modeling and potential use in improving outcomes in hip arthroplasty. The third study involved developing a computational model of an experimental knee simulator for simultaneous evaluation of tibiofemoral and patellofemoral mechanics. The model's predictions were verified against experimental measurements, providing a reliable computational tool for further studies. The fourth study investigated the influence of soft tissue balance and implant congruency on knee stability during daily activities. Finite element models were calibrated based on experimental data, perturbed for varying soft-tissue imbalance levels, evaluated for stability during the activities of daily living, thereby highlighting the impact of implant design on stability. The dissertation's findings contribute to the knowledge of surgical planning, implant design, and potentially enhancing outcomes in joint replacement surgeries.

Document Type

Dissertation

Degree Name

Ph.D.

First Advisor

Chadd Clary

Second Advisor

Daniel Linseman

Third Advisor

Paul Rullkoetter

Keywords

Biomechanics, Patient specific, Soft tissue, Surgical planning, Total hip replacement, Total knee replacement

Subject Categories

Biomechanical Engineering | Biomechanics and Biotransport | Biomedical Engineering and Bioengineering | Engineering | Mechanical Engineering

Computational Methodology for Generating Patient-Specific Soft Tissue Representations

A Dissertation

Presented to

the Faculty of the Daniel Felix Ritchie School of Engineering and Computer Science

University of Denver

In Partial Fulfillment

of the Requirements for the Degree

Doctor of Philosophy

by

Ahilan Anantha Krishnan

November 2023

Dr. Chadd Clary

Author: Ahilan Anantha Krishnan
Title: Computational Methodology for Generating Patient-Specific Soft Tissue Representations
Advisor: Dr. Chadd Clary
Degree Date: November 2023

ABSTRACT

This dissertation focused on modeling specimen-specific soft tissue structures in the context of joint replacement surgery. The research addressed four key aspects. The first study involved developing a workflow for creating finite element models of the hip capsule to replicate its torque-rotational response. Experimental data from ten cadaveric hips were used to calibrate the models, resulting in improved accuracy and relevance for surgical planning and implant design. The second study tackled the challenge of expediting the calibration of mechanical properties of the hip capsule to match patient-specific laxities. A statistical shape function model was proposed to generate patient-specific finite element models, demonstrating potential for instant modeling and potential use in improving outcomes in hip arthroplasty. The third study involved developing a computational model of an experimental knee simulator for simultaneous evaluation of tibiofemoral and patellofemoral mechanics. The model's predictions were verified against experimental measurements, providing a reliable computational tool for further studies. The fourth study investigated the influence of soft tissue balance and implant congruency on knee stability during daily activities. Finite element models were calibrated based on experimental data, perturbed for varying soft-tissue imbalance levels, evaluated for stability during the activities of daily living, thereby highlighting the impact of implant design on stability. The

dissertation's findings contribute to the knowledge of surgical planning, implant design, and potentially enhancing outcomes in joint replacement surgeries.

ACKNOWLEDGMENTS

I would like to express my deepest gratitude to my advisor, Dr. Chadd Clary, for his guidance, support, and expertise throughout the entire process of conducting this research and my entire journey in grad school. From writing multiple internship recommendations to offering invaluable research feedback, his support has been immense in navigating through the program.

I am thankful to my lab member and colleague, Yashar Behnam, for his hard work and sharing his research related to all the knee-related experiments. I would also like to thank Michael Scinto and Brittany Marshall for generously sharing their valuable research on hip. This dissertation would not have come to fruition without their experimental work.

I would like to extend my sincere appreciation to the individuals who generously donated their bodies to science. Their contribution was paramount in acquiring the cadaveric study data used in these experiments.

I am grateful to Depuy Synthes for funding this research, enabling its successful completion.

Lastly, I want to express my heartfelt appreciation to all the researchers and previous lab members whose work served as a foundation for this dissertation. I would like to thank Dr. Casey Myers and Dr. Don Hume for their models, codes, and invaluable research feedback, which greatly contributed to this work.

I am truly grateful for the collective support and encouragement I have received, and I acknowledge that this work would not have been possible without the contributions of all those mentioned, as well as the many others who have influenced my academic journey.

TABLE OF CONTENTS

LIST OF FIGURES

CHAPTER 1

CHAPTER 3

CHAPTER 4

CHAPTER 5

CHAPTER 6

LIST OF TABLES

CHAPTER 6

CHAPTER 1. CLINICAL IMPLICATIONS OF PATIENT-SPECIFIC SOFT TISSUE MODELS FOR JOINT REPLACEMENT

1.1 Background

Predicted total annual counts for Total Hip Arthroplasty (THA) in the United States by 2025, 2030, and 2040 are (in thousands): 652, 850, and 1429, respectively, and for primary Total Knee Arthroplasty (TKA), predicted total annual counts 2025, 2030, and 2040 are (in thousands): 1272, 1921, and 3416, respectively (Singh et al., 2019). These projections highlight the importance of understanding joint replacement mechanics to aid in patient care. Both in the hip and knee joints, ligaments are crucial in providing stability and maintaining joint integrity. An accurate understanding of the function of ligaments during and post-surgery is essential for improving surgical outcomes, optimizing implant designs, and enhancing patient-specific treatment planning (Aunan et al., 2015; Victor et al., 2005; Jiang et al., 2016). This section aims to provide a background of the current research, methodologies, and challenges associated with patient-specific modeling of ligaments in the knee and hip in the context of joint replacement surgery.

Ligaments are tough, fibrous connective tissues that connect bones and provide stability to the knee and hip joints (Fu et al., 1993; Martin et al., 2008). The knee joint consists of four dominant ligaments: the anterior cruciate ligament (ACL), posterior

cruciate ligament (PCL), medial collateral ligament (MCL), and lateral collateral ligament (LCL) in addition to ancillary structures (Figure 1.1a). On the other hand, the hip joint is supported by several ligaments, including the iliofemoral ligament, ischiofemoral ligament, and pubofemoral ligament (Figure 1.1b). In the natural joint, these ligaments act as passive restraints, restraining joint motion within physiological limits, helping distribute the forces and loads encountered during joint movement, supporting the surrounding structures, and reducing stress on articular surfaces. However, joint replacement surgery is reported to alter the ligament function leading to changed joint kinematics in both hip (van Arkel et al., 2018) and knee joints (Emodi et al., 2019; Yue et al., 2012).

The success of joint replacement surgery relies on achieving optimal joint stability and function (Rivière et al., 2019; Courtney et al., 2017). However, the ligamentous structures and their properties can vary significantly among individuals due to age, sex, activity level, and individual anatomy (Schleifenbaum et al., 2016). Considering these subject-specific factors, the unique biomechanical response of ligaments in different individuals can be better understood, especially in developing computational models. For instance, Ali et al. developed specimen-specific finite element models of intact and ACL-deficient knees (Ali et al., 2017). When predicting kinematics, they report model accuracy with average RMSE of 3.0° and 2.1° in rotations, and 1.7 and 2.5 mm in translations. Baldwin et al. developed specific-specific soft tissue representations of three cadaveric knees. Their simulated and experimental differences were less than 1.8 mm and 2.2° for patellofemoral (PF) and tibiofemoral (TF) translations and rotations (Baldwin et al., 2012). Patient-specific modeling of ligaments can be a practical approach to evaluating surgical outcomes and

personalizing treatment planning. However, patient-specific biomechanical modeling can be an intensive process, as outlined in Figure 1.2.

One aspect of the modeling is gathering accurate geometry corresponding to the patient. Various imaging modalities, including magnetic resonance imaging (MRI) and computed tomography (CT), enable capturing patient-specific ligament geometries. Recently, several image segmentation and processing techniques were developed and reported in the literature to extract ligament attachment sites and geometries from the acquired imaging data. In particular, Statistical Shape Modeling (SSM) and machine learning techniques have emerged as valuable tools for capturing inter-subject variations in patient geometry. SSM creates a statistical representation of the shape variability within a population, enabling the generation of personalized ligament models based on a limited training data set. For instance, Oevelen et al. developed a statistical shape function model to derive the knee's soft tissue geometry from bone geometry (Oevelen et al., 2023). Pillet et al. used a similar approach to predict the ligament attachment sites in the knee with an average accuracy of 3.3±1.5 mm and 5.8±2.9 mm for femoral and tibial/fibular attachment sites, respectively (Pillet et al., 2016). Thus, patient-specific information was proven in the literature as vital to develop patient-specific ligament representations.

Subject-specific modeling goes beyond subject-specific considerations and incorporates inter-subject variations in ligament properties as appropriate material properties are crucial for accurately representing its behavior. Ligament properties can be obtained from cadaveric studies, previous literature, or experimental testing of ligament samples (Galbusera et al., 2014). In some cases, inverse optimization techniques were used to estimate material properties based on experimental or clinical data (Beidokhti et al.,

2017). In addition, statistical algorithms were employed to learn patterns and relationships from a large dataset, allowing for ligament properties based on joint response prediction. For instance, Razu et al. used neural networks coupled with Bayesian optimization to predict ACL properties from knee kinematics (Razu et al., 2023).

Validating patient-specific ligament models is paramount for building confidence in their prediction (Erdemir et al., 2012). Validation involves comparing model predictions with in vivo measurements or data from biomechanical experiments. Measurements using force sensors and joint kinematics analysis validate the ligament models and ensure their applicability (Papaioannou et al., 2008; Ali et al., 2016). Once validated, patient-specific ligament models could find potential applications, including pre-operative planning, implant selection, implant positioning, capsule preservation-reconstruction, implications for post-surgery joint performance, and understanding the interplay between ligament function and implant design/function (Clary et al., 2013; Halloran et al., 2005; Elkins et al., 2011). Studies exploring these areas either have a limited scope of application (lack of generalizability), use population-averaged data, lack proper model validation techniques, need more time to develop, or need a more streamlined workflow to integrate them into the pre- or intra-operative surgical decision-making. Going forward, the term ‘subject’ describes cadaveric data/ details and distinguishes it from live patients.

1.2 Objective and Chapter Overview

Given the potential benefits, opportunities for incorporating patient-specific models must be explored that could enable their use in joint replacement surgeries. To facilitate that goal, this dissertation aims to streamline the subject-specific model development

process and validate the models. In addition, it aims to validate a knee-simulator model and demonstrate its utility in evaluating surgical conditions. The abovementioned goals are thus condensed into the following studies:

Study 1: Chapter 2 develops a generic representation of an implanted hip capsule and calibrates it to subject-specific laxity data. In addition, it aims to streamline the workflow to calibrate ten specimens and validate the models by predicting their dislocation response. In addition, it underscores the structure-function relationship of the capsular structure.

Study 2: Chapter 3 addresses the major limitation from Specific Aim 1: the time required to develop specimen-specific models. This aim used statistical shape function and regression modeling to expedite development of specimen-specific models. These expedited models were tested and validated against cadaveric laxity data.

Study 3: Chapter 4 develops a finite element model of a knee simulator, which will be used as a computational testbed for evaluating different implant designs and conditions. The study replicated the simulator in a deep knee bend activity for various patella positions and validated the model against TF, PF kinematics, and PF joint loading.

Study 4: Chapter 5 develops four specimen-specific models of the implanted knee calibrated to varus-valgus and anterior-posterior laxities. The knees were virtually implanted with TKA of varying congruity and then the implant alignment was altered to change the ligament balance. The effects of ligament balance on knee stability were assessed during three different activities of daily living.

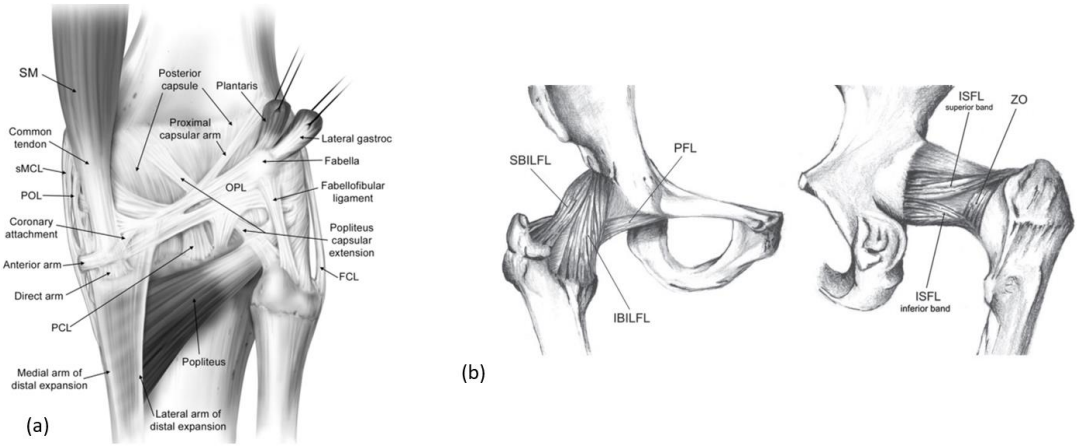

Figure 1.1: (a) Posterior aspect of the knee after removal of medial and lateral gastrocnemius muscles and neurovascular structures (LaPrade et al., 2007) (b) anterior and posterior views of the articular capsule of the hip, displaying the capsular ligaments as distinct bands reinforcing the capsule (Wagner et al., 2012; (CLH = capsular ligaments of the hip, IBILFL = inferior band of the iliofemoral ligament, ILFL = iliofemoral ligament, ISFL = ischiofemoral ligament, PFL = pubofemoral ligament, SBILFL = superior band of the iliofemoral ligament, ZO = zona orbicularis).

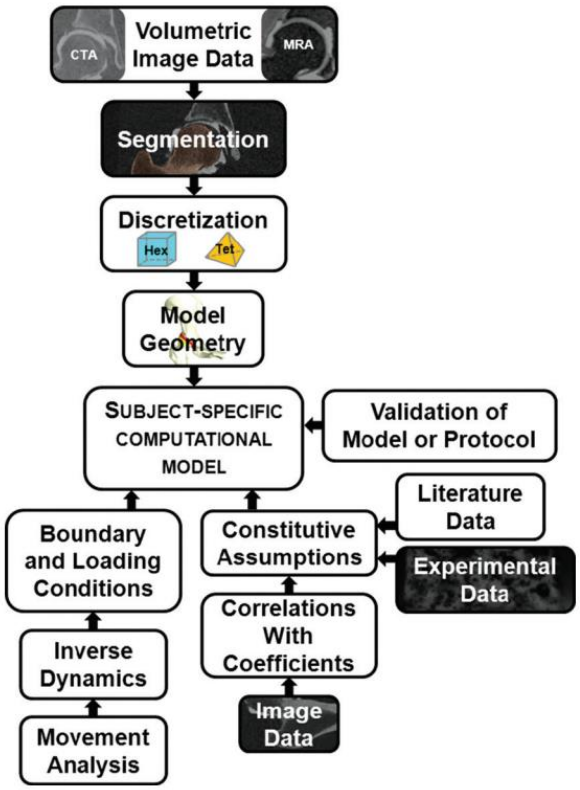

Figure 1.2: High-level overview of methods for generating subject-specific computational models (Henak et al., 2013).

CHAPTER 2. LITERATURE REVIEW

This chapter aims to provide a literature review on the subject-specific modeling of ligaments. Understanding the biomechanical behavior of ligaments through subject-specific modeling will lead to improved diagnosis, treatment, and prevention of ligament-related injuries.

2.1 Anatomy and Biomechanics of Ligaments

2.1.1 Ligaments of the Hip

The hip joint is reinforced by three main fibrous capsular ligaments: iliofemoral, ischiofemoral, and pubofemoral (Martin et al. 2008). Each ligament has distinct functional roles in stabilizing the joint (Martin et al. 2008, Ng et al. 2019). The iliofemoral ligament consists of lateral and medial fibrous branches, forming an inverted Y-shaped structure (Figure 1.1 b). It reinforces the capsule during external rotation and extension (Ambrosi et al. 2021). The ischiofemoral ligament reinforces the capsule during internal rotation and neutral positions (Ng et al. 2019) (Figure 1.1 b). The pubofemoral ligament restricts excessive abduction and external rotation during hip extension (Martin et al. 2017) (Figure 1.1 b). The triangular-shaped ligamentum teres reinforces between the inferior acetabular notch and the fovea of the femoral head, playing a critical role in proprioception and structural stability (Ng et al. 2019) (Figure 1.1 b). The circular fibers of the zona

orbicularis, along with the longitudinal fibers of the primary capsular ligaments, contribute to stability by closing around the femoral neck (Bedi et al. 2011) (Figure 1.1 b). The zona orbicularis was also found to facilitate the circulation of synovial fluid within the capsule (Malagelada et al. 2015).

2.1.2 Ligaments of the knee

The ACL originates in the intercondylar notch and inserts on the intercondylar eminence (Goldblatt et al. 2003, Bowman et al. 2010). It consists of the anteromedial and posterolateral bundles, although the existence of an intermediate bundle is still debated. Tension in these bundles varies depending on the flexion angle, with the anteromedial bundle tighter in extension and the posterolateral bundle tighter in flexion (Amis et al. 1991). The ACL wraps upon itself, increasing tension as the tibia rotates internally. It plays a role in preventing hyperextension and primarily resists anterior translation, particularly at around 20° flexion (Unwin et al. 2010). The ACL also guides tibial rotation during knee extension and couples translation to tibial axial rotation.

The PCL originates on the medial surface of the intercondylar notch and inserts on the proximal tibia in the fovea centralis (Goldblatt et al. 2003, Bowman et al. 2010). Its insertion is anterior to the posterior extent of the femoral and tibial condyles, aligning with the posterior cortex of the femur and tibia (Bowman et al. 2010). The specific attachment sites of the PCL on the femur and tibia vary between individuals, with the femoral footprint averaging 209 mm^2 (Bowman et al. 2010) The PCL has two bundles: a posteromedial bundle and an anterolateral bundle. The posteromedial bundle is taut in extension, while the anterolateral bundle is taut in flexion (Bowman et al. 2010). Internal rotation of the

tibia causes these bundles, as well as the ACL, to wrap upon themselves, which can be tested using 90-degree anteroposterior drawer tests (Bowman et al. 2010). The ligaments of Wrisberg and Humphry connect the PCL to the posterior attachments of the lateral meniscus (Cho et al. 1999). In full extension, the PCL serves as the primary restraint against translation and coronal plane rotation (Bowman et al. 2010).

The medial compartment of the knee was reported to have three layers, namely the superficial, middle, and deep layers (Goldblatt et al. 2003, Bowman et al. 2010, LaPrade et al. 2015). The superficial layer contains the sartorius muscle and deep fascia, while the middle layer includes the superficial MCL, posterior oblique ligament, medial PF ligament, medial patellar retinaculum, and semimembranosus (Warren et al. 1979). The deep compartment consists of the deep MCL, the knee joint capsule, and the coronary ligaments. The MCL, which is the largest structure on the medial aspect of the knee joint, has two components: the superficial MCL located in the middle layer and the deep MCL in the deep layer (Hassebrock et al. 2020). Superficial MCL originates near the medial epicondyle and has two distinct insertions on the tibia. The deep MCL is divided into the meniscotibial and meniscofemoral portions, connecting the meniscus to specific points on the tibia and femur. Collectively, the three key static stabilizers in the medial aspect of the knee (sMCL, dMCL, and the POL), provide support against abnormal valgus motion, rotation, and translation in the knee (LaPrade et al. 2015).

The lateral aspect of the knee is also composed of superficial, middle, and deep layers (Goldblatt et al. 2003, Bowman et al. 2010, Hassebrock et al. 2020). The superficial layer consists of the iliotibial band and biceps femoris. The middle layer is made up of the lateral PF ligament and lateral patellar retinaculum. The deep layer includes the lLCL,

fabellofibular ligament, popliteus tendon, politeofibular ligament, joint capsule, and arcuate ligament. The knee joint relies on several lateral structures to maintain stability and control movement. The iliotibial (IT) tract and its interaction with the biceps fascial communication contribute to stabilizing the lateral compartment of the knee and preventing varus rotation (Flato et al. 2017). In addition to its role as an extensor, the IT band acts as a static stabilizer when the knee is fully extended. As the knee flexes, the IT band tightens and moves backward to maintain tension throughout the range of motion (Flato et al. 2017).

Another important component of knee stability is the LCL, which primarily restrains varus stress at all flexion angles (Bowman et al. 2010). It also acts as a secondary restraint to external rotation and posterior translation. When the knee is in full extension, the LCL resists approximately 55% of the varus load. Furthermore, the popliteofibular ligament plays a dominant role in resisting external rotation during knee flexion, while the LCL provides additional support (Shahane et al.1999). When the posterolateral structures of the knee are sectioned, there is an increase in posterior translation and external rotation, especially between 0° and 45° of flexion, affecting the posterior limit of translation. This highlights the importance of these structures in controlling knee stability during various ranges of motion. Additionally, the fabellofibular ligament experiences the most tension in full extension and likely plays a significant role in maintaining knee extension. The popliteus complex also assumes a crucial role in the knee joint's stability. Positioned in the posterolateral corner, it acts as a dynamic internal rotator of the tibia and a static restraint against posterior tibial translation, varus rotation, and primary and combined external rotation of the tibia on the femur (Kaplan et al. 1961). The popliteus effectively prevents

tibial external rotation during flexion and varus rotation, contributing to overall knee stability (Nyland et al. 2005).

2.2 Constitutive Modeling of Ligaments

The ligaments of the knee and other articular joints are composed of a water-rich ground substance reinforced with collagen fibers (Loitz et al. 1993, Frank et al. 2004). This ground substance contains proteoglycans and hyaluronic acid, which attract water and create a gel-like structure. The ligament tissue is assumed to be incompressible due to its ability to maintain a high-water content even when stretched. Fibroblasts within the matrix produce collagen molecules, which provide tensile stiffness and resistance to the tissue. The collagen structure of ligaments is hierarchical, with crimped collagen fibrils that align with the loading direction when stretched, resulting in a characteristic force-elongation curve. Constitutive models (1D/2D/3D) have been developed and reported in the literature to simulate this behavior.

2.2.1 1D Material Model

Line elements such as springs, trusses, and beams are commonly used to represent the mechanical behavior of ligaments especially in the knee joint. The most common approach is to use bundles of line elements that cover the insertion areas of the ligaments. However, some studies have also used single elements to describe each ligamental bundle (Table 2.1). Early numerical models of the knee joint incorporated non-linear elements to capture the force-elongation behavior of the ligaments (Blankevoort et al., 1996). These elements were typically quadratic or quadratic in the toe region combined with linear response.

However, they only accounted for tensile loads and offered no resistance to compression or shear. The material properties of the ligaments reported in various studies show significant variability, especially regarding the reference strain (Table 2.1).

When simulating knee ligaments, knee extension is often considered as the reference state, as the ligaments are already strained and sustaining a tensile load in this position. However, estimating reference strains experimentally is challenging, and assumptions are often made to accurately simulate the initial state of knee extension. The ligaments in the knee not only exert forces on the insertion areas but also exhibit wrapping behavior between themselves or with bones. Some studies have employed techniques to simulate wrapping, while others neglected this phenomenon, which may limit the accuracy of the results, especially when the force distribution and direction are affected (Blankevoort et al. 1991, Beidokhti et al. 2017).

2.2.2 2D/3D Material model

Compared to a simplistic representation, 3D material models offer a more realistic representation of ligaments. MRI scans combined with 3D reconstruction software allow for detailed representations that include ligament geometry and insertion sites specific to each patient (Benos et al. 2020). Combining MRI with CT scans provides high-resolution imaging of the bony structures through registration software. However, simulating ligaments with solid elements has limitations due to their anisotropic and non-compressive mechanical behavior. An intermediate approach combines the ease of implementing 1D elements with realistic anatomy using 3D elements. This involves embedding springs or trusses in a 3D matrix with a simple constitutive law, such as linear isotropic elasticity or

neo-Hooke hyperelasticity (Bischoff et al. 2008). Previous studies utilized 2D elements (shells or membranes) reinforced with non-linear line elements to capture ligament anisotropy (Baldwin et al. 2012). Various continuum material models have been reported, with anisotropic hyperelastic models being commonly used (Table 2.2). Regardless of the complexity, 3D material models enable the simulation of ligament wrapping using surface-to-surface contact, enhancing the accuracy of stress simulation near bone contact and insertion areas.

2.3 Subject-Specific Modeling

Subject-specific modeling of soft tissue structures employed a variety of computational modeling approaches, such as finite element analysis (FEA), multibody dynamics (MBD), and musculoskeletal modeling incorporating individual variations in geometry, material properties, and loading conditions. Regardless of the type of joint, the first step in the subject-specific modeling involves acquiring subject-specific geometry. Subject-specific model geometry can be acquired through both in vitro and in vivo approaches. In vitro methods, such as laser scanning and stereophotogrammetry, provide precise reconstructions but cannot be used on living subjects (Henak et al. 2013). With the progress in volumetric imaging, it has become possible to create intricate computational joint models of living individuals which involve volumetric computed tomography (CT) or magnetic resonance (MR) imaging to obtain subject-specific geometry. CT scanning involves taking a series of radiographic images from different angles around the joint and then reconstructing a 3D image using a computer, while MRI uses a strong magnetic field to create detailed images of the soft tissues including the cartilage, ligaments, tendons, and

other soft tissues surrounding the joint (Henak et al. 2013). Specialized software tools, such as Amira, Mimics, and Seg3D, enable 3D reconstruction of volumetric image data through automatic, semiautomatic, and manual segmentation methods (Wittek et al. 2016). These programs utilize techniques like thresholding, histogram-based segmentation, manual segmentation, decimation, and smoothing to create 3D geometries from 2D layers. An alternative approach to standard segmentation is statistical shape modeling, which could morph the limited subject-specific data to the template to generate high-quality geometry reducing the time required to generate subject-specific models (Heimann et al. 2009).

Subject-specific loading and kinematics can be gathered through instrumented implants, controlled loading apparatus, and motion capture techniques. This involves using infrared cameras with reflective markers, inertial measurement units (IMUs), or video recordings combined with musculoskeletal modeling. Ground reaction forces (GRFs) are recorded using force plates, while muscular activation is captured via electromyography (EMG). Subsequently, inverse kinematics and musculoskeletal modeling are employed to estimate joint motions, moments, contact forces, and muscle forces of the joint. Recently, machine learning techniques have been reported to predict knee loading patterns based on measured variables replacing physics-based modeling. However, obtaining subject-specific data for various physical activities can be time-consuming. So, most studies still use population-averaged kinematics or loading data from open sourced databases like Orthoload (Heinlein et al. 2007).

In contrast to anatomy and kinematics, obtaining in vivo subject-specific ligament mechanical properties is complicated. Therefore, researchers rely on subject-specific geometry and loading data, coupled with a ligament constitutive model, to calibrate model

parameters using an inverse approach. Table 2.2 provides an overview of studies that have developed subject-specific ligament representations for various joints. These studies typically use experimental data from different degrees of freedom (DOFs) and levels of ligament recruitment to fine-tune specific parameters. However, the calibration process, based on matching the data used, does not guarantee generalizability to a broader range of applications. For instance, Kia et al. developed a multibody dynamic model of a cadaveric knee and tuned the ligament parameters to match experimentally measured ligament forces in full extension (Kia et al. 2016). The tuned model was able to predict experimentally measured ligament forces, internal rotation, anterior translation with an accuracy of ≤ 5.7 N, $\leq 1.6°$ and ≤ 0.4 mm across a range of 130° of passive flexion. On the other hand, Harris et al. developed subject-specific finite-element models of cadaveric knees by tuning the ligament stiffness, initial strain, and attachment location, to match experimental laxity data (Harris et al. 2016). Their reported errors between model predictions and experimental results were consistently minimal, with $<2°$ during varus-valgus rotations,$<6°$ during internal-external rotations, and <3 mm of translation during anterior-posterior displacements.

To validate these models, researchers often compare the results with controlled in vitro experiments conducted using setups like the Oxford rig (Zavatsky et al. 1997) or the Kansas Knee Simulator (Maletsky et al. 2005). These setups allow for the application of physiological loads and motions, and the resulting kinematics are then compared with numerical predictions. However, these experimental methods have limitations, as they do not provide direct measurement of strains in the ligaments, limiting the extent of model validation. While sophisticated sensors or optical strain measurements offer a partial

solution to this limitation, they introduce added complexity to the experimental setup. As a result, many studies resort to indirect validation methods, comparing their results with available data from literature or previous experiments (Table 2.2). However, in such cases, researchers have limited control over the quality and variability of the experiments used for comparison, which can affect the overall reliability of the validation process.

2.4 Clinical Applications and Future Perspectives

Several studies in the literature use subject-specific models to understand joint biomechanics, soft tissue damage progression, implant design, and surgical decision-making and planning. Elkins et al. used a subject-specific hip capsule model to represent varying levels of capsule thickness, regional detachment from the capsule's femoral or acetabular insertions, surgical incisions of capsule substance, and capsule defect repairs (Elkins et al., 2011). They used these models to evaluate dislocation resistance and showed that localized defects in the capsule led to varying degrees of compromise in construct stability, with some situations resulting in over 60% reduction in resistance to dislocation. However, well-conceived repairs substantially improved construct stability, bringing it closer to the levels observed in intact capsules. Their study underscored the importance of retaining or robustly repairing capsular structures in THA to maximize overall construct stability. Myers et al. used a calibrated hip capsule model to evaluate the effect of different implant parameters (head diameter, lipped liner, jump distance, and mobility type) on joint stability (Myers et al., 2021). This study's clinical implications reveal that increasing the head diameter of total hip arthroplasty (THA) implants improves resistance to both anterior and posterior dislocation by 22%. Additionally, the use of a lipped liner and a dual-mobility

acetabular design enhances resistance to posterior dislocation by 47% and 38%, respectively, providing surgeons with valuable options to enhance joint stability and reduce the risk of dislocation.

Ali et al. developed and validated subject-specific finite element (FE) representations of the PF joint, enabling the prediction of PF kinematics and quadriceps force in both healthy and pathological knee specimens (Ali et al, 2015). Their study showed cruciate resections led to either increased patellar tendon loads or increased joint reaction force and discussed implications such as raising the risk of cartilage wear and the development of osteoarthritis. Fitzpatrick et al. used a subject-specific model to probabilistically evaluate the effects of implant design, surgical techniques, and component alignment on TF and PF mechanics, including contact mechanics, joint loads, and ligament and quadriceps forces (Fitzpatrick et al., 2012). They found design factors were the primary contributors to condylar contact mechanics and TF anterior–posterior kinematics. TF ligament forces were dependent on surgical factors while joint loads and quadriceps force were dependent on subject-specific factors. Their study demonstrated how robust implant designs and surgical techniques must be to adequately accommodate subject-specific variations. Clary et al. used a calibrated model to virtually implant multiple designs to predict paradoxical anterior femoral slide during a simulated deep knee bend (Clary et al., 2011). They found that incorporating a gradually reducing radius during mid-flexion reduced anterior motion by 21%-68% in simulations and 81% experimentally and demonstrated the use of calibrated models as essential tools in optimizing TKA design and improving implant kinematics.

Recent studies attempted to incorporate machine learning techniques into patient-specific planning. For instance, Twiggs et al. investigated the correlation between

simulated patient-specific postoperative TKA joint dynamics and patient-reported outcomes (Twiggs et al 2021). Their results revealed significant nonlinear relationships between Knee Injury and Osteoarthritis Outcome Score (KOOS) pain score and dynamic coronal alignment as well as rollback. In addition, they identified a "kinematic safe zone" of favorable outcomes, suggesting an optimal target for individual patients' joint dynamics, potentially aiding preoperative alignment decisions to achieve better postoperative KOOS scores. Regardless, given the complexity in terms of computational resources, experimental data, and appropriate subject-specific data, the potential of using subject-specific models in surgical planning and clinical decision-making remains underutilized. This dissertation aims to address some of the challenges faced in this area.

Table 2.1: Variability in the calibrated properties reported for different knee structures (K is the stiffness in N/mm, e is the reference strain, NR = not reported).

Study	MCL	LCL	PCL-PM	POL	PCAP-M	PCAP-L
Kia et al. 2016- Natural Knee	K = 80 e = 1.000	K = 59 e = 0.974	K = 57 e = 0.975	K = 56 e = 0.949	K = NR e = 0.995	K = NR e = 0.989
Harris et al. 2016 – Implanted Knee	MCL K = 122.2 MCLA e = 1.040 MCLM e = 1.047 MCLP e = 1.050	K = 160.5 e = 1.015	K = 59 e = 0.972	K = 48.7 e = 0.915	K = 91.2 e = 1.022	K = 97.5 e = 1.042
Ewing et al. 2015 – Implanted Knee	dMCL e = 0.92 sMCLA = 0.89 sMCLM e = 0.90 sMCLP e = 0.92	LCLA e = 0.98 LCLP e = 0.99	NR	NR	e = 1.14	e = 0.95
Navacchia et al. 2019	dMCL K = 123.2	K = 143.5 e =1.037	NR	K = 70.2 e=1.107	NR	NR

– Natural Knee	sMCLA K = 102.2 sMCLM K = 102.2 sMCLP K = 102.2 dMCL e = 0.992 sMCLA e = 1.012 sMCLM e = 1.055 sMCLP e = 1.020					
Beidokhti et al. 2017 – Natural Knee	aMCL e = 1.033 iMCL e = 1.093 pMCL e = 0.946	aLCL e = 0.770 sLCL e = 0.900 pLCL e = 1.016	e= 1.063	NR	NR	NR

Table 2.2: Literature review of studies reporting subject-specific material properties of ligaments

Joint (Study)	Material Model	Approach	Verification & Validation
Knee (Gardiner et al., 2003)	3D - transversely isotropic hyper elastic material	Direct measurement – uniaxial tensile testing in two directions	Compared against experimental MCL strain during valgus loading
Knee (Kia et al., 2016)	1D – nonlinear springs	Ligament slack length tuned through optimization to match tibial kinematics	Not reported
Knee (Harris et al., 2016)	1D – nonlinear springs	Ligament stiffness and prestrain tuned through optimization to VV, AP, IE laxity test data	Indirect validation through comparison of ligament recruitment patterns reported in literature

Acromioclavicular (Flores et al., 2023)	1D – nonlinear springs	Ligament stiffness and free length tuned through optimization to match joint force-displacement data during distraction	Compared against experimental force-displacement curves for loading by applying IE torque
Lumbar spine – Facet capsular ligaments (Bermel et al., 2020)	3D - ground matrix (neo-Hookean) combined with fiber (exponential strain energy function)	Model parameters tuned to match experimental reaction force during shear loading	Not reported
Cervical spine (Kallemeyn., 2010)	1D – nonlinear springs	Ligament stiffness and prestrain tuned through optimization to match experimental moment–rotation curves	Validation through a combination of literature and specimen-specific test data in multiple DOFs
Knee (Zaylor et al., 2019)	1D – nonlinear springs	ligament slack lengths tuned to match experimental distraction force-displacement data	Indirect validation through comparison of ligament recruitment patterns reported in literature
Hip (Elkins et al., 2011)	3D - Holzapfel-Gasser-Ogden Model	Model parameters tuned to match experimental distraction force-displacement data	Validation by comparing against experimental resisting moment during sit-to-stand dislocation
Knee (Ewing et al., 2016)	1D – nonlinear springs	Ligament stiffness and prestrain tuned through optimization to match experimental moment–rotation curves	Not reported

CHAPTER 3. SPECIMEN-SPECIFIC FINITE ELEMENT REPRESENTATION OF IMPLANTED HIP CAPSULE

3.1 Introduction

Hip stability is inherently provided by the congruent bony anatomy of the femur and acetabulum, but soft tissue structures, including the labrum, ligament capsule, and the surrounding muscles play a key role in preventing hip separation and potential dislocation. After total hip arthroplasty (THA), instability and dislocation are among the primary reasons for revision surgery (Melvin et al. 2014; Badarudeen et al. 2017; Kenney et al. 2019). Several risk factors for hip dislocation have been reported, including surgical approach, implant positioning, soft-tissue balancing, implant head-to-neck ratio, and femoral head diameter (Kunutsor et al. 2019).

THA removes the labrum, alters the native ball and socket anatomy, and changes the natural capsule integrity (van Arkel et al. 2018). Van Arkel et al. reported that reduction of the head diameter from natural to implanted states reduced wrapping of the hip capsule and its ability to restrain extensive rotation. In addition, THA alters the soft tissue fidelity depending on the surgical approach, implant positioning, and repair (Pellicci et al. 1998; Barrack. 2003; Padgett et al. 2004; Takao et al. 2016). Thus, understanding the soft tissue

constraint offered by the hip capsule and changes associated with THA could help improve implant designs and surgical planning to reduce instability and restore natural function.

The hip capsule is a complex ligamentous structure, consisting of the medial and lateral ILFL, the ISFL, and the PFL, that prevents excessive rotation at the hip. The ILFL primarily restrains external rotation (ER) in flexion and both internal rotation (IR) and ER in extension. The ISFL, located posteriorly, primarily restrains IR in flexion and extension. The PFL resists ER in extension with additional support from the ILFL (Martin et al. 2008). Compromising the integrity of the capsule during surgery was reported to alter the kinematics of the joint. Unrepaired T-capsulotomy and capsulectomy were reported to increase the rotational laxity and decrease the distraction force compared to the uncompromised state (Abrams et al. 2015; Khair et al.2017).

Several studies advocate capsule repair after THA to reduce hypermobility, early impingement, subluxation, edge-loading, and dislocation (van Arkel et al. 2015b; Karunaseelan et al. 2021; Suh et al. 2004; Mihalko et al. 2004). Given that capsule repair increases intraoperative time and complexity, many surgeons opt not to repair the capsule. A patient-specific computational model of the capsule could aid surgeons in choosing the proper implant configuration, alignment, and capsular repair technique.

Most previous evaluations of hip capsule biomechanics were performed on cadaveric specimens (Martin et al. 2008, Hidaka et al. 2014, Abrams et al. 2015, Khair et al. 2017, Burkhart et al. 2020). While this testing offers valuable insights, experiments are time consuming and expensive. Further, direct measurement of ligament forces in cadaveric capsules is difficult and unreliable, so studies report metrics like restraint torque, distraction load, and tissue strains. Due to inter-specimen variability, the averaged data

from these studies may not be appropriate for patient-specific surgical planning and intra-operative decision making. In contrast, patient-specific computational models developed directly from experimental laxity data could be used to perform parametric studies of hip mechanics with limited resources and lead to better surgical guidance.

A limited number of studies have developed either specimen-specific or generic computational models of the hip capsule. Elkins et al. represented the hip capsule as a continuous sheath with 27 different material regions in their specimen-specific finite element model of the hip. The properties of the Holzapfel-Gasser-Ogden material model were calibrated to match a single distraction loading curve (Elkins et al. 2011). The tuned model was used to study the effects of thickness variations, suture incisions, and attachment releases on dislocation resistance. Our group has previously developed a probabilistic finite element model of the capsule using parametric non-linear springs embedded in a hyperelastic membrane. Literature-reported averaged torque-rotation data of eight cadavers was used to calibrate the model (Myers et al. 2020). The literature lacks a study that demonstrates a workflow for developing specimen-specific models from specimen-specific anatomy and the corresponding mechanical behavior, which will be necessary for evaluating patient-specific scenarios and surgical guidance.

The current study aimed to develop an algorithmic workflow for building specimen-specific finite element models of the hip capsule for a cohort of ten cadaveric specimens implanted with THA. We used hip capsule geometry created directly from imaging data in an automated fashion and specimen-specific experimental internal-external (I-E) laxity data for calibration. Model predictions were verified during simulated anterior and posterior dislocation loading profiles. To quantify the improved predictive ability of the

specimen-specific models, we compared the specimen-specific predictions to a generic computational representation of the capsule for each specimen.

3.2 Methods

3.2.1 Specimen Preparation

Five fresh-frozen pelvis-to-toe cadaveric specimens (10 hips, 2 male / 3 female, age = 69 ± 8 years, height = 69 ± 5 inches, weight = 168 ± 38 lbs., BMI = 25.0 ± 4.7) underwent bi-lateral THA using modular dual mobility (DM) implants (PINNACLE^{TM} acetabular cups with either SUMMIT^{TM} or CORAIL^{TM} femoral stems (DePuy Synthes, Warsaw, IN). Surgeries were performed by ten different board-certified orthopedic surgeons via either the direct anterior or posterior approach on contralateral hips. All specimens underwent pre- and post-operative computed tomography (CT) scans to quantify the native bony anatomy and implant alignment. For each hip, 3D models of the native pelvis and femur, implanted pelvis and femur, femoral stem, and acetabular shell were segmented from the CT scans using ScanIP (Synopsys, Mountain View, CA). Pelvic and femoral anatomic coordinate systems were defined from the native bony 3D models (Tannast et al. 2007). The 3D models of the implanted pelvis, femur, and respective implants were aligned to the native bones, and the implant CAD models were aligned to the scanned implants, thus achieving matched pairs of geometries for further kinematic evaluation.

3.2.2 Experimental Laxity & Dislocation Evaluation

A six Degree of Freedom (DOF) VIVO Joint Simulator (AMTI, Watertown, MA) was used to characterize hip capsule laxity in all 10 hips. The hemi-pelvises were mounted to

specimen-specific 3D printed fixtures, while the femurs were mounted inside cylindrical fixtures with bone cement. This fixturing approach aligned the pelvis and femur anatomic coordinate systems to the VIVO simulator degrees of freedom. It also ensured the hip center of rotation coincided with the intersection point of the rotational axes of the simulator. An optical motion capture system (Optotrak Certus, NDI, Ontario, Canada) was used to track rigid arrays of infrared emitting diodes attached to the pelvis and femur and provided data for kinematics calculations. A 50 N compressive load and a 10 N medial load were applied to the hips to maintain nominal contact, while the anterior/posterior (AP) DOF was maintained at 0 N. The flexion-extension (F-E) and adduction-abduction (Ad-Ab) axes were fixed at 0° of rotation. The I-E axis was loaded with a trapezoidal wave with a 5 Nm maximum torque as has been previously used to describe a taut hip capsule (van Arkel et al. 2015). This I-E laxity assessment was performed at hip flexion angles of 0°, 30°, 60°, and 90°. In addition, movements intended to cause anterior and posterior dislocation were simulated. The anterior dislocation profile hyperextended the hip from 0° to -30°, coupled with 0° of Ad-Ab and 1° of ER per degree of hyperextension. The anterior dislocation profile continued till hyperextension of 30° or until 10 Nm reaction torque was observed about the F-E axis. The posterior dislocation profile flexed the hip from 90° to 120°, coupled with 0.5° of adduction and 1° of IR per degree of hip flexion. The corresponding reaction torques in the F-E, Ad-Ab, and I-E DOFs were recorded by the VIVO simulator.

3.2.3 Kinematics Post-Processing

When the laxity and dislocation evaluations were complete, the hips were skeletonized, and four fiducial markers each were affixed into the pelvis and femur. The fiducial markers were digitized using the motion capture system to measure the relative alignment between the fiducial markers and the optical tracking arrays. The femur and pelvis were then optically scanned (Space Spider 3D Scanner, Artec, Luxembourg Luxembourg). The white-light scans of the skeletonized DM-THA femur and pelvis were converted into 3D models and then aligned to the original CT 3D models in their anatomical position. This orientation defined neutral rotation and translation and aligned the experimental and computational coordinate systems from which the kinematics were calculated. Forces and torques (measured about the head center) were recorded using the 6-DoF load cell incorporated in the simulator. Statistically significant differences in internal and external rotations at 5 Nm across flexion angles between the anterior approach and posterior approach specimen were tested via a 2-way repeated measures analysis of variance (RMANOVA) with Tukey's post-hoc tests. The surgical approach and flexion angle were considered independent variables with the significance level was set to $p < 0.05$. The specimen-specific I-E laxities, dislocation profiles, and aligned geometries were used to develop specimen-specific finite element models.

3.2.4 Hip Capsule Model

The implant CAD models aligned with the CT scan-derived implanted hip geometries were used in the finite element models. The capsule was modeled as a cylindrical sleeve that originated at the acetabular rim and inserted at the femoral intertrochanteric line

(Figure 3.1). The creation of the capsule using membrane elements was automated through a Matlab script (MathWorks, Natick, MA). The script fit ellipses to the manually identified capsule attachment points on the acetabulum (origin) and femur (insertion). A line connecting the lateral most points of the origin and insertion ellipses was used as the reference line for longitudinal capsule fibers. The capsule was subdivided into six longitudinal sectors to approximate the capsule's ligaments, with each sector circumscribing 60° of the attachment ellipses starting from the reference line in the counterclockwise direction in the superior-inferior direction. The stiffness and pre-strain properties of these sectors were parameterized to be tuned in subsequent calibration. In addition, the longitudinal fiber orientation of the capsule was parametrized by a twist angle, whereby the femoral capsule attachment nodes were rotated along the femoral attachment ellipse about the longitudinal axis of the capsule. Each capsule consisted of 810 quadrilateral elements with an average edge length of 3.1-mm. The bones and implant components were modeled as rigid bodies using triangular shell elements with an element edge length of 1.0 mm.

The capsule was modeled as a fiber-reinforced soft tissue using nonlinear tension-only springs embedded longitudinally in the hyperelastic membrane elements, which were previously validated for modeling knee ligaments (Baldwin et al. 2012). The ligament force-displacement response was parametrically defined as,

$$f=0,\ \varepsilon < 0$$

$$f = 0.25\ k\ \varepsilon^2/\ \varepsilon_l,\ 0 \leq \varepsilon \leq 2\ \varepsilon_l$$

$$f = k\ (\varepsilon - \varepsilon_l),\ \varepsilon > 2\ \varepsilon_l$$

where ε is the current engineering strain, ε_l is the reference ligament strain which defines the toe region (0.03), k is ligament stiffness and f is the ligament force (Blankevoort and Huiskes, 1996). The hyperelasticity of the capsule was defined using the Marlow model in Abaqus/Explicit (Dassault Systèmes, Waltham, MA) and experimental ligament tissue stress-strain data (Marlow, 2003). Contact between bones, implants, and capsule were modeled using general contact. All contact interactions were considered rigid to improve efficiency with the appropriate pressure-overclosure relationships previously validated for implanted joints (Fitzpatrick et al. 2010). A coefficient of friction of 0.04 was defined at the cup-liner, head-liner and stem-liner interfaces, while all other interactions had a coefficient of friction of 0.01. In all evaluations, the pelvis was fixed, and loading was applied through the femur head center via connector elements. Hip rotations were calculated using passive connector elements located at the hip rotation center corresponding to the previously described experimental kinematics (Grood & Suntay, 1983).

3.2.5 Model Calibration & Validation

Specimen-specific tissue properties for each capsule sector (6 stiffnesses, 6 pre-strains, and twist angle) were optimized to minimize the RMSE in the model-predicted and experimentally measured I-E torques at six corresponding I-E rotation angles throughout each laxity curve (IR and ER curves at flexion of 0°, 30°, 60°, and 90°) for a total of 48 equally weighted data points in the objective function (figure 3.2). Parameter optimization was conducted using the simulated annealing algorithm (Kirkpatrick et al. 1983) in Isight

(Dassault Systèmes, Waltham, MA) set with upper and lower bounds of parameters falling within the physiological range (Harris et al. 2016).

The specimen-specific model predictions were evaluated by applying the anterior and posterior dislocation profiles to the calibrated models and calculating the resulting F-E, Ad-Ab, and I-E resistance torques. Dislocation simulations were terminated at the initiation of subluxation due to bone-bone or implant-bone impingement thereby isolating the contribution of the capsule for validation. A combined dislocation resistance torque, defined as the square root of the squared sum of these three torques, was compared to corresponding experimental data. The resulting RMSE was used to quantify the model's predictive capability.

The accuracy improvement associated with specimen-specific models was assessed by comparing the RMSE in specimen-specific laxity predictions of the calibrated capsules against the RMSE in laxity predictions of models with specimen-specific specific geometry but with averaged capsule properties for all ten specimens. Paired t-tests were performed to compare RMSEs between specimen-specific and average property models at all flexion levels and loading conditions. In addition, a linear regression was performed comparing torque predictions from the specimen-specific and averaged property models with the experimental laxity through the flexion range. The contributions of the various capsule sectors to hip stability were evaluated by averaging the total force in each sector at 5 Nm of applied torque during the laxity evaluations.

3.3 Results

Internal hip rotation was highest at 30° flexion (76.0° ± 19.3°) and reduced with increasing flexion to 90° (47.8° ± 19.7°) under a 5 Nm torque (Figure 3.3). The internal laxity at 90° flexion was significantly lower than both 0° and 30° flexion. External hip rotation moderately increased with increasing flexion past 30°, with the lowest average external rotation at 30° flexion (26.3° ± 9.1°) and the highest at 90° flexion (39.7° ± 15.9°). No statistically significant differences were observed with flexion. When grouped based on surgical approach, the posterior approach specimens had increased internal laxity at 30°, 60°, and 90° flexion compared to the anterior approach specimens, but these differences were not statistically significant. In contrast, the anterior approach specimens had increased external rotation at 30°, 60°, and 90° flexion compared to the posterior approach specimens, but these differences were also not statistically significant. The largest difference in internal and external laxity between the two approaches was 10.3° and 6.5°, respectively, at 60° flexion.

The specimen-specific capsule sector pre-strains after calibration averaged 0.99 ± 0.03 [0.93-1.03], 0.71 ± 0.11 [0.50-0.88], 0.62 ± 0.16 [0.37-0.89], 0.57 ± 0.09 [0.45-0.67], 0.48 ± 0.10 [0.32-0.60] and 0.57 ± 0.14 [0.38-0.80] for sectors 1 through 6, respectively (Table 3.2). The averaged specimen-specific stiffnesses of the capsule sectors were 61 ± 16 [37-86], 62 ± 19 [23-88], 59 ± 12 [34-80], 54 ± 8 [35-67], 71 ± 7 [60-86] and 50 ± 18 [20-71] N/mm for sectors 1 through 6, respectively. Twist angles across the ten hips averaged 33.5° ± 12.9° and ranged from 18.7° to 63.9°. The specimen-specific I-E torque-rotation responses of the calibrated models were compared to the experimental data in Figure 3.4. The average residual RMSE between model and experimental I-E laxity responses at 0°,

30°, 60°, and 90° flexion were 0.86 ± 0.25, 0.81 ± 0.15, 0.99 ± 0.48, and 1.41 ± 0.67 Nm, respectively.

Calibrated model predictions and the corresponding experimental torques measured during the anterior and posterior dislocation loading profiles are shown in Figure 3.5. The average RMSE across specimens during the dislocation profiles were 0.78 ± 0.33 and 1.10 ± 0.48 Nm for anterior (8 specimens) and posterior (9 specimens) dislocations, respectively. Three trials were excluded from the comparison because the measured torque exceed 10 Nm in the initial position for the anterior dislocation test (specimens 4 and 10) or posterior dislocation test (specimen 7).

The generalized models using specimen-specific geometry and the averaged capsule properties had significantly lower accuracy than the calibrated specimen-specific models. The RMSE at 0°, 30°, 60°, and 90° flexion increased to 2.71 ± 1.26, 2.37 ± 0.88, 2.09 ± 0.37 and 2.39 ± 0.77 Nm, respectively. Averaged across all flexion angles, the generalized models resulted in an RMSE of 2.39 ± 0.68 Nm, while the specimen-specific models resulted in an RMSE of 1.02 ± 0.21 Nm. Across all loading conditions, there was a stronger correlation between model predictions and experimental measurements for the calibrated capsule models (r^2=0.87) compared to the generic models (r^2=0.39) (Figure 3.6).

Average peak tensions in each sector of the hip capsule under 5 Nm of torque ranged from 0 to 162.4 N (Figure 3.7). Sector 1, analogous to the lateral arm of the ILFL, experienced maximal loading of 162.4 ± 33.0 N during ER at 0° flexion that reduced with increasing flexion. Sector 2, analogous to the medial arm of the ILFL, experienced maximal loading of 160.0 ± 92.2 N during hip extension. Sectors 3 and 4, analogous to the PFL, experienced lower peak loads of 44.4 ± 43.3 N and 105.9 ± 119.0 N, respectively,

resisting maximal flexion. Both sectors 5 and 6, analogous to the ISFL, experienced peak forces of 83.0 ± 94.6 N and 32.2 ± 48.4 N under internal rotation beyond 60° flexion. Overall, sectors forming the posterior aspect of the capsule demonstrated more load sharing and higher variability in sector forces across specimens than the sectors forming the anterior capsule.

3.4 Discussion

This study developed specimen-specific models of ten implanted hip capsules using experimental I-E laxity data to calibrate the capsule parameters and evaluated the models' predictions during simulated movements known to cause anterior and posterior dislocation. The average RMSE between calibrated model predictions and the experimentally measured torques were approximately 1 Nm across the laxity and dislocation simulations. The capsule calibration process reduced the prediction error by more than 50% compared to the generic capsule models. The improved accuracy associated with a patient-specific approach could potentially enable use of computational capsule models to be applied intraoperatively to influence implant configuration, alignment, sizing, and capsule repair techniques.

3.4.1 Ligament recruitment patterns

The current study represented the capsule using a simplified tubiform mesh that enabled automatic and parametric mesh generation suitable for optimization but did not explicitly represent the individual ligamentous components of the capsule. Despite this difference, the calibrated capsule models demonstrated recruitment patterns similar to

capsule function reported in the literature. Multiple experimental studies have shown the ILFL is the primary restraint to external hip rotation (Hidaka et al., 2014, Burkhart et al., 2020, Martin et al., 2008, Van Arkel et al., 2015, Myers et al., 2011). Sectors 1 and 2 in the current model correspond to the lateral and medial arms of the ILFL, respectively. Sector 1 provided the primary resistance to external rotation through the flexion range. Sector 2 contributed to resisting external rotation in the extended hip, but also resisted hip extension, consistent with the description by Hidaka et al. Both Van Arkel et. al and Martin et al. noted that the superior ILFL was also recruited during IR with hip extension. Similarly, sector 1 in the model was consistently the primary restraint to IR at full extension.

Sectors 5 and 6 correspond to the ISFL and were primarily recruited to resist internal rotation, with their largest contributions coming with hip flexion beyond 30°. This is consistent with observations by Burkhart et al and Martin et al that the ISFL is the primary restraint to internal rotation. In addition to the ISFL, sectors 3 and 4, corresponding to the PFL, contributed to resisting internal rotations with hip flexion beyond 30°. Similar observations were made by both Martin et al and Van Arkel et al that the PFL played a significant role in resisting internal hip rotation in flexion. Thus, the model's resistance to internal rotation of the hip was influenced by hip flexion angle, shifting from the ILFL in extension, to the ISFL in mid flexion, with an increased contribution of the PFL at 60° and 90° flexion. Although not considered in this experiment, the PFL is a primary restraint to hip abduction (Martin et al., 2008) and may experience higher tensions during abduction than found in this study during maximal flexion. It should be noted that most experimental studies of capsule biomechanics focus on the natural hip, which typically has a larger

diameter femoral head than the implanted hip. Disruption of the capsule during the surgical approach and reduction of the femoral head diameter after surgery have been shown to directly affect hip stability (Van Arkel et al., 2018, Abrams et al. 2015; Khair et al.2017). The current study used a dual mobility construct that has demonstrated smaller increases in capsular laxity following THA compared to a conventional construct, likely due to greater ligament wrapping (Logishetty et al., 2019). These approaches and implant specific changes to capsule recruitment necessitate the proposed model calibration.

3.4.2 Model accuracy

Multiple studies in the literature have developed mathematical models of the hip capsule to provide insight into capsule biomechanics (Karunaseelan et al., 2021, Bunn et al., 2014, Myers et al., 2020, Wingstrand et al., 1997, Helwig et al., 2013, Stewart et al., 2004, Elkins et al. 2011). These mathematical representations range in complexity from simple 1D springs that wrap around the femoral head (Karunaseelan et al., 2021, Bunn et al., 2014) to complex 3D finite element continuum models (Stewart et al., 2004, Elkins et al. 2011). Only three of these studies have attempted to calibrate models of the capsule to replicate experimentally observed hip laxity (Elkins et al., 2011, Bunn et al., 2014, Myers et al., 2020). Elkins et al. calibrated a finite element model of the capsule using force-displacement data from an axial distraction test on a single cadaveric specimen (Elkins et al. 2011). They modeled the capsule as a continuous cylinder segmented into sectors like the current model but used hexahedral elements and a continuum material model to predict capsule strains. Bunn et al. represented the capsule using ellipsoidal rigid bodies in a musculoskeletal modeling software and calibrated stiffnesses of the ILFL and ISFL to

represent literature reported axial distraction data (Bunn et al., 2014). Neither study quantified the model's ability to accurately represent capsule restraint beyond a qualitative assessment making comparisons with the current model's accuracy difficult.

In a previous study from our institution, Myers et al. developed a parametric model of the hip capsule using similar methods to the current study. The capsule was modeled using fiber-reinforced membranes, but the ligament configuration more directly represented the individual capsular ligaments, including the ILFL, ISFL, PFL, and Zona Orbicularis. ligament properties were calibrated to average experimental hip laxity reported in the literature, including combinations of I-E, Ad-Ab, and F-E movements (Van Arkel et al., 2015). Depending on the movement, the reported model RMSE ranged from 4.0° to 5.3° for I-E rotations and 2.5° for flexion and extension. During the optimization process for the current study, differences in joint torques observed with displacement-controlled hip rotations were primarily used to quantify prediction accuracy. However, when calculated using the same methods as Myers et al, the average RMSE across all movements for the current study was 5.2°. Myers et al noted a limitation to representing the capsule using the individual ligamentous structures was the inability to characterize complex load transfer that may exist between structures. Given the current study was attempting to model a variety of specimen specific laxity behaviors, ranging from tight to loose, similar accuracies between the two studies suggest the use of a simplified tubiform mesh was a reasonable assumption.

3.4.3 Intra-operative Applications

Patient-specific soft-tissue models have long been developed for other joints, including the knee (Harris et al. 2016), cervical spine (Kallemeyn et al. 2010), lumbar spine (Weisse et al. 2012) and shoulder (Drury et al. 2011). However, this is the first study to develop patient-specific representations of the hip capsule. Methodologies for development of these capsule models may ultimately enable use of the models as a pre- or intra-operative tool for surgical decision making. Pre-operative tools currently exist that allow surgeons to evaluate the effect of pelvic mobility on functional acetabular cup orientation, impingement risk between the implants and bones, and proclivity for edge-loading (Miki et al., 2014, Barsoum et al., 2007, Liu et al., 2018). However, the risk of adverse loading conditions is influenced by capsular function (Karunaseelan et al., 2021) and is not considered in these patient-specific analyses. Leveraging patient-specific capsule models formulated intra-operatively could address this limitation and further reduce risks of impingement. Similar finite element models of the hip capsule have been used to provide clinically relevant insight into the interactions between capsule function, implant alignment, bearing type (e.g., lipped, or dual mobility), head offset, and dislocation resistance (Myers et al., 2022) and the effects of capsule releases and repairs on hip stability (Elkins et al. 2011).

Several technical challenges exist to adopting these models as intraoperative tools. The poor predictions of capsule models using averaged ligament properties in the current study clearly demonstrates the necessity to calibrate models for use with individual patients. Additional research must be performed to determine the optimal amount of hip laxity information necessary to achieve the desired model accuracy. Surgeons commonly

use the “shuck” test to evaluate hip stability (Charles et al. 2005) and similar distraction data has previously been used to calibrate capsule models (Bunn et al., 2014, Elkins et al. 2011). However, it’s unclear that distraction data alone provides sufficient information to determine the rotational restraint the capsule provides when resisting impingement and dislocation. Further, it must be demonstrated that hip laxity data collected intra-operatively, rather than via sophisticated testing equipment, provides sufficient fidelity for model calibration. Finally, the calibration algorithm used in the current study was computationally expensive and time consuming, requiring an average of 72 hours of processor time for model convergence. This challenge could be overcome through future work using statistical models or machine learning algorithms to predict capsule parameters from hip laxity data rather than using time-intensive optimization techniques.

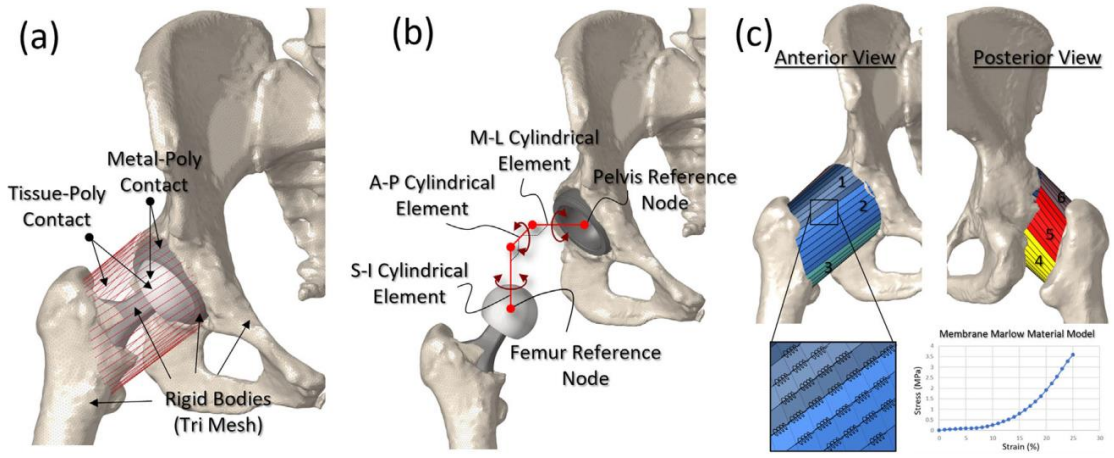

Figure 3.1: (a) Assembled hip capsule model, including rigid triangular meshes of the bones and implants, fiber-reinforced membrane elements representing the hip capsule, and contact between the implants and capsule. (b) Exploded view of the mutually orthogonal cylindrical connector elements used to apply loads and measure kinematics between the femur and pelvis. (c) Six regions of the capsule from anterior and posterior aspects of the capsule, including an enlarged view of the fiber-reinforced membrane elements and the stress-strain response of the membrane elements comprising the capsule.

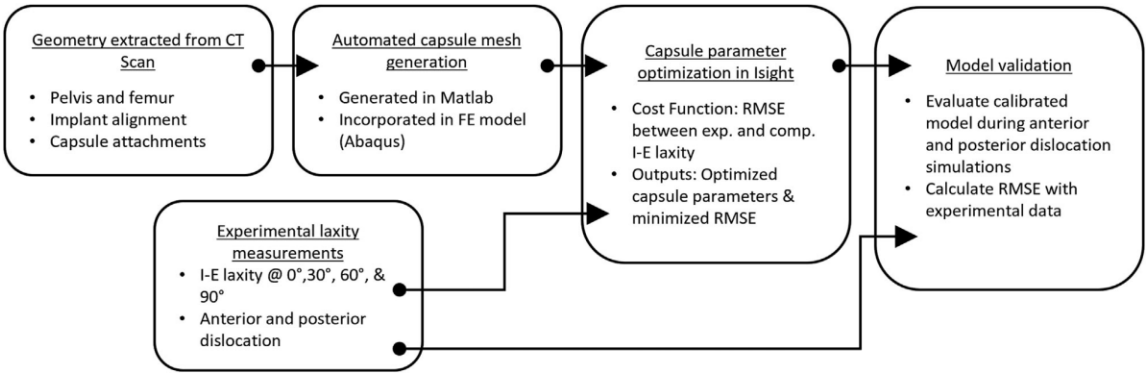

Figure 3.2: Overview of the modelling workflow, including generation of the model geometry from the CT scans, calibration of the capsule parameters to match the experimental laxity data, then validation of the model by predicting hip torques during anterior and posterior dislocation simulations.

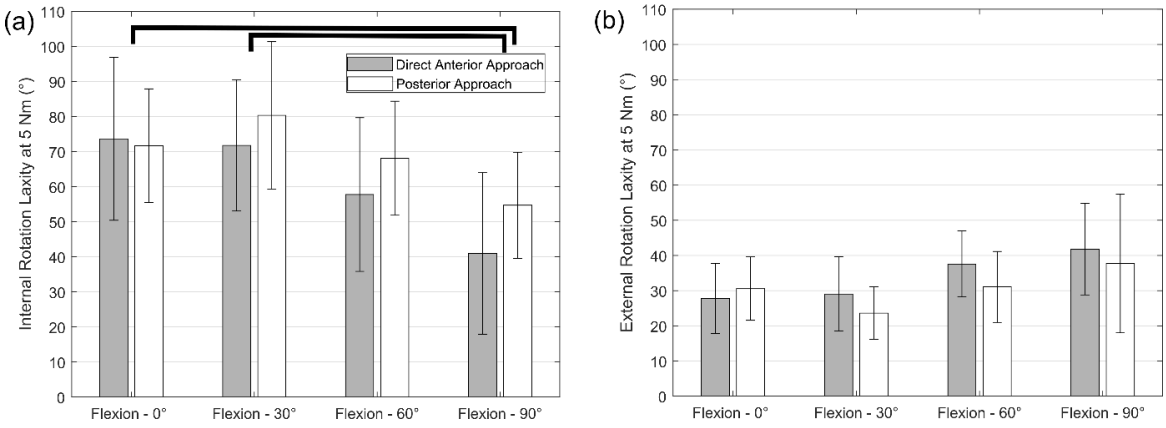

Figure 3.3: (a) Internal and (b) External rotational laxity at 5 Nm I-E torque at different flexion angles for specimens implanted using direct anterior (n=5) and posterior approaches (n=5). Statistically significant differences were represented with bars ($p<0.05$)

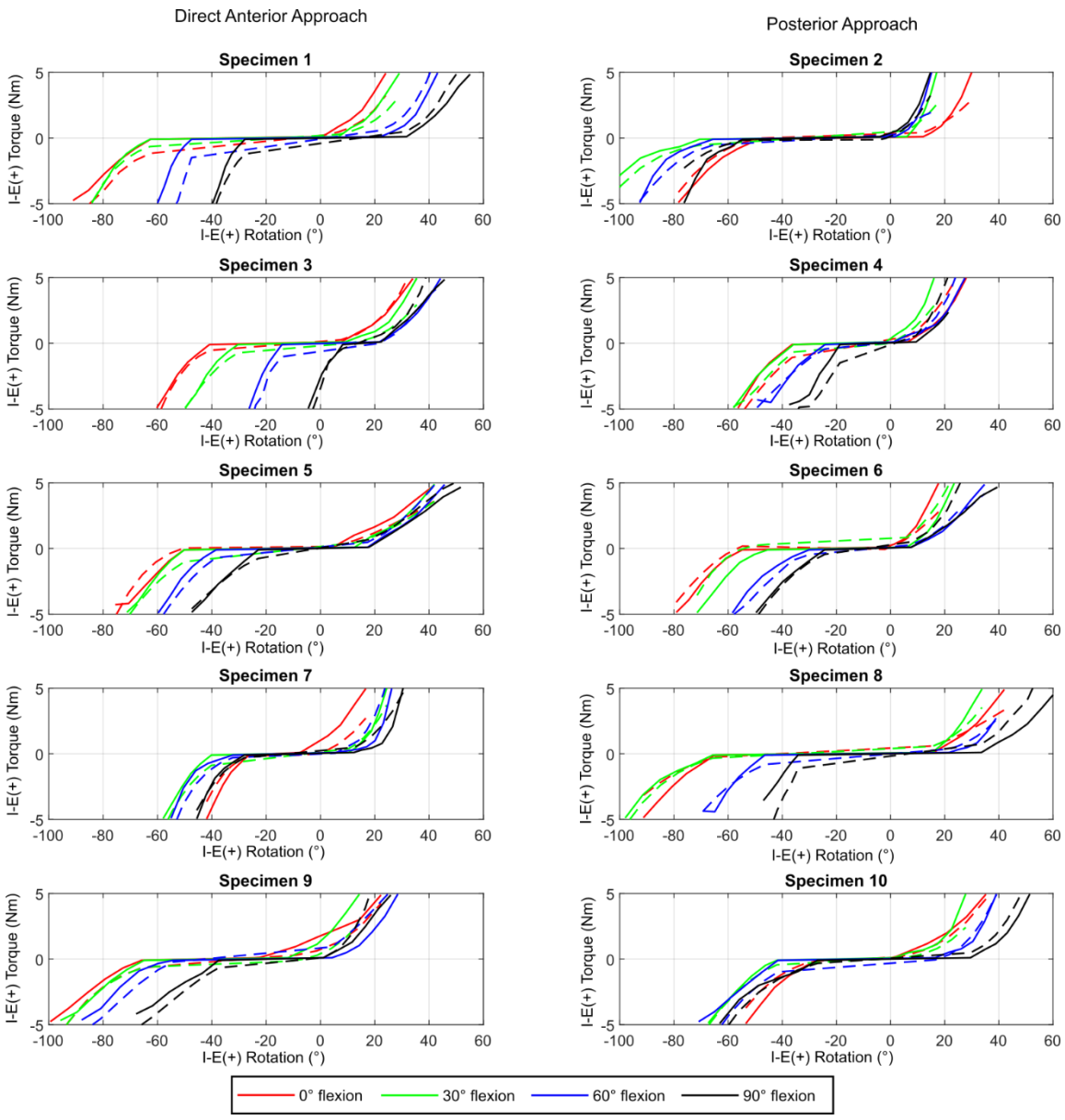

Figure 3.4: Specimen-specific calibration results using I-E laxity data with the solid lines representing the experimental data and dotted lines showing the corresponding model predictions.

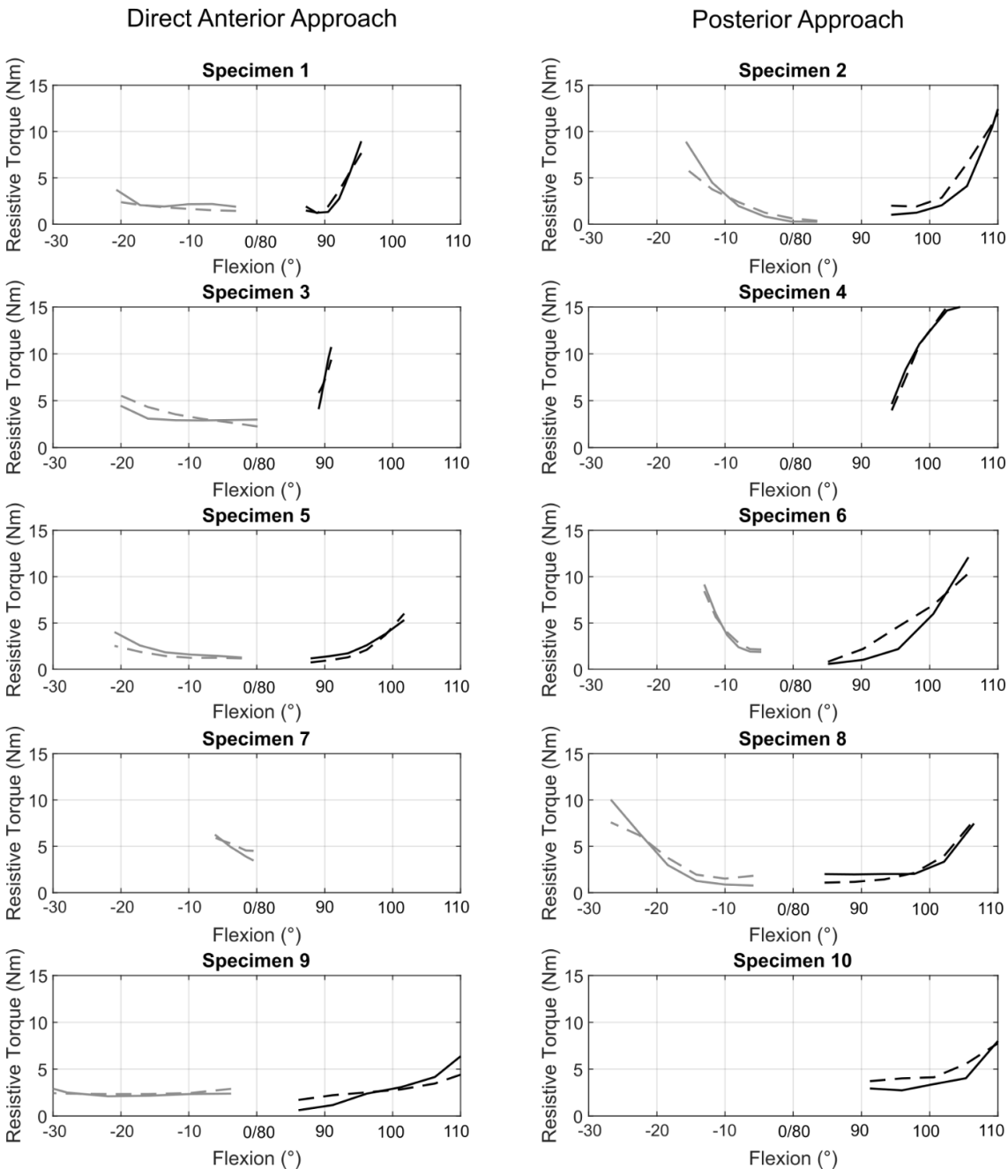

Figure 3.5: Specimen-specific models were evaluated using anterior (grey) and posterior (black) dislocation simulations and the experimental (solid) and model (dotted) dislocation resistance torque predictions were compared.

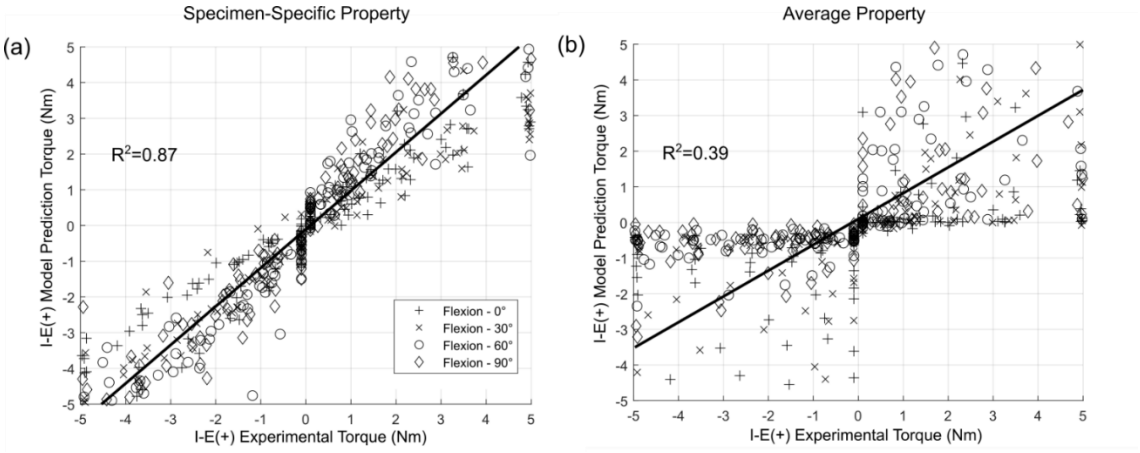

Figure 3.6: Scatter plot and best fit linear regression lines for experimental and model torque predictions using specimen-specific (a) and average properties (b) during IE laxity evaluations at all four flexion angles.

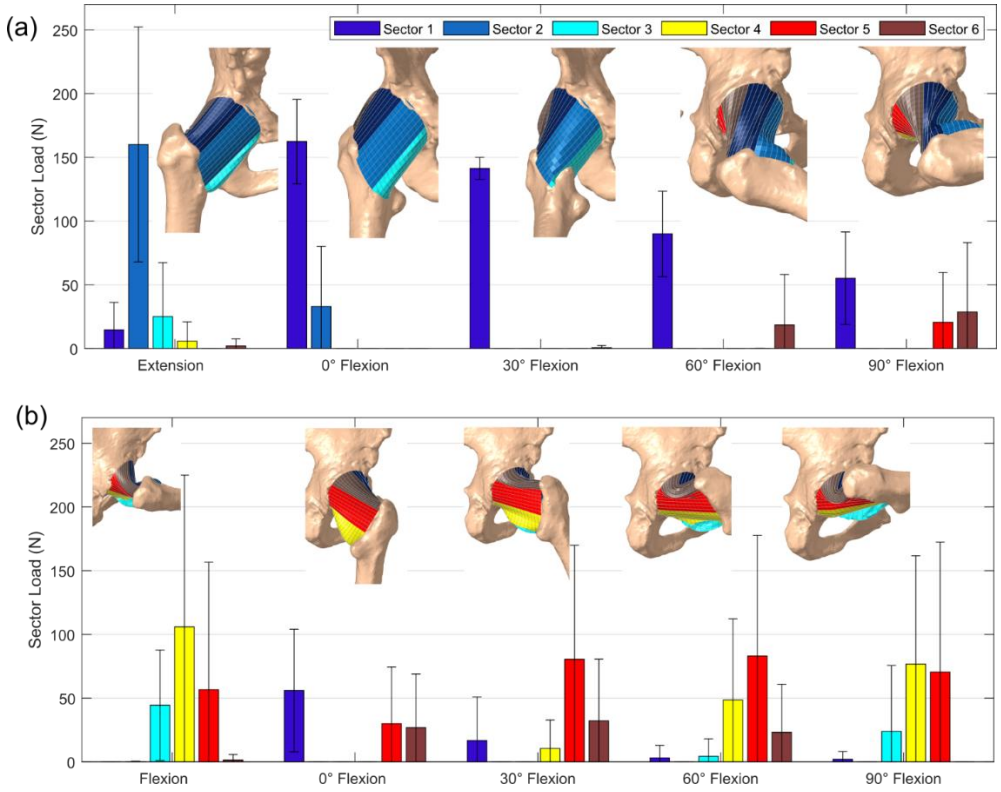

Figure 3.7: Ligament recruitment pattern across 5Nm IE laxity envelops for ten specimen-specific models during (a) external and (b) internal rotation.

Table 3.1: Calibration results for the ten specimens. The results were averaged and used in the average-property models.

Specimen ID	Prestrain – Sector #						Stiffness (N/mm) – Sector #						Twist Angle (°)
	1	2	3	4	5	6	1	2	3	4	5	6	
1	1.002	0.652	0.632	0.548	0.463	0.429	50.38	77.08	62.54	50.26	73.08	27.38	32.40
2	0.989	0.681	0.456	0.585	0.394	0.659	62.68	22.97	46.93	50.58	85.90	69.48	63.84
3	1.002	0.809	0.885	0.666	0.526	0.581	74.74	58.83	58.20	66.62	70.80	48.78	25.09
4	1.028	0.756	0.665	0.498	0.575	0.559	75.14	58.76	56.89	55.41	63.13	61.59	30.48
5	0.929	0.772	0.754	0.493	0.595	0.521	44.56	75.74	58.98	57.89	73.07	34.74	25.03
6	0.994	0.666	0.533	0.470	0.575	0.438	61.29	66.80	53.35	53.12	66.69	62.02	46.92
7	0.996	0.832	0.712	0.640	0.411	0.794	71.18	59.42	68.52	57.64	66.46	71.22	30.90
8	0.964	0.579	0.467	0.662	0.321	0.567	46.19	75.61	65.53	34.65	68.78	19.48	30.99
9	0.966	0.496	0.369	0.450	0.539	0.378	37.24	40.06	34.06	52.88	77.11	63.21	30.26
10	1.018	0.847	0.755	0.655	0.367	0.802	86.05	87.82	80.21	59.53	60.19	45.72	18.68
Average ± Std	0.989 ± 0.029	0.709 ± 0.115	0.623 ± 0.163	0.567 ± 0.086	0.477 ± 0.098	0.573 ± 0.145	60.945 ± 15.95	62.309 ± 19.213	58.521 ± 12.464	53.858 ± 8.314	70.521 ± 7.368	50.362 ± 18.189	33.459 ± 12.895

Table 3.2: Calculated RMSE in the IE laxity curves prediction between specimen-specific and average property models during individual and all four flexion angles combined. Validation RMSEs were reported between the calibrated specimen-specific model predictions and experimental data during two dislocations.

Specimen ID	Calibration (Laxity) - RMSE (Nm)										Validation (Dislocation) - RMSE (Nm)	
	IE 0° flexion		IE 30° flexion		IE 60° flexion		IE 90° flexion		IE Combined			
	Specimen-Specific	Avg Property	Specimen-Specific	Average Property	Specimen-Specific	Average Property	Specimen-Specific	Average Property	Specimen-Specific	Average Property	Anterior Dislocation	Posterior Dislocation
1	1.19	4.68	0.74	1.20	2.13	2.28	1.17	3.17	1.31	2.83	0.65	0.71
2	0.79	2.07	0.94	3.03	1.03	1.89	1.06	1.74	0.96	2.18	1.26	1.75
3	0.39	1.3	0.79	1.78	0.84	2.45	1.64	1.96	0.92	1.87	0.79	1.12
4	1.04	2.33	0.85	2.51	0.71	2.23	1.52	2.22	1.03	2.32	-	0.84
5	0.75	1.6	0.62	2.48	0.69	2.13	0.47	2.19	0.63	2.10	0.71	0.47
6	0.87	2.14	1.04	2.17	0.52	1.74	2.23	2.01	1.17	2.02	0.42	1.50
7	1.17	2.52	0.66	2.21	1.24	1.84	0.66	1.94	0.93	2.13	0.58	-
8	0.88	5.16	0.62	4.43	0.45	2.86	2.40	4.29	1.09	4.19	1.32	0.63
9	0.94	2.97	1.02	2.05	1.08	1.77	2.06	2.23	1.28	2.26	0.54	1.19
10	0.57	2.32	0.81	1.82	1.17	1.74	0.84	2.19	0.85	2.02	-	1.73
Average ± Std	0.86 ± 0.25	2.71 ± 1.26	0.81 ± 0.15	2.37 ± 0.88	0.99 ± 0.48	2.09 ± 0.37	1.41 ± 0.67	2.39 ± 0.77	1.02 ± 0.21	2.39 ± 0.68	0.78 ± 0.33	1.10 ± 0.48

CHAPTER 4. INSTANTANEOUS GENERATION OF SPECIMEN-SPECIFIC FINITE ELEMENT MODELS OF HIP CAPSULES

4.1 Introduction

Patient-specific THA surgery has emerged with the increased use of image-based planning, navigation, and robotic surgical systems in recent years (Colombi et al., 2019; Subramanian et al., 2019). Studies investigating the effectiveness of these systems demonstrate precise reconstruction of native hip anatomy, including implant positioning, fit with the host bone, restoration of center-of-rotation, limb length, and offset (Emara et al., 2021). These systems use bone-based imaging and three-dimensional (3D) templating software in preoperative planning to identify the optimal component size, angle, and position (Riddick et al., 2014). Furthermore, these systems offer intraoperative feedback to assist surgeons in performing precise bone cuts and implant placement while enhancing the surgeon's accuracy and reproducibility (Fontalis et al., 2022). However, these systems do not include the hip capsule in their pre-operative or intra-operative planning, which limits their ability to predict hip stability and range of motion after surgery.

The hip capsule's function is complex, with each ligament structure in the capsule contributing to stability in certain degrees of freedom (Martin et al., 2008). Studies report that reduced wrapping of the hip capsule around the smaller implanted femoral head after

THA decreases its restraint to hip rotations (van Arkel et al., 2018). Even though THA causes a loss of capsule function, there is a lack of consensus on the optimal surgical approach and capsule repair technique. For example, one group of studies reports there is no significant difference in dislocation risk between approaches: anterior vs. posterior (Maratt et al., 2016) and posterior vs. direct lateral (Mjaaland al., 2017). Another group of studies contradicts it by reporting significant differences in dislocation risk: direct anterior vs. posterior (Haynes et al., 2022), posterolateral vs. direct anterior and anterolateral (Zijlstra et al., 2017). Similarly, no clear consensus exists, with some proponents for capsule repair (Swanson et al., 2019; Pedneault et al., 2020) and others indifferent to the repair (Vandeputte et al., 2021; Schwartz et al., 2021). Thus, utilizing patient-specific models of the hip capsule to evaluate dislocation risk could offload the cognitive burden of the surgeon and provide clarity on when capsule repair may be beneficial.

Recently, finite element models of hip capsules with soft tissue constraints have been reported in the literature. For instance, Elkins et al. developed a hip capsule model by tuning the material coefficients to match the load-displacement curve from a distraction-type test (Elkins et al., 2011). Further, Myers et al. developed a probabilistic representation of the implant capsule by optimizing the ligament properties to match the literature-reported average torque-rotation curves (Myers et al., 2020). We recently developed high-fidelity finite element models (Fig. 4.1), which could capture the subject-specific torque-rotation response of the ligamentous structure and validated their predictions against experimentally measured dislocation risks (Anantha Krishnan et al., 2023). These models capture patient-specific characteristics and, if integrated into the patient-specific surgical

planning and intra-operative decision-making workflow, could be valuable in implant positioning and hip capsule management.

Developing subject-specific models of ligamentous structures by calibrating ligament parameters to match experimental data from cadaveric specimens is time-intensive. Calibration of ligaments takes between three days to three months, depending on the number of parameters included (determined by the type of joint), the optimization algorithms used, and the computational resources available (Anantha Krishnan et al., 2023; Ezquerro et al., 2011). Such a time frame is untenable if the end goal is to use the model for intra-operative decision-making like identifying optimal implant position or managing capsule repairs to minimize dislocation risk. In addition, computational models have challenges when balancing generalizability and specificity, such as evaluating mean-population scenarios vs. accounting for patient-specific variability like bone geometry, ligament properties, and attachment sites (Anantha Krishnan et al., 2023, Ewing et al., 2016, Bischoff et al., 2014, Baldwin et al., 2009). Practically, it is critical to identify the minimum parameters required to capture patient-specific differences with the fidelity necessary to detect clinically significant differences. For instance, if the impact of a particular patient-specific parameter on the model's accuracy is marginal, it can be ignored, reducing the size of the parameter space and the calibration time.

Statistical shape models have long been used in orthopedic biomechanics to understand bone morphology, geometric variability and to reconstruct 3D geometries from sparse image data (Sarkalkan et al. 2014, Hollenbeck et al. 2018, Reyneke et al. 2018). A few studies extended this technique to relate joint shape models with their function resulting in statistical shape-function type models: knee anatomy with tibiofemoral and

patellofemoral kinematics (Smoger et al. 2015), total knee geometry and alignment with joint mechanics (Gibbons et al. 2019) and knee anatomy with laxity (Shalhoub et al. 2022).

This paper aims to develop a statistical model of the implanted hip capsule relating geometry-material property with joint laxity to instantaneously generate patient-specific FE models while simultaneously identifying the minimal input parameters required to develop accurate models.

4.2 Methods

4.2.1 Overview

A statistical framework to predict hip capsule parameters was developed based on a previously validated probabilistic finite element model of the implanted hip capsule (Figure 4.2). The parametric model was repeatedly evaluated via Monte Carlo simulations with Latin Hypercube sampling to represent 95% of the population's variability in capsule properties and attachment sites. Multivariate regression models were developed that predict capsule properties (pre-strain and stiffness) from the patient's hip laxity and attachment site geometry. The regression models were validated by predicting the hip capsule properties for subject-specific experimental cadaveric data (Figure 4.2).

4.2.2 FE Model of the Implanted Hip Capsule

A previously validated specimen-specific implanted hip capsule model was used in the current study and the model is briefly described here (Anantha Krishnan et al., 2023). Pelvis and femur bony geometry were segmented from the CT scan of a cadaveric hip implanted with a THA. The manufacturer's implant CAD models (CORAIL® Total Hip

System, DePuy Synthes, Warsaw, IN) were aligned with the implant geometries in the CT scan.

The capsule was modeled as a cylindrical sleeve that originated from an ellipse around the acetabular rim and inserted into an ellipse around the femoral intertrochanteric line (Figure 4.1). An automated Matlab script (MathWorks, Natick, MA) generated a series of nodes connecting corresponding points on the pelvis and femur ellipses, wrapping around the femoral head when present. Corresponding nodes in adjacent lines were connected to form quadrilateral elements along the length of the capsule. The capsule was subdivided into six longitudinal sectors to approximate the ligaments that compose the capsule. Each sector was modeled using fiber-reinforced quadrilateral hyperelastic membrane elements with nonlinear tension-only springs embedded axially along the element edges (Baldwin et al., 2012). The stiffness and pre-strain of each sector were independently parameterized for probabilistic analysis. The sector stiffness was defined as the total stiffness for the sector and divided across the number of spring elements acting in parallel in the sector mesh. Similarly, the sector pre-strain was equally divided among all springs acting in series along each longitudinal line of spring elements.

Contact between bones, implants, and capsule were modeled using the general contact algorithm in Abaqus/Explicit, with all contact interactions considered rigid with the appropriate pressure-overclosure relationships to improve solver efficiency (Fitzpatrick et al., 2010). A coefficient of friction of 0.04 was applied between the cup-liner, head-liner, and stem-liner interfaces. All other contact (bone-bone, bone-implant, capsule-implant, and capsule-bone) were defined with a coefficient of friction of 0.01. In all trials, the pelvis was fixed in space while torques were applied through the femur. The resulting hip

rotations were calculated using passive connector elements embedded at the hip rotation center using a three-cylindric open chain configuration (Grood & Suntay, 1983).

4.2.3 Statistical Shape Model of the Capsule

A principal component analysis (PCA) was performed on the pelvis and femur bony geometry from 156 hips to quantify the variability in the capsule attachment sites (39% Female, Age:72±11, Height: 67±3in., Weight:147±36lbs). For each hip, the femur and pelvis bony geometry were manually segmented from high resolution CT-scans (0.6mm slice thickness). Anatomic landmarks were manually identified on the femur and pelvis, then used to reorient the bones into their respective anatomic coordinate systems as follows: Coordinate systems were assigned to the pelvis with the anterior-posterior (A-P) axis perpendicular to a plane defined by the anterior superior iliac spines and mid pubis point. For the femur, the superior-inferior axis was defined along the femoral mechanical axis and rotationally aligned to the femoral epicondylar axis in the transverse plane. The origins of the pelvis and femur coordinate systems were at the acetabular center and femoral head center, respectively.

The pelvic attachment of the capsule was assumed to attach just beyond the labrum and was automatically extracted from the acetabular bone (Figure 4.3) (Telleria et al., 2014; Tsutsumi et al., 2019). Nodes were identified circumferentially along the apex of the acetabular rim, excluding the acetabular notch. A plane was fit to these rim nodes, which were then projected onto the plane and an ellipse was fit to the projection. The femoral attachment of the capsule was assumed to follow the intertrochanteric crest (Wingstrand et al. 1997). The intertrochanteric crest was approximated by fitting a plane through the

superior apex of the greater trochanter (a), the apex of the lesser trochanter (b), and a third point (midpoint of a and b projected on the anterior aspect of the femur) (Figure 4.3). The plane was translated along the femoral neck axis until the original midpoint of a and b reached the femoral neck surface (Zhang et al., 2020). The femur nodes lying on this plane were extracted and fit with an ellipse.

To facilitate the PCA, 360 nodes were equally spaced along each ellipse starting at the most superior point. PCA was performed on the 3D coordinates of the nodes (Sarkalkan et al. 2014). The first four principal components (PCs) accounted for 77% of the capsule attachment site variability and were used to define the capsule geometry in subsequent probabilistic analyses (Table 4.1). Thus, new attachment geometries were reconstructed by multiplying PC scores with corresponding PC vectors and then summing them with the mean coordinates.

4.2.4 Probabilistic Model Representation

A probabilistic analysis was performed on the FE model of the hip capsule incorporating variability in both the capsule mechanical properties and attachment sites. The 500-trial Monte Carlo simulation used Latin Hypercube sampling to select the capsule parameters from Table 4.2. The sixteen independent input variables included six capsule stiffnesses, six capsule pre-strains, and four PC scores of the capsule attachment sites. Each sample was selected from a normal distribution representing 95% of the population. The mean and standard deviations for the capsule mechanical properties (stiffness and pre-strain) were determined based on ten calibrated specimen-specific models from a previous study (Anantha Krishnan et al., 2023).

Isolated torques were applied to the femur in internal, external, abduction, and adduction rotations while the hip was flexed to 0°, 30°, 45°, 60°, and 90° (20 total simulations). The applied torques followed a ramp waveform between 0Nm and 5Nm starting from neutral femoral rotations. The resulting rotations in each direction were recorded at 1Nm of torque, corresponding to the slack-to-stiff transition of the capsule, and at 5Nm torque. The probabilistic analysis resulted in a dataset of 500 independent trials relating 16 capsule properties to 40 laxity metrics.

4.2.5 Ligament Parameter Prediction on the Probabilistic Data

The 500-trial dataset was randomly divided with 90% of trials (n=450) assigned to a training set and the remaining 10% reserved for validation (n=50). From that data, multivariate regressions were performed. Inputs to the regression model were the 40 hip laxities (i.e. hip rotations at 1Nm and 5Nm) and the 4 PCs defining the capsule attachment site. These variables were considered inputs to the model because they could be measured either pre-operatively (e.g. bony geometry from a CT scan for capsule attachments) or intraoperatively (e.g. hip laxity). The regression model outputs were the 12 capsule mechanical properties (stiffness and pre-strain for each capsule section). The multivariate regression took the general form,

$$p^{k(1..12)} = \sum_{i=1}^{N} (l_i \times L_i) + \sum_{i=1}^{4} (p_i \times PC_i)$$

where p^k represents the kth capsule parameter, l_i represents the i^{th} regression coefficient of the hip laxity parameters L, p_i represents the i^{th} regression coefficient of the attachment PC score, and N represents the number of laxity parameters used in the training set (Table 4.3).

The regression coefficients were calculated using stepwise regression, which entails a systematic approach of adding and removing terms from a general linear model based on their statistical significance in explaining the response parameters (*stepwiselm* function, Matlab, MathWorks, Natick, MA).

To check for convergence, five multivariate regression models were created based on training sets with 100, 200, 300, 400, and 450 trials. The regression models were used to predict the capsule mechanical parameters for each trial in the validation set (50 trials). FE models were then evaluated with the predicted capsule parameters and the known attachment site PCs to calculate the corresponding FE-model hip laxities. Root mean square errors (RMSE) were calculated between the laxity predictions from the FE models and the corresponding laxity inputs to the regression models. Increasing the training set size from 400 to 450 trials resulted in a modest reduction in the overall RMSE and was thus considered converged (Figure 4.6a). The full training set of 450 trials was used in all subsequent analyses.

The full training set included a comprehensive set of laxity measurements that may be burdensome to measure intraoperatively. Some of these laxity measurements may not be necessary to accurately predict the capsule's mechanical properties. To evaluate the contribution of each laxity measurement to the overall accuracy of the capsule predictions, regression models were trained using different combinations of laxity data. Variations in the training set included only training on I-E or Ad-Ab laxities, only training on laxity measured at 0° and 90° flexion, and along with mid-flexion (45°). The different laxity measures included in each input set are shown in Table 4.3. The model validation was repeated to calculate RMSEs between the input laxity and FE laxity using the predicted

capsule properties. Student t-tests were performed to detect significant RMSE differences between the baseline model and the 8 alternate training sets ($p<0.05$).

4.2.6 Ligament Parameter Prediction on Experimental Data

The details of the experimental cadaveric hip laxity characterizations can be found in our previous study and are explained briefly here: Five hips underwent bilateral THA using dual mobility implants. Pre- and post-operative CT scans were taken to assess the anatomy and alignment of the bones and implants. The laxity of the hip capsules was experimentally characterized using a dynamic joint simulator (AMTI, Watertown, MA). A motion capture system tracked the movements of the pelvis and femur during testing. Hip internal and external laxity was evaluated between 0Nm and 5Nm of torque at 0°, 30°, 60°, and 90° flexion.

The experimental data collection did not include laxity measurements at 45° flexion or Ad-Ab laxity measurements at any flexion angle, which were used in the development of the regression models described above. So, only the two trained regression models which were trained on laxity measures similar to the experiment (corresponding to sets 2 and 8) were tested on the experimental data. The hip laxity data and capsule attachment sites for five experimental specimens were used to predict the capsule mechanical properties using the above two trained regression models. The predicted capsule parameters were evaluated in the specimen-specific FE model to evaluate the resulting hip laxity. The RMSE and correlation coefficients (R^2) between the measured and FE-model predicted hip laxities were calculated to evaluate the accuracy of the regression models.

4.3 Results

4.3.1 Shape Function Model of Hip Capsule & Probabilistic Model

PCA of the capsule attachment sites revealed that the first four modes of variation cumulatively accounted for 77% of the variability across the population (PC1: 36.8%, PC2: 18.0%, PC3: 13.0%, PC4: 9.1%). Visualizing the attachment sites (Figure 4.4), the first PC corresponded to the overall scaling of the size of the hip capsule with some contribution to the version angle of the acetabulum rim. PC2 describes dominantly the AP translation of the intertrochanteric crest. PC3 explains the variation of the intertrochanteric crest geometry in the SI direction while the fourth PC dominantly describes the scaling and version angle of the acetabular rim in addition to its contribution to the scaling of the intertrochanteric crest (Figure 4.4).

The mean (± 1 standard deviation) laxity response from the 500 probabilistic trials are reported in Figure 4.5. Mean external hip rotation increased from 25.2±11.3° at 0° hip flexion to 47.5±6.1° at 90° flexion under the 5 Nm torque. Conversely, internal hip rotation decreased from 35.7±6.7° in extension to 22.5±20.0° in flexion. The highest overall I-E range of motion (77.5°) was observed at 60° hip flexion. Hip abduction laxity also increased with increasing hip flexion, ranging from 32.5±5.8° at 0° flexion to 54.4±6.1° at 90° flexion. Similarly, the hip ad-ab range of motion was largest at 60° hip flexion (85.3°). The highest variability in the model's laxity response was observed in the deepest flexion for both Ad-Ab and I-E laxity. The internal rotation standard deviation was 20.0° and the adduction rotation standard deviation was 14.4° at 90° hip flexion.

4.3.2 Regression Model Training, Validation & Testing

The performance of the regression model improved when increasing the number of trials in the training set. The overall RMSE decreased from 2.3°±1.1° to 1.8°±0.8° when the training set increased from 100 to 450 trials (Figure 4.6a). A percentage change in RMSE of <5% was considered as a measure of convergence which was achieved by the 450 trials case (RMSE change of 4.2% between 400 trials and 450 trials). The average model training time for each set of laxity measures was ~720 seconds while the model inference time was in the order of milliseconds.

The mean RMSE in laxity predictions varied depending on the types of laxity included in the training set (Figure 4.6b and Figure 4.7). The lowest composite RMSE of 1.8°±0.8° was achieved when all laxities were included in the training set (i.e., Set 1). The RMSE increased when trained on only Ad-Ab (2.3°±0.9°) or I-E (2.2°±0.6°) laxities at all flexion angles. Prediction accuracy was preserved when the regression model was trained on datasets that replaced 30° and 60° hip flexion with only 45° hip flexion (Set 4: 1.8°±0.4°). However, the accuracy was significantly reduced when either Ad-Ab or I-E laxities were excluded from this regression model (i.e., Training sets 5 and 6). Even models trained only on 0° hip flexion and 90° hip flexion data (Set 7) were able to maintain the same accuracy (1.8°±0.6°) as that of the models that used all the laxity data (set 1).

The overall prediction accuracies of the regression models were lower for the experimentally measured cadaveric hip laxity. The regression model trained on I-E laxity at all flexion angles (set 2) predicted the cadaveric laxity with a RMSE of 4.5°±0.2° (Range: 4.2° to 4.8°). The accuracy was reduced when the regression models were trained only on data from 0° and 90° hip flexion (set 8): 4.8°±0.2° (Range: 4.5° to 4.9°). Despite

the higher RMSE compared to the validation cases, there were strong correlations between the model predicted and experimentally measured hip laxity with from $R^2 = 0.98$ and 0.97 (Figure 4.8). Likewise, the FE models using capsule parameters predicted by the regression model performed on par with FE models developed using an optimization algorithm from our previous study, which had an average RMSE of 5.0° (Anantha Krishnan et al. 2023).

4.4 Discussion

The current study developed a framework to calibrate an FE model that accurately predicts the capsule's laxity across a broad flexion range without the need for time consuming optimization algorithms (Figure 4.2).

Laxity data required for calibration

Different sets of laxity measures were used to train the models and the models which used only Ad-Ab and IE laxity at 0°, 45° and 90° flexion (Set 4: 1.8°) showed similar accuracy as that of the model that was trained on all the laxity measures (Set 1: 1.8°). In addition, the model that used only Ad-Ab and IE laxity at 0° and 90° flexion (Set 7: 1.8°) also didn't compromise in terms of accuracy. This implies that a model trained only on 16 parameters can predict the laxity response with the accuracy same as the model trained on all 40 parameters. This behavior could be explained by the recruitment of all ligament sectors in one DOF or another when tested across the entire flexion range leading to their contribution getting captured in the significance level check of the response parameter during the systematic regression. For instance, ligament recruitment patterns have shown that sectors 1&2, 1&6, 1&6, and 4&5 act as a dominant restraint at external rotation (at 0° flexion), external rotation (at 90° flexion), internal rotation (at 0° flexion), and internal

rotation (at 90° flexion) respectively with minor contributions from other sectors (Anantha Krishnan et al. 2023). Similarly, ligaments corresponding to sectors 3&4, 1&2, 1&2, and 2&3 offer rotational restraint during abduction (at 0° flexion), abduction (at 90° flexion), adduction (at 0° flexion), and adduction (at 90° flexion) respectively (van Arkel et al. 2014).

When either Ad-Ab or IE laxity was removed from the training data, the RMSE showed a statistically significant increase compared to the baseline (set 1) case (Figure 4.6). This response is because the model did not fully recruit all sectors leading to a lack of significant correlations and ended up getting rejected by the regression model when it trains by adding and removing predictors. In other terms, when the model was only trained on IE data, the resulting models had higher errors in the Ad-Ab DOF and vice versa (Figure 4.7). Despite the higher RMSE, the errors were still in the acceptable range to be used in a clinical setting. So future experiments planning to calibrate hip capsule models can test for laxity at 0° and 90° flexion, and that data is sufficient to develop models to explain a more comprehensive flexion range.

Prior hip capsule modeling

Only a few studies have employed computational models to understand the hip capsule's physiological structure-function relationship, evaluate surgical techniques for capsule management, or investigate THA implant contact mechanics. Elkins et al. developed a deterministic model of a single implanted hip capsule and calibrated the material properties to match an experimental load-distraction curve (Elkins et al., 2011). They subsequently used the model to parametrically evaluate the effects of changes in capsule thickness, attachment, incisions, and repairs on the capsule's resistance to

dislocation. Myers et al. developed a probabilistic representation of the implanted hip capsule and optimized the ligament properties to match literature-reported average torque-rotation curves (Myers et al., 2020). The average model was subsequently used in a parametric study to evaluate the effects of femoral stem offset, jump distance, and liner constraint on dislocation resistance (Myers et al., 2022). Employing these same models for patient-specific surgical planning and intraoperative decision making is primarily limited by the computational resources and experimental data required to tune these models to represent each patient's unique anatomy. The proposed statistical calibration in the current study directly addresses this prior limitation.

Applicability in surgical decision making

The hip capsule is the primary restraint against hip dislocation in extreme ranges of motion. An experimental study showed that smaller-diameter femoral heads post-THA reduces the wrapping of the hip capsule, decreasing the capsule's ability to resist hip rotations (van Arkel et al., 2018). Clinical studies have shown reduced dislocation rates and improved patient-reported outcomes with the repair of the hip capsule (Sun et al., 2020, Owens et al., 2021). However, other studies have demonstrated that most THA patients have stable hips without capsule repair, particularly when using the direct anterior approach (Batailler et al. 2017). THA components with increased constraint, like lipped liners or dual mobility constructs, can effectively mitigate the risk of dislocation, but the indication for using increased constraint remains unclear. In most cases, constrained liners or dual mobility constructs are reserved for revision surgeries (Vajapey et al. 2020). Risk stratification tools for dislocation are primarily based on non-modifiable risk factors like patient demographics, neurological disease, or previous spine surgery (Wyles et al. 2022).

While directly responsible for resisting hip dislocation, the function of the hip capsule is rarely considered when evaluating dislocation risk in primary THA surgery. Incorporating computational models of the hip capsule into intraoperative planning software would provide surgeons with a quantitative method to assess the risk of dislocation and evaluate implant configurations and alignments to mitigate that risk.

However, the hip capsule management was left to the surgeon's discretion during the surgery. Integrating a mean population capsule into the existing surgical planning and decision-making workflow may not capture patient-specific details like ligament attachment sites which dictate the forces transmitted by different sectors of the capsule for a given bone-implant relative orientation and the capsule-implant interaction limiting the patient-specific dislocation behavior (Anantha Krishnan et al., 2023). In other words, ligament wrapping is nonlinear and patient specific. The current study is a step toward integrating a patient-specific capsule model into the surgical workflow. Once implemented, these models could inform implant choice and targeted surgical positioning that optimizes the range of motion in which the capsule is taut (dislocation envelope) and identify capture repair strategies that restore capsule tension to a pre-surgical state.

Surrogate modeling techniques

Developing instantaneous models via surrogate models using finite element calculations for a limited number of training sets and then rapidly providing estimates of new cases has increased adaptation by the orthopedic biomechanics community. Several surrogate modeling techniques like principal component regression (Fitzpatrick et al. 2011), Bayesian modeling (Bah et al. 2011), artificial neural network (Taylor et al. 2017), and random forest (Donaldson et al. 2015) which predict complex biomechanical

parameters which are otherwise computationally intensive to evaluate have been reported in the literature. For instance, Fitzpatrick et al. developed regression-based surrogate models for predicting micromotion at the bone-implant interface in cementless total knee replacement (Fitzpatrick et al. 2014). Their models were reported to achieve an inference time of 30 seconds compared to a traditional FE analysis which took 15 hours to evaluate the same conditions. Ziaeipoor et al. used regression modeling to predict femoral strains during various activities of daily living (Ziaeipoor et al. 2019). Their models were able to reduce the inference time to 0.1 seconds compared to 66 seconds per time instance for a standard FE analysis without compromising the accuracy. However, only a few studies explored surrogate modeling in the context of ligament parameter identification.

For instance, Bartsoen et al. used Bayesian optimization, which coupled an artificial neural network to calibrate ligament properties of the knee using kinematics data from squatting. Their parameter optimization approach took 80 hours for each knee specimen, comparable to 72 hours for the hip using a simulated-annealing algorithm in our previous study (Anantha Krishnan et al., 2023). The current study used a simple multivariate regression which, even though it took five days for training set creation, once the model is trained, new specimen-specific models can be created in a few milliseconds translating this improvement to find real-time applications. In addition, the model validation RMSE 1.76° (set 3) and test RMSE 4.5° demonstrates sufficient accuracy to be accepted in a clinical setting. Moreover, test RMSE 4.5° is comparable to the RMSE of 5.0° from our previous study, which used a traditional calibration technique (Anantha Krishnan et al., 2023). Even though the current framework uses implanted hips, it can be generalized and applied to other states like natural, different implant types, and extended to other joints.

Extending statistical calibration to native hips

The reported approach could be used to develop subject-specific models of natural hips which could act as a baseline for virtual implantation. However, this will require laxity data collected experimentally on natural hips along with natural femur geometry to perform PCA and do subsequent calibration. Future work could focus on collecting comprehensive natural hip laxity data along with geometry data to develop these models. In addition, the approach in its current form is more applicable to cadaveric testing, as measuring the abduction-adduction laxity of a live patient during surgery may not be viable. Future studies could explore the opportunity of leveraging instrumented implant trials to derive these metrics during surgery combined with statistical/ machine learning type techniques to infer laxity measures from patient geometry before surgery.

Capsule PCA discussion

Regardless of the type of joint, most probabilistic studies evaluating computational ligament responses did not include ligament attachment variability in their parameter space as identifying and parametrizing attachment sites requires a more extensive database of anatomical geometries and complex processing. For the hip capsule, while measuring the footprints of the ILFL and ISFL, Tamaki et al. report a standard deviation of 4.1 mm, 1.7 mm, 3.5 mm, and 1.1 mm for the length and width measurements of the proximal ISFL and the lateral arm of the ILFL respectively (Tamaki et al., 2020). As ligament recruitment patterns (prestrain in the parametric form) depend on the attachment site, we have processed 156 acetabulum-femur geometry pairs, performed PCA, and included them in a parametric form in our probabilistic representation. The mode of attachment site evaluated by our geometric analysis is consistent regarding qualitative variation reported in the

acetabulum and femoral neck geometries. While evaluating the shape models of the pelvis, Brynskog et al. reported that the first mode in the acetabulum corresponds to the acetabular rim's version and the second mode does not describe any variation in the acetabular rim geometry (Brynskog et al., 2021). Regarding the femoral neck geometry, Zhang et al. reported that the first mode corresponds to size variation, while the second mode accounted for variation in version angle (Zhang et al., 2014). Both studies were consistent with our prediction of modes of variation in the ligament attachment, thereby highlighting the validity of the approach (Figure 4.4).

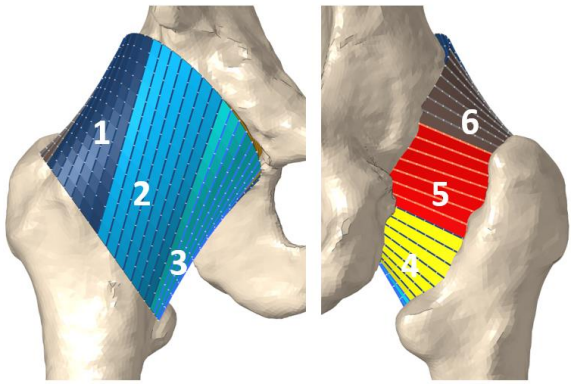

Figure 4.1: Anterior (A) and Posterior (B) views of the implanted hip capsule with numbered sectors.

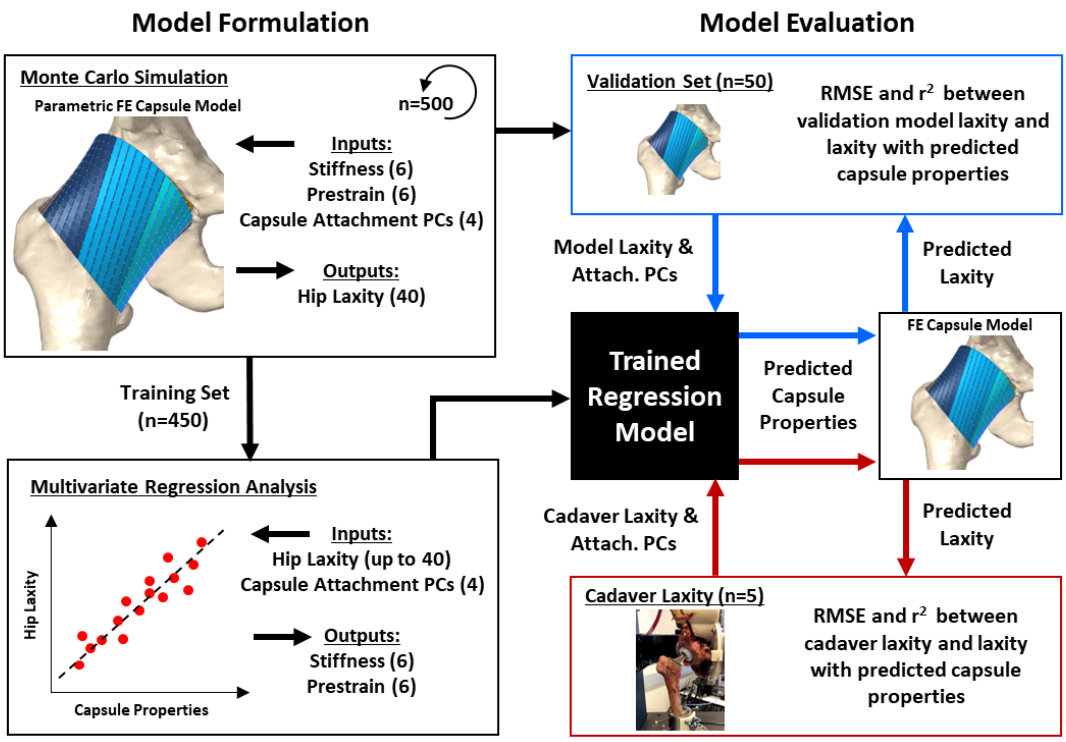

Figure 4.2: Workflow followed to develop the statistical shape function model followed by training, validation, and testing of the statistical model for the instantaneous generation of hip capsule models.

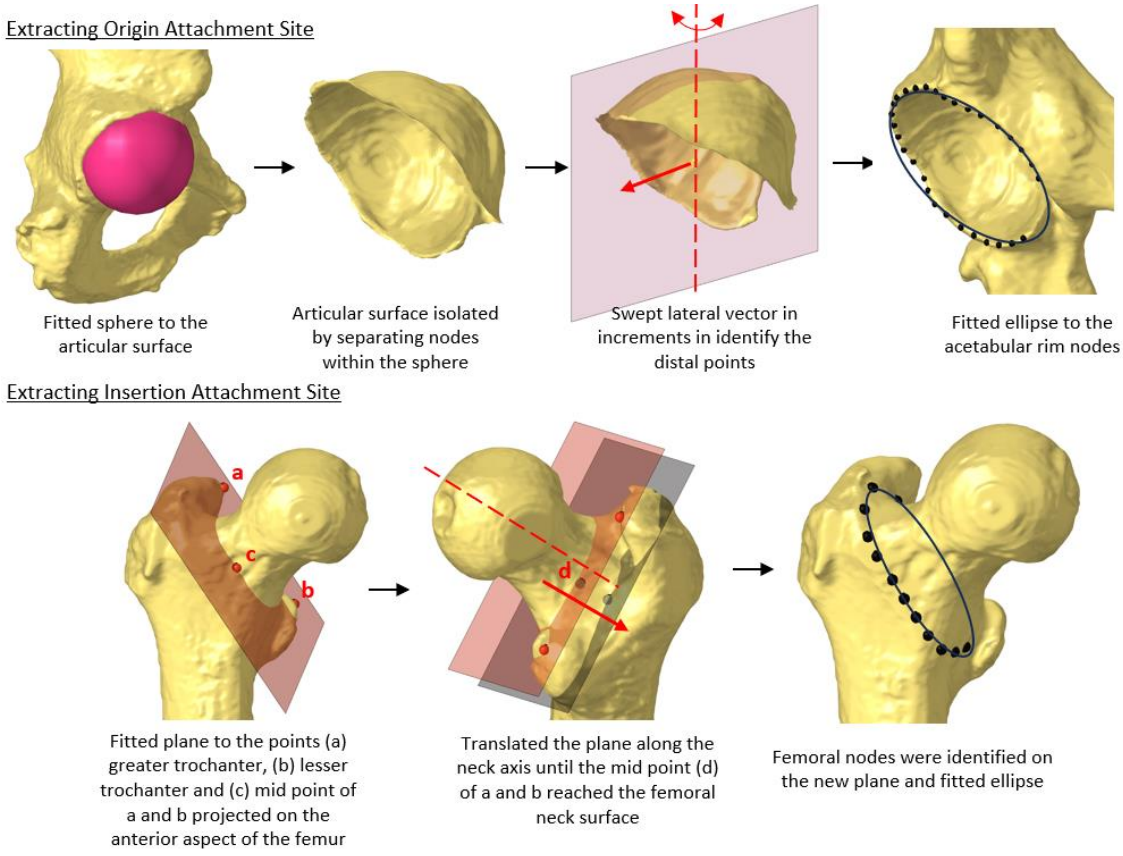

Figure 4.3: Automated workflow to identify attachment sites of the hip capsule.

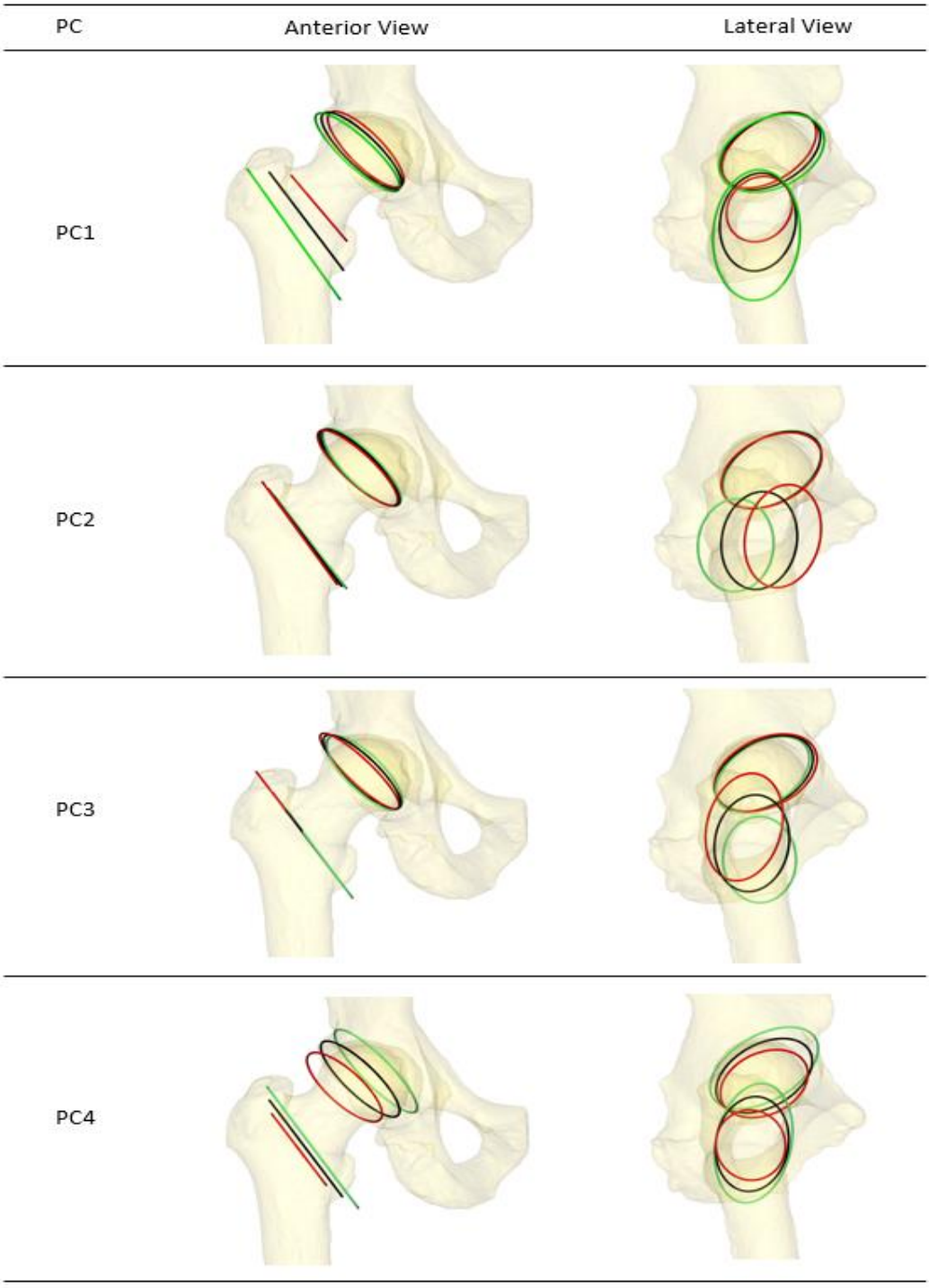

Figure 4.4: Origin and insertion of the capsule were approximated as ellipses to aid in parametrization and automation of the capsule creation. The black, red and green lines represents mean, +2SD and -2SDs of the PCs respectively.

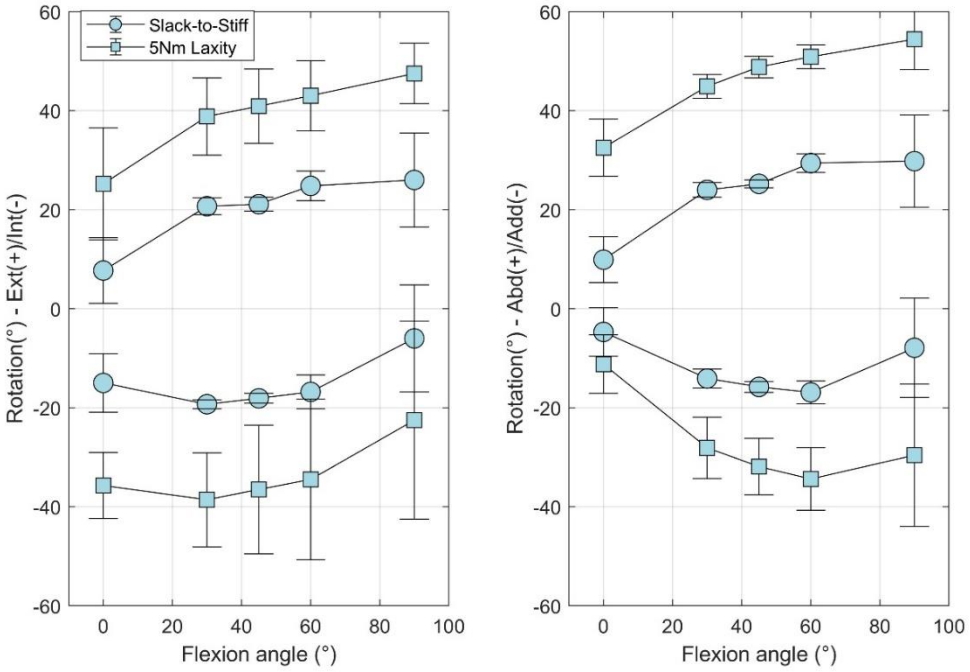

Figure 4.5: Probabilistic response of all 40 laxity parameters from the 500 trials with the error bars representing one standard deviation.

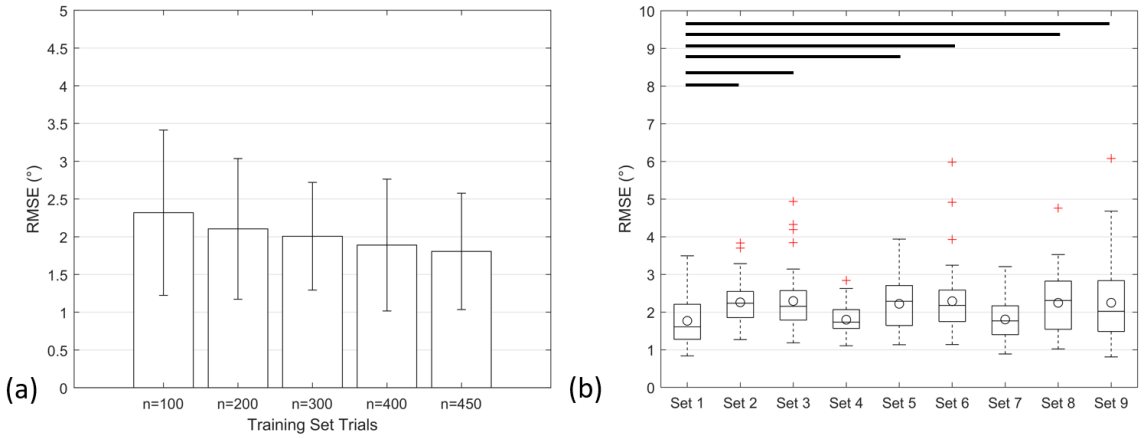

Figure 4.6: Convergence of the multivariate regression model with the cumulative RMSE decreasing as the number of trials in the training set increased (a). RMSE when using different hip laxities in the training sets (b). Horizontal bars show statistical difference in sets ($p<0.05$) with circles showing the mean RMSE.

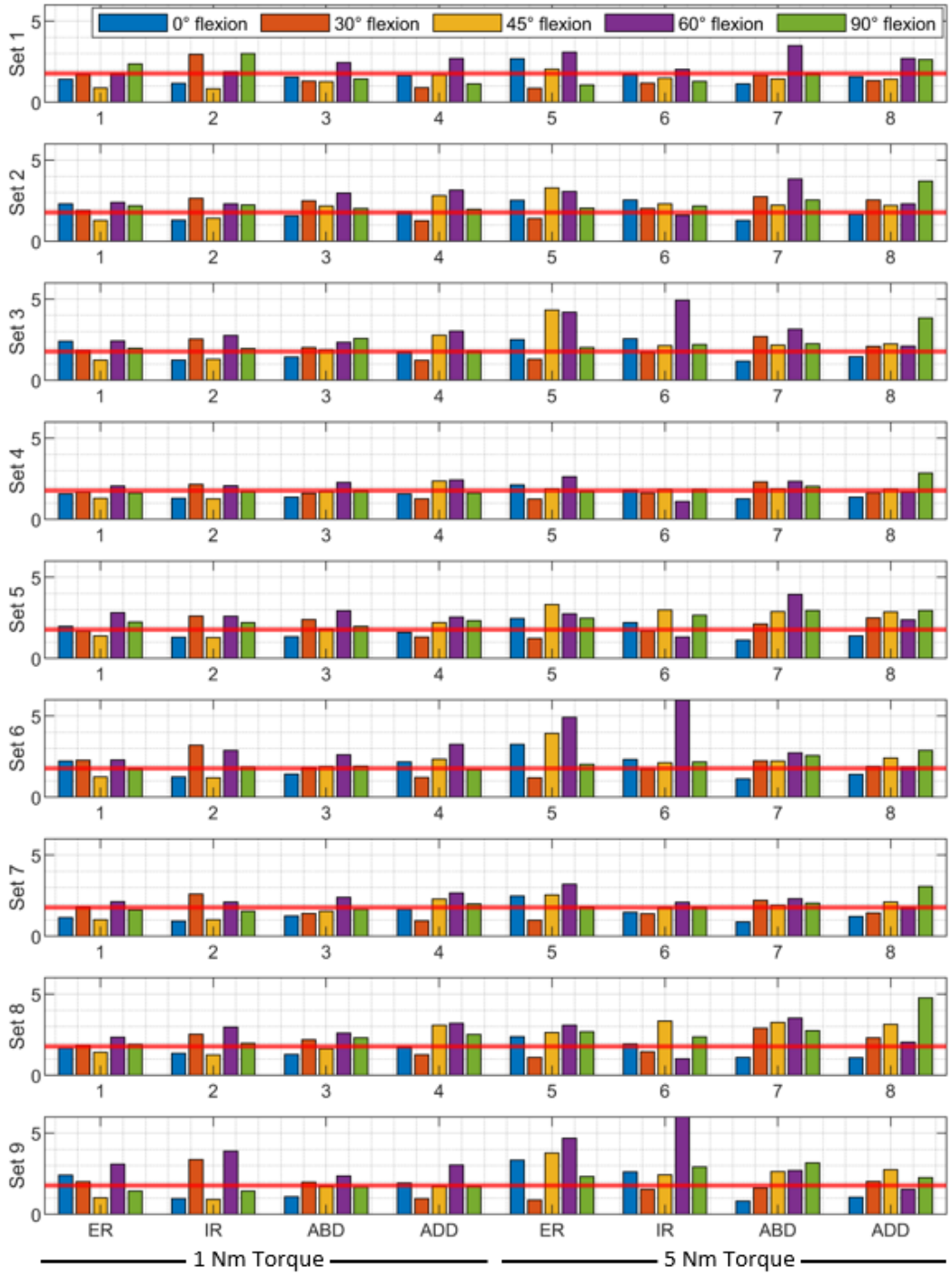

Figure 4.7: Bar chart showing the training error of all output parameters using different data sets (horizontal red line represents the mean RMSE across all 40 laxity measures).

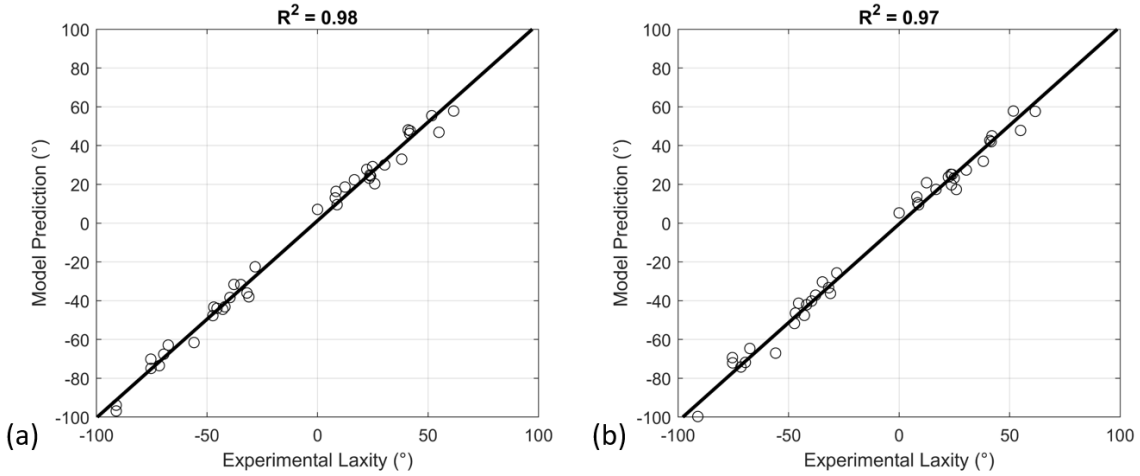

Figure 4.8: Correlation plots between experimental data and FE model's predictions (which used regression model predicted ligament parameters) for regression models trained on different sets of data (a) set 2 (b) set 8.

Table 4.1: Orientation of the attachment site ellipses with respect to the global axes.

PC (Variance Explained)		**Acetabulum (Origin)**		**Femur (Insertion)**	
		Inclination (°)	Version (°)	Inclination (°)	Version (°)
Mean		137.9	18.5	124.1	0.0
PC1 (36.8%)	+2 SD	138.5	20.7	127.2	0.0
	-2 SD	137.5	16.6	122.5	0.0
PC2 (18.0%)	+2 SD	138.0	17.7	123.3	0.0
	-2 SD	137.8	19.4	125.0	0.0
PC3 (13.0%)	+2 SD	136.6	14.4	124.4	0.0
	-2 SD	138.9	22.7	123.9	0.0
PC4 (9.1%)	+2 SD	137.5	21.7	124.4	0.0
	-2 SD	137.4	15.6	124.0	0.0

Table 4.2: Input parameters in the probabilistic model

Parameter ID	Parameter	Mean ± Standard Deviation
1	Sector 1 – Stiffness (N/mm)	61.0 ± 15.0
2	Sector 2 – Stiffness (N/mm)	62.3 ± 15.0
3	Sector 3 – Stiffness (N/mm)	58.5 ± 15.0
4	Sector 4 – Stiffness (N/mm)	53.9 ± 15.0
5	Sector 5 – Stiffness (N/mm)	70.5 ± 15.0
6	Sector 6 – Stiffness (N/mm)	50.4 ± 15.0
7	Section 1 - Prestrain	0.99 ± 0.05
8	Section 2 - Prestrain	0.71 ± 0.05
9	Section 3 - Prestrain	0.62 ± 0.05
10	Section 4 - Prestrain	0.57 ± 0.05
11	Section 5 - Prestrain	0.48 ± 0.05
12	Section 6 - Prestrain	0.57 ± 0.05
13	Attachment Region PC1	± 2.0
14	Attachment Region PC2	± 2.0
15	Attachment Region PC3	± 2.0
16	Attachment Region PC4	± 2.0

Table 4.3: Different sets of laxity parameters were used in the training set to identify the minimal number of parameters required to achieve accuracy comparable to the baseline model.

Training Set	**Laxity used in the training set**	**Hip Flexion Angles (Deg)**	**Input Parameters (N)**
Set 1	I-E Laxity & Ad-Ab Laxity	0, 30, 60, 90	32
Set 2	I-E Laxity	0, 30, 60, 90	16
Set 3	Ad-Ab Laxity	0, 30, 60, 90	16
Set 4	I-E Laxity & Ad-Ab Laxity	0, 45, 90	24
Set 5	I-E Laxity	0, 45, 90	12
Set 6	Ad-Ab Laxity	0, 45, 90	12
Set 7	I-E Laxity & Ad-Ab Laxity	0, 90	16
Set 8	I-E Laxity	0, 90	8
Set 9	Ad-Ab Laxity	0, 90	8

CHAPTER 5. EXPERIMENTAL VALIDATION OF A COMPUTATIONAL KNEE SIMULATOR

5.1 Introduction

Total knee arthroplasty (TKA) is a common treatment for end-stage osteoarthritis and other degenerative diseases of the knee. Restoring patients' natural joint kinematics is important for patient satisfaction, joint stability, and implant survivorship (AOS, 2018; Sharkey et al., 2002). While most studies on TKA mechanics focus on the tibiofemoral (T-F) joint, patellofemoral (P-F) mechanics directly influence patient satisfaction and knee stability following TKA (AOS, 2018; Sharkey et al., 2002; PM et al., 2017; Sharma et al., 2008) with patellar mal-tracking and pain being the most common causes of revision (Sharkey et al., 2002; Browne et al., 2005; Piedade et al. 2009). In vivo P-F mechanics are influenced by quadriceps muscle forces and lines of action, resection of the patella and implant alignment, the articulating geometry, repair of the lateral retinaculum, and T-F kinematics (Sharma et al., 2008; Browne et al., 2005; Mizuno et al., 2001; Salem et al., 2021). Development and testing of new TKA components to improve patient function typically requires in vitro simulation of realistic in vivo joint loading to enable pre-clinical measurement of dynamic knee kinematics and stability. Realistic loading would ideally

utilize simultaneous loading of the T-F and P-F articulations in a physiologically relevant manner.

Early whole knee experimental simulators, like the Oxford-style knee loading rig, used a linear actuator attached to the quadriceps tendon to counteract a vertical load applied through the hip (Zavatsky et al., 1997). This style of simulator allows unconstrained movement at the knee, including the P-F joint, but is limited in its ability to control loading in each of the knee's degrees of freedom (DoF) simultaneously and independently. Advancements to Oxford-style rigs include the addition of loaded degrees of freedom at the ankle to simulate approximated ground reaction forces and control systems to simulate dynamic activities (Navacchia et al., 2018; Maletsky et al., 2005). In contrast, robotic-arm based systems leverage the end-effector of a robotic arm coupled with a loadcell to apply kinematics to the knee while measuring the resulting joint loads. Recently, robotic simulators have included cables with weights or actuators to simulate muscle forces (Grantham et al., 2020; Navacchia et al., 2020; Willing et al., 2019; Herrmann et al., 2012). Robotic-systems have the unique ability to independently control loading in each of the knee's degrees of freedom but are limited in their capacity to apply dynamic force-controlled loading to the knee as seen in common activities of daily living (Noble et al., 2010; Lee et al., 2014; Bates et al., 2015).

The physical limitations of experimental simulators can be overcome using computational models. Advancements in finite element (FE) analysis and musculoskeletal modeling have led to improved computational tools to predict knee mechanics and are commonly used during the pre-clinical evaluation of new TKA designs (Halloran et al., 2005; Hume et al., 2019; Navacchia et al., 2016). These models can evaluate component

designs under dynamic loading conditions that would otherwise be difficult and costly to achieve experimentally. Godest et al. developed a finite element replicating the Stanmore knee simulator and verified the resulting kinematics against the experiment. Guess et al. developed a multibody dynamic model of the Kansas Knee Simulator, which was verified against predictions for patellar tendon load, T-F ROM of V-V, I-E rotation, and M-L translations. Baldwin et al. developed a finite element-based model of the Kansas Knee Simulator. They verified the 6DOF P-F, T-F kinematics, and actuator loading during deep knee bend and gait activities. Such models incorporate sophisticated control systems that more closely approximate the human neuromuscular system (Razu et al., 2018; Harris et al., 2016; Anijs et al., 2022) and tissue representations that enable the prediction of ligament tensioning and bony remodeling (Ziegler et al., 1993; Grood et al., 1983).

As these models' capabilities exceed their experimental counterparts' capabilities, model verification becomes challenging. This increased capability imposes limitations on their potential applications in regulatory filings as rigorous verification and validation is required to meet regulatory standards. So, we attempt to develop a simulator model (digital twin) and comprehensively verify their joint loading predictions in addition to kinematics. Thus, the purpose of this study was to develop a novel experimental simulator to evaluate knee mechanics, capable of simultaneous dynamic load-control of T-F and P-F joints, and to experimentally validate a corresponding FE model to complement the experimental measurements.

5.2 Methods

The experimental setup is described in Behnam et al. 2023 in detail (Journal of Biomechanical Engineering - under review). In brief, … AMTI VIVO …<describe in a couple of sentences>.

5.2.1 Experimental Protocol

A series of controlled loading conditions were applied to the synthetic bones to investigate force transfer through the knee and to enable subsequent computational model validation with a neutral patellar tendon length. During the isolated quadriceps loading profile, a quadriceps load was applied via the quadriceps tendon following a cosine waveform ranging from 100 N to 1000 N at 15°, 30°, 45°, and 60° knee flexion. During quadriceps loading, a tibial compressive load of 200 N was held constant, and the remaining DoF at the knee (I-E, Ad-Ab, M-L, A-P) maintained zero force or torque in load control. The 200-N compressive load was sufficient to maintain bicondylar contact of the knee implants while still allowing translation of the tibia relative to the femur in response to the quadriceps loading. Three cycles of the sinusoidal loading profile were applied and the P-F reaction force at peak loading was averaged across cycles.

During the simple deep knee bend (DKB), a 500 N quadriceps load was applied through the quadriceps tendon as the knee dynamically flexed and extended following a cosine wave from 0° to 80° while a 200 N compressive load was applied to the tibia. Although smaller than the quadriceps loads typically observed during a DKB in vivo, the 500-N quadriceps load was sufficient to ensure articulation between the femur and patella while not overloading the triaxial loadcell embedded below the patella. The tibial I-E rotation was constrained at 0° in displacement control and the remaining tibiofemoral axes

(A-P, M-L, and Ad-Ab) were maintained at zero force or torque. Five cycles were performed for each loading condition at a rate of 0.015 Hz while T-F and P-F loads and kinematics were recorded. T-F kinematics were further analyzed by calculating the location of the closest points on the femur implant's medial and lateral condyles to the plane of the tibial resection (i.e., lowest-points). Kinematics and loadings were averaged across cycles. The simple DKB loading conditions were repeated with the patella in alta and baja positions.

5.2.2 Computational Model & Validation

A dynamic FE model of the experimental setup was developed in Abaqus Explicit (Dassault Systèmes, Vélizy-Vilacoublay, FR, Figure. 5.1) based on a previously verified model of a stock AMTI VIVO simulator (Fitzpatrick et al. 2016). The simulator's fixtures, synthetic bones, and implants were meshed using triangular shell elements (Type: S3R) and modeled as rigid bodies. The mean edge length for non-articulating components (bones and fixtures) was 1.5 mm., while the edge length for the articulating implant elements was 0.5 mm based on a previously published convergence study on knee kinematics (Halloran et al. 2015). The total number of surface elements in the model were 145,480 (non-articulating components) and 147,727 (articulating components). Contact interactions between the femur, patella, and tibial implants were defined using a previously verified pressure-overclosure relationship with a friction coefficient of 0.04 (Halloran et al. 2015).

The straps representing the quadriceps ligament and patella tendon were modeled as deformable quadrilateral membrane elements (Type: M3D4R) with an axial length of 6 mm and transverse width of 3 mm (140 total elements). The membrane elements were

reinforced with link-type connector elements (Type: CONN3D2, link) along the strap axis, thus making the strapping inextensible. The proximal and distal ends of the patella ligament strap were attached to the patella fixture and tibial tuberosity, respectively, via hinge connector elements (Type: CONN3D2, hinge) to allow relative rotation in the sagittal plane. Likewise, the distal end of the quadriceps tendon was attached to the proximal aspect of the patella fixture in the same fashion and the proximal end was attached to the quadriceps actuator. The experiment's quadriceps actuator was modeled with a corresponding connector element (Type: CONN3D2, translator). A final connector element was embedded between the patella implant and the patella fixture (Type: CONN3D2, bushing) to measure the loads experienced by the patella during contact with the femur corresponding with the 3-axis loadcell used in the experiment.

The loads applied to the knee by the VIVO simulator in the experiment were controlled via virtual coordinate systems aligned to the implant geometry using a three-cylindric open chain configuration described by Grood and Suntay (Grood et al. 1983). To recreate the applied loading, a series of three mutually orthogonal connector elements (Type: CONN3D2, cylindrical) were aligned to the same virtual coordinate systems in the model. The first connector element was affixed to the tibia along the tibial S-I axis and oriented to allow S-I translation and I-E rotation of the knee. The second connector element was affixed to the M-L axis of the femur and oriented to allow M-L translation and F-E rotation of the knee. The third connector element connected the first two virtual axes and was oriented along a vector mutually orthogonal to both axes, coinciding with A-P translation and Ad-Ab rotation of the knee. Load-sensing connector elements (Type: CONN3D2, bushing) were embedded between the distal end of tibial S-I axis and the tibial bone to

measure the loading experienced by the tibia corresponding to the 6-axis tibial load cell in the experimental set-up and between the tibial tray and insert to measure the T-F reaction forces. Note that the tibial reaction force and T-F contact force are different due to the forces exerted on the tibia by the patella tendon. A virtual proportional-integral (PI) control system was incorporated into the FE model that replicated the control algorithm of the experimental simulator. Forces and moments measured by the tibial load-sensing bushing were inputs to the PI controller via a user subroutine (VUAMP) and used to control load profiles for the connectors modeling the VIVO's actuators. The control system's proportional and integral gain parameters were tuned via a previously published method (Fitzpatrick et al. 2014).

The meshed model was virtually aligned in the initial position relative to the VIVO simulator using the optical scan of the experimental setup thereby ensuring proper alignment of the fixtured assembly with respect to the simulator's actuators. Anatomic coordinate systems were defined in the model on the femur, tibia, and patella components using equivalent definitions to the experiment, which facilitated a direct comparison of T-F and P-F kinematics throughout the analyses. The same experimental boundary conditions were evaluated in the model, including the isolated quadriceps loading with the neutral patella position and the simple DKBs with the patella in baja, neutral, and alta positions. During each simulation, patella loads and knee kinematics were compared against the experimental measurements, and the Root Mean Square errors (RMSE), normalized Root Mean Square Error (nRMSE), mean errors (ME), and standard deviations (STD) of the differences were calculated.

Computational Model Sensitivity Analysis

Unlike the single synthetic bone used in the experimental component of this study, there is significant variability in quadriceps mechanism geometry across the potential patient population that affects knee mechanics. A model sensitivity analysis was performed to quantify the effect of variability in the quadriceps mechanism on uncertainty in the resulting kinematics and joint loads. The five alignment parameters considered in the sensitivity were the A-P position of the patellar tendon insertion, the patella alta-baja position (controlled by the patella tendon length), the patella composite thickness, the quadriceps muscle sagittal plane angle (controlled by the A-P position of the superior attachment of the quadriceps actuator), and the quadriceps muscle frontal plane angle (Q-angle, controlled by the M-L position of the superior attachment of the quadriceps actuator, Figure. 5.2). Based on published studies of extensor mechanism geometry across the patient population, the standard deviation from the mean for these alignment parameters were 2.5 mm, 5.0 mm, 3.0 mm, 2.5°, and 2.5°, respectively {Mizuno et al. 2001, van Eijden et al. 1985, Blackburn et al. 1977, Reuben et al. 1991).

Perturbations in the alignment parameters were applied to the model's nominal alignment with the neutral patella position using the Monte Carlo method with sampling from normal distributions via Latin Hypercube Sampling (100-trials). The resulting T-F and P-F kinematics and loads during the simple DKB were evaluated. The range of flexion during the simulated DKB was extended to 120° flexion to quantify deep flexion behavior not measured experimentally. Correlation coefficients and corresponding slopes between the five input quadriceps variables and output knee mechanics were calculated. Output variables included P-F kinematics, P-F loading, T-F S-I loading, patella tendon load, quadriceps moment arm, and quadriceps elongation at 15°, 60°, and 120° knee flexion. The

quadriceps moment arm was calculated by dividing the quadriceps elongation over a 6° flexion window centered on the flexion angle of interest by the corresponding change in flexion (in radians).

5.2.3 Model Verification

The same experimental boundary conditions were evaluated in the model, including the isolated quadriceps profile with the neutral patella position and the simple DKBs with the patella in baja, neutral, and alta positions. During each simulation, patella loads and knee kinematics were compared against the experimental measurements, and the Root Mean Square (RMS) differences were calculated.

5.3 Results

5.3.1 Model Accuracy

The FE model T-F kinematic predictions were found to be sensitive to changes in patella tendon length, predicting the same increased posterior translation of the tibia in the patella alta condition as observed experimentally (Figures. 5.3, 5.4 and 5.5). Overall RMSEs for kinematic predictions across patella conditions were less than 3.3° and 1.4 mm (Table 5.2). T-F V-V rotations and S-I translations achieved the best prediction accuracies, with average RMSE of 0.4° and 0.3 mm, respectively. The worst prediction accuracies were for T-F I-E and M-L, with average RMSE of 1.6° and 1.6 mm, respectively. Femoral low point translation predictions were most accurate when predicting S-I translations and least accurate for predicting M-L translations, for both the medial and lateral condyle. Average RMSEs for A-P translation were 1.0 mm and 0.9 mm across all patella configurations and each condyle, respectively (Table 5.2). The experimental kinematics

trends were also observed in the FE model, resulting in accurate kinematic predictions through the flexion range (Figs. 5.4 and 5.5). RMSEs in FE model P-F kinematics predictions across all conditions were less than 3.3° and 1.4 mm (Table 5.2). The best prediction accuracies were achieved for P-F V-V rotations and A-P translations, with average RMSE of 1.2° and 0.8 mm, respectively. The worst prediction accuracies were for P-F I-E and M-L, with average RMSE of 2.8° and 1.3 mm. RMSEs in FE model P-F force predictions averaged 21 N and ranged between 7.4 N and 53.6 N across patella heights (Table 5.1).

P-F loading during the simplified DKB followed similar patterns to the isolated quadriceps loading profiles, with the P-F A-P reaction force increasing with knee flexion (Figure 5.6). Increasing the patella tendon length (patella alta) resulted in larger peak A-P forces, ranging from 470 N to 653 N for baja and alta cases, respectively. Increasing the patella tendon length also caused the S-I component of the P-F reaction force to change from -109 N in the inferior direction to 176 N in the superior direction for baja and alta conditions, respectively. In the neutral patella configuration, the S-I load oscillated between superior during flexion and inferior during extension, likely due to friction at the P-F articulation. P-F M-L reaction forces were consistently the smallest in magnitude and acted in the lateral direction. RMSEs in FE model P-F force predictions averaged 21 N and ranged between 7.4 N and 53.6 N across patella heights (Table 5.3).

5.3.2 Model Sensitivity

The model's sensitivity to the variation in the quadriceps geometry changed through flexion (Figure 5.7). Variation in the tuberosity A-P position had no significant correlations

(correlation coefficients > 0.6) with knee mechanics. Patella alta was directly correlated to P-F superior translation through flexion and to P-F M-L translation in mid-flexion due to articulating higher in the angled trochlear groove. Likewise, patella alta caused an increase in the superior component of the P-F reaction force that propagated through the patella tendon, causing higher T-F S-I loading (7.6 N/mm of increased patella alta). In deep flexion, patella alta caused reduced P-F flexion and more anterior loading through the patella. Increased patella thickness was directly correlated with more anterior P-F translation. This caused an increase in the quadriceps moment arm in early and mid-flexion along with increased quadriceps elongation to reach mid and deep flexion (additional 1.5 mm of elongation per 1.0 mm of increased patella thickness). Increased patella thickness was also strongly correlated to higher P-F superior loading which propagated through the patella tendon into T-F compressive load. The sagittal angle of the quadriceps had weak correlations with P-F kinematics in extension that dissipated with increasing flexion. Likewise, increased sagittal quadriceps angle reduced P-F loading in early and mid-flexion. The frontal plane angle of the quad was strongly correlated with P-F M-L translation and V-V rotation in extension, prior to full engagement with the trochlear groove, and an increase in the P-F M-L reaction force once the patella was constrained within the trochlear groove in mid and deep-flexion.

5.4 Discussion

The purpose of this study was to develop a novel whole knee loading apparatus capable of controlling six DoF T-F loads while simultaneously loading the P-F joint through a simulated quadriceps mechanism. To expand the capabilities of the experiment,

a complementary FE model was developed that incorporated the same mechanisms and control system as the physical rig and was validated against the experimental measurements. The model accurately predicted changes in T-F and P-F mechanics when altering the patella height during a simplified DKB activity. The integrated control system of the complementary FE model will be used to develop increasingly sophisticated boundary conditions that enable future cadaveric simulation of patient-specific and implant-specific whole knee loading conditions.

While the primary focus of the study was model development and validation, the variations in patella height tested in the experiment provided insight into patellar mechanics and extensor mechanism efficiency. Patella baja, or pseudo-patella baja, is a common complication of TKA and has been associated with poor outcomes (Tischer et al., 2022; Ward et al., 2005; Fitzpatrick et al., 2016; Baldwin et al., 2012). Multiple studies have demonstrated the effects of patella height on patella kinematics, patella loading, and extensor mechanism efficiency with conflicting results (List et al., 2020; Dreyer et al., 2022; Willing et al., 2018). In a similar experimental study, Luyckx et al. developed an oxford-style knee loading apparatus and evaluated TKA P-F contact forces with different patella heights (Dreyer et al., 2022). Unlike the current study, the quadriceps load was variable to create a constant vertical ground reaction force at the ankle and not held at a constant value (e.g., 1000-N). Between 30° to 70° knee flexion, patella alta resulted in lower P-F contact forces compared to patella baja, indicating an increase in the extensor mechanism efficiency. Ward et al. compared extensor efficiency in vivo between healthy subjects with normal or alta patellae using magnetic resonance imaging and observed that patella alta caused an increase in the effective moment arm of the extensor mechanism

from 0° to 60° knee flexion (Ward et al., 2005). In contrast, Tischer et al. investigated TKA P-F mechanics using a musculoskeletal model and found patella alta resulted in an increase in patella contact force that persisted through the full flexion range (Tischer et al., 2022).

In the current study, the patella alta condition had lower P-F reaction forces between 20° and 50° knee flexion coupled with higher T-F joint compressive loads (Figure. 5.8), indicating more quadriceps force was being transmitted from the quadriceps actuator through the patella, and into the patella tendon. Beyond approximately 60° flexion, wrapping of the quadriceps strap on the femur's trochlear groove was observed in the neutral and baja conditions, which offloaded the patella articulation. As a result, the patella alta condition had the highest PF reaction forces at 80° flexion of 135% of the applied quadriceps load, compared to 110% and 101% for the neutral and baja conditions. Similarly, the model sensitivity analysis identified direct correlation between patella alta and the superior component of the P-F reaction force in mid-flexion, which propagated into an increased T-F reaction force. Although not directly calculated, an increase couple between the patella tendon force and T-F reaction force would increase the knee extension moment resulting in increased extensor efficiency. These results are consistent with the findings of Luyckx et al. and Ward et al. that patella alta improves extensor mechanism efficiency through mid-flexion but also increases patella loading in deeper flexion (Luyckx et al. 2009, Ward et al. 2005).

T-F and P-F FE model prediction errors in the current study were less than 3.3° and 2.1 mm for knee rotations and translations, respectively. Errors for T-F A-P translations ranged from 0.5 mm – 2.1 mm across patella heights, while T-F I-E errors ranged from 1.7° - 2.2°. These accuracies are comparable to previous literature-reported studies with

FE models of experimental knee simulators. In our previous work, we formulated a simpler FE model of the VIVO simulator configured for knee tribological testing. When modeling the rigidly fixtured femur and insert, RMS errors were less than 1.7 mm and 1.4° for T-F A-P translation and I-E rotation, respectively. The accuracy in the current study was similar despite the increased modeling complexity of the quadriceps mechanism and compliance in the larger mechanical components of the simulator. Baldwin et al. predicted implanted P-F kinematics in cadaveric specimens loaded with the Kansas Knee Simulator and achieved an accuracy of 1.6 mm and 2.6° for P-F translations and rotations, respectively (Behrend et al., 2019). In a subsequent study using the same experimental set-up, Baldwin et al. simultaneously predicted implanted T-F and P-F kinematics in cadavers performing a deep knee bend, achieving RMS errors of 2.1 mm and 1.3° for T-F A-P translation and I-E rotation, respectively (Baldwin et al., 2012). Unlike the current study, kinematic predictions in cadaveric tissue require modeling the knee's ligaments and patella retinaculum. While this adds complexity to the model, it also enables tuning the soft tissue properties to recreate the measured knee kinematics more closely. Future work using cadaveric tissue to develop patient specific computational soft-tissue models will further enhance the capabilities of the combined tool developed here.

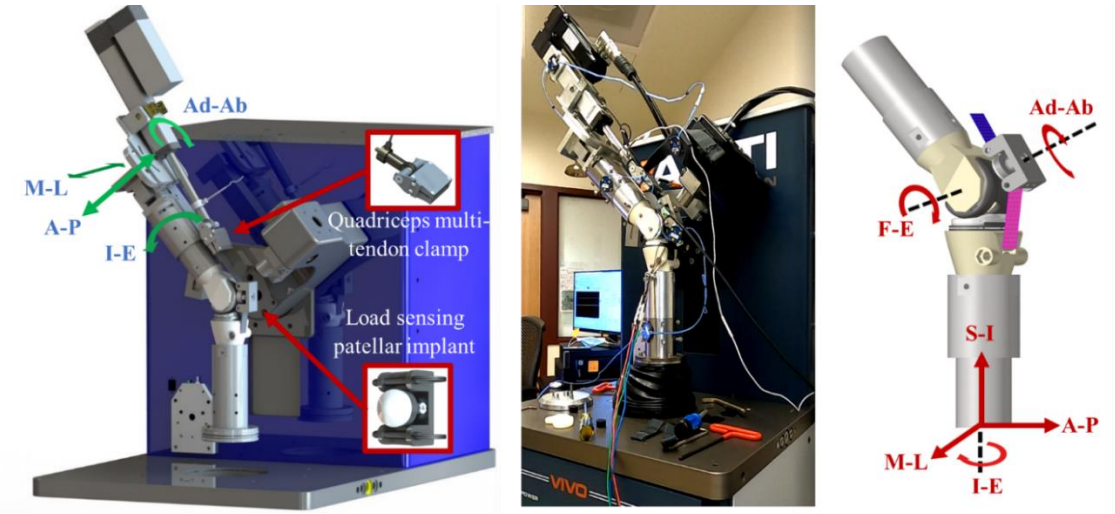

Figure 5.1: Model of modified VIVO joint simulator retrofitted with custom fixturing and quadriceps actuation assembly (left); joint simulator setup with fixtured TKA in synthetic bones (middle); finite element model of experimental configuration (right). Axes labeled in blue highlight adjustment capabilities of the femoral fixture relative to the femoral CS. Axes labeled in red are controlled by the joint simulator relative to the tibial CS.

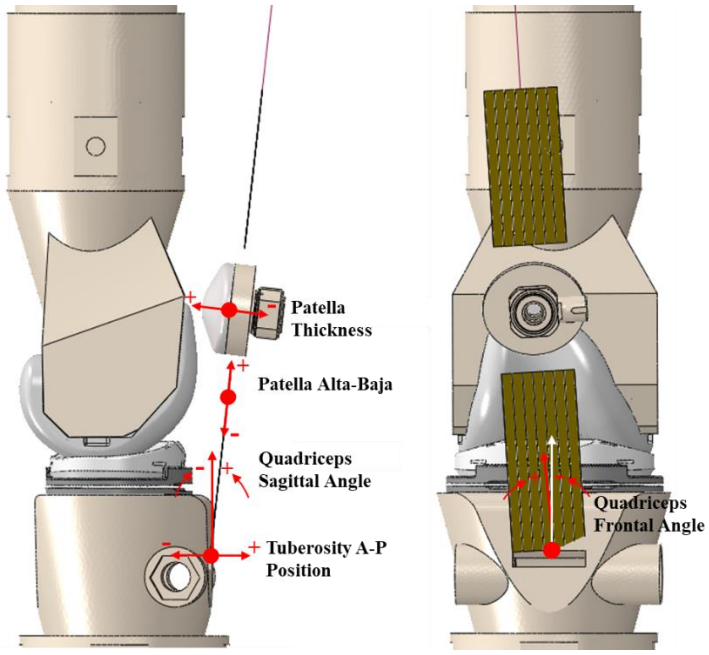

Figure 5.2: Finite Element model of the experimental configuration and the five alignment parameters that were perturbed in the sensitivity analysis.

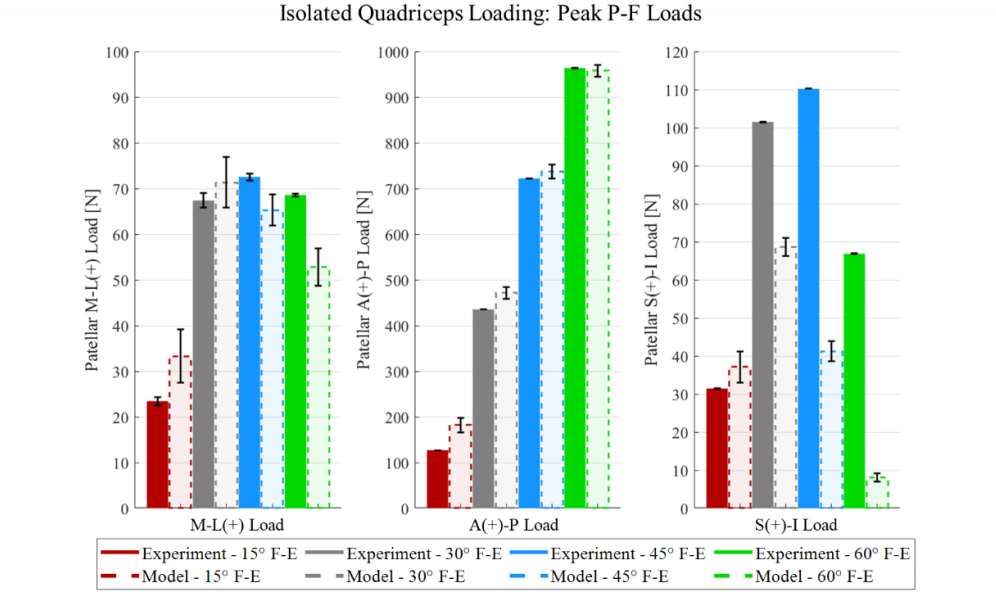

Figure 5.3: Mean patellofemoral reaction forces with 1000 N applied quadriceps force observed experimentally and predicted by the FE model at different knee flexion angles. Error bars indicate 1 standard deviation from the mean peak force during 3 experimental cycles and 100 iterations from the model's sensitivity analysis.

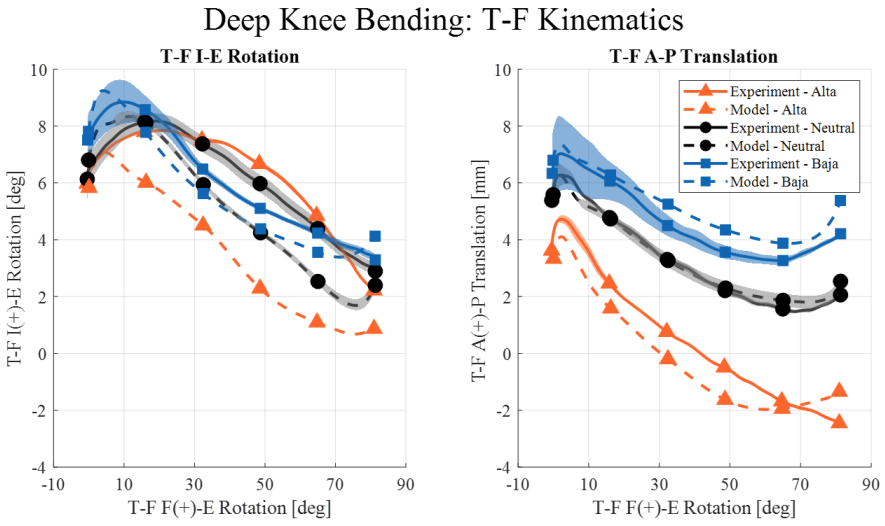

Figure 5.4: Experimental and Model tibiofemoral kinematics during a simple Deep Knee Bending activity. Shaded regions highlight 1 standard deviation from the mean.

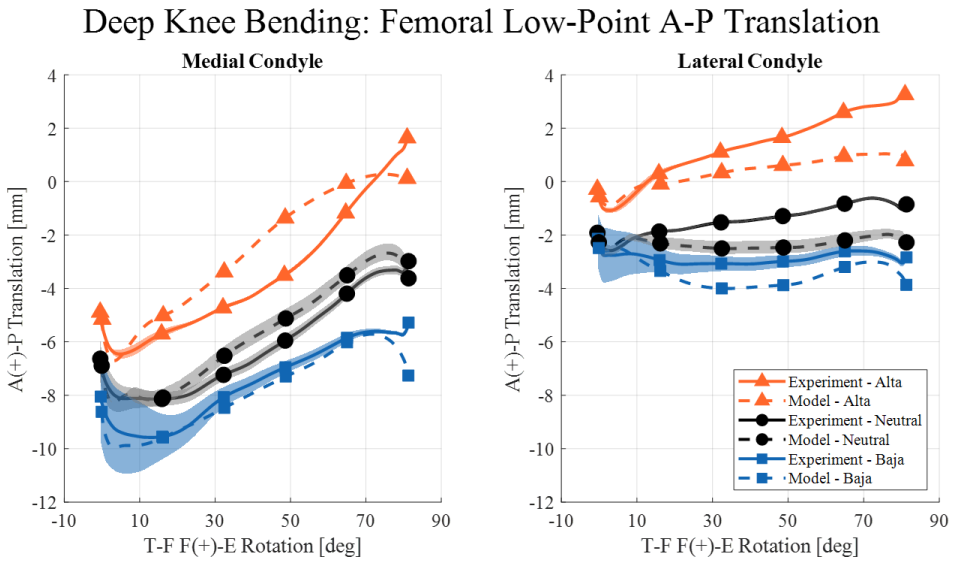

Figure 5.5: Femoral low-point A-P translation during the simple Deep Knee Bending activity. Experimental (solid) and computational (dashed) results are shown with *alta*, *neutral*, and *baja* tendon lengths. Shaded regions highlight 1 standard deviation from the mean.

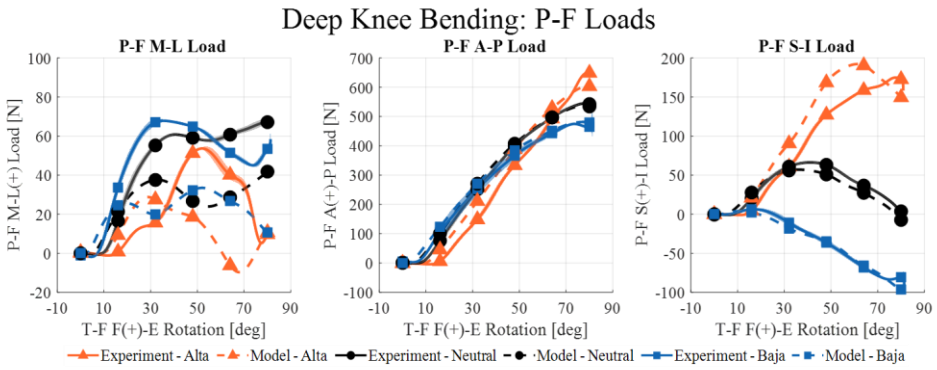

Figure 5.6: Experimental (solid) and Model (dashed) patellofemoral loads during the simple Deep Knee Bending activity for the alta, neutral, and baja tendon lengths. Shaded regions highlight one standard deviation from the mean.

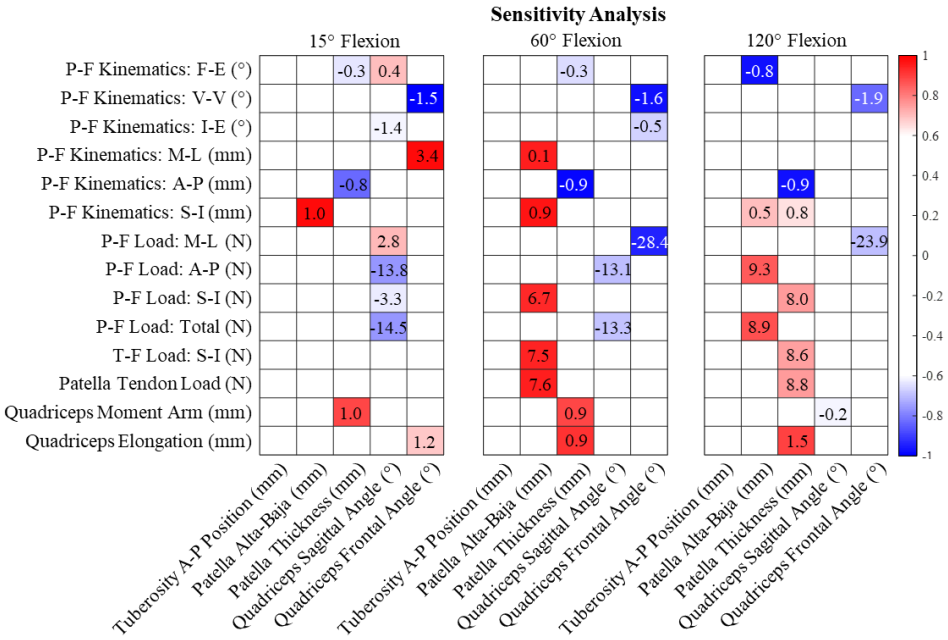

Figure 5.7: Correlations between the FE model alignment perturbations and resulting knee mechanics at various flexion angles during a deep knee bend. Red regions indicate positive correlations while blue regions indicate negative correlations. Correlations less than 0.6 are shown in white. The slope of the linear fit is inset for variables with correlations greater than 0.6.

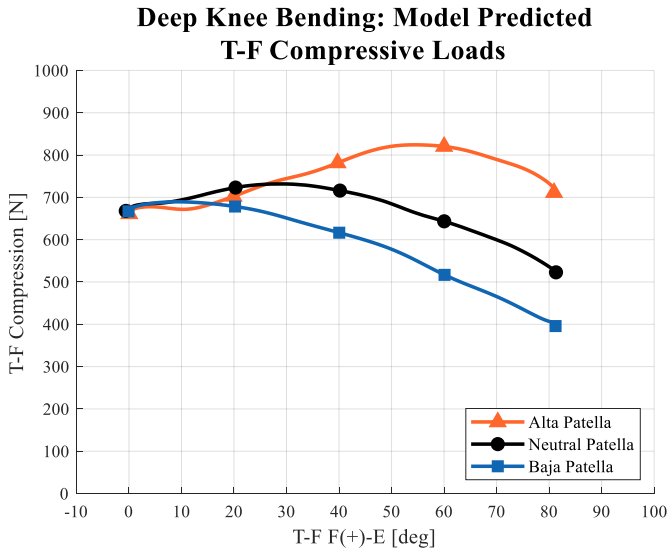

Figure 5.8: Model-predicted tibiofemoral loads during the simple Deep Knee Bending activity for the alta, neutral, and baja tendon lengths.

Table 5.1: Peak patellofemoral Root Mean Squared Error (RMSE), Mean Absolute Error (MAE) and Standard Deviation (STD) of the error between experimental and model patellofemoral loads during sinusoidal loading of the quadriceps while knee flexion angle was held constant at 15°, 30°, 45°, and 60°.

Knee Flexion		**M-L**				**A-P**				**S-I**		
		RMSE	MAE	STD		RMSE	MAE	STD		RMSE	MAE	STD
15°		5.6	3.8	4.1		34.9	-24.7	24.7		5.2	-3.6	3.8
30°		5.2	-2.5	4.6		36.6	-7.3	35.9		20.5	17.1	11.3
45°		9.8	-9.0	3.9		49.9	11.0	48.7		42.6	35.7	23.4
60°		15.8	-15	5.1		65.7	26.9	60.0		40.6	33.5	22.9

Table 5.2: Root Mean Squared Error (RMSE), Mean Absolute Error (MAE), and Standard Deviation (STD) of the error between experimental and model tibiofemoral (T-F) and patellofemoral (P-F) kinematics during the simple Deep Knee Bending activity with alta, neutral, and baja tendon lengths.

			Rotations (deg)									
			F-E				**V-V**				**I-E**	
			RMSE	MAE	STD		RMSE	MAE	STD		RMSE	MAE	STD
T-F	*alta*		1.1	-0.4	1.0		0.4	0.1	0.4		2.2	1.7	1.4
	neutral		1.1	-0.4	1.0		0.4	0.4	0.1		1.3	0.2	1.3
	baja		1.1	-0.4	1.0		0.4	0.4	0.2		1.3	-0.4	1.2
P-F	*alta*		2.3	-1.7	1.5		1.5	1.5	0.5		3.3	-2.8	1.7
	neutral		0.9	-0.6	0.7		0.8	-0.6	0.6		1.7	-0.9	1.4
	baja		2.0	-1.1	1.6		1.2	-0.8	0.8		3.3	-2.9	1.5
			Translations (mm)									
			M-L				**A-P**				**S-I**	
			RMSE	MAE	STD		RMSE	MAE	STD		RMSE	MAE	STD
T-F	*alta*		1.7	1.6	0.8		0.7	0.1	0.7		0.5	0.5	0.2
	neutral		1.6	1.3	0.9		0.5	-0.2	0.4		0.3	-0.1	0.3
	baja		1.6	1.4	0.8		0.8	-0.6	0.5		0.2	-0.1	0.2
P-F	*alta*		1.3	1.1	0.7		0.8	0.2	0.8		1.2	0.2	1.1
	neutral		1.3	0.3	1.3		0.8	-0.1	0.7		0.7	0.6	0.3
	baja		1.4	1.2	1.2		0.7	0.0	0.7		1.3	0.7	1.0

Table 5.3: Root Mean Squared Error (RMSE), normalized Root Mean Square Error (nRMSE), Mean Error (ME), and Standard Deviation (STD) between experimental and model patellofemoral (P-F) loads during the simple Deep Knee Bend activity at alta, neutral, and baja tendon lengths.

	ML				AP				SI			
	RMSE	nRMSE	ME	STD	RMSE	nRMSE	ME	STD	RMSE	nRMSE	ME	STD
alta	16.8	0.3	-4.3	16.3	53.6	0.1	-27.7	45.9	25.1	0.1	-10.2	23.0
neutral	17.1	0.3	-8.5	14.9	14.7	0.0	-5.8	13.5	7.4	0.1	3.4	6.6
baja	25.4	0.4	-16.4	19.4	14.4	0.0	-9.7	10.7	14.3	0.1	5.4	13.2

CHAPTER 6. TKA CONFORMITY HAS A LARGER INFLUENCE ON KNEE KINEMATICS DURING ADLS THAN LIGAMENT TENSION

6.1 Introduction

Total Knee Arthroplasty (TKA) relieves pain and restores normal knee function. Post TKA, instability is one of the three main reasons for revision surgery (Sharkey et al., 2014; Pitta et al., 2018). Implant sizing, positioning, and soft-tissue balance are the main factors that dictate postoperative instability (Rodriguez-Merchan., 2011). For instance, implant malalignment or tight ligaments could produce unequal loads on the medial and lateral tibial plateaus and cause joint stiffness and component wear (Johnston et al., 2019). For well-balanced knees, correct Varus/Valgus (VV) alignment and equal flexion and extension gaps must be achieved (Babazadeh et al., 2009). One of the following two surgical techniques is generally followed for balancing knees (Mercuri et al., 2019). The measured resection technique uses bony landmarks for implant positioning and then adjusts the soft tissue balance by releasing the tight ligaments. The gap balancing technique uses ligament tension from tensioners as a reference for implant alignment and then adjusts the bone resection to achieve the desired balance. Regardless of the technique, soft tissue left unbalanced in the sagittal and coronal planes can lead to a plethora of complications, including abnormal kinematics, polyethylene wear, asymmetric gaps, inadequate range of

motion, recurrent effusions, bearing surface separation, or condylar lift-off, and instability (Sheth et al., 2017).

Intraoperative balancing evaluations include a VV stress test for laxity (condylar lift-off) and a distraction test for joint gaps using tension jigs, laminar spreads, and spacer blocks or inline traction (Mihalko et al., 2003). However, TKA knees were rarely reported exhibiting condylar lift-off during Activities of Daily Living (ADLs). For instance, Khasian et al. observed no condylar lift-off during gait, ramp-down activity, and deep knee bend (DKB) in a study of 35 subjects implanted with posterior-stabilized TKA fluoroscopy (Khasian et al., 2020). Argenson et al. reported that only 10% and 30% of subjects experienced condylar lift-off with a high flexion TKA at full extension and maximum knee flexion, respectively, during weight-bearing DKB in a fluoroscopy study (Argenson et al., 2005). In addition, literature studies reporting soft-tissue balancing effects on postoperative stability were predominantly reported during deep flexion activities, including lunging (Moro-oka et al., 2009), kneeling (Nakamura et al., 2015; Moro-oka et al., 2009), weight-bearing (Teeter et al., 2017; Suzuki et al., 2014) and non-weight-bearing flexion (Moro-oka et al., 2009; Suzuki et al., 2014). However, unlike other ADLs, DKB activities were observed to have lower Anterior-Posterior (AP) force and Internal-External (IE) torque loading on the joint. For instance, instrumented tibial tray measurements report that maximum AP load and IE torque experienced during sitting and squatting were 68.6%, 35.2%, and 77.2%, 38.0%, lesser than the maximum AP load and IE torque during gait (Bergmann et al., 2014). In other terms, evaluating stability under different ADLs could lead to different stability measures or reveal instability patterns not shown by DKB.

Literature studies traditionally report the effect of soft tissue balance on short-term and long-term outcomes. For example, Unitt et al. studied the influence of soft-tissue releases on the outcome of 526 total knee replacements one-year post-TKA. Extensive soft-tissue balancing improved clinical outcome scores (Unitt et al.,2008). In their two-year follow-up study, Singh et al. reported improved knee scores comparing surgical techniques. They concluded that the gap-balancing technique resulted in better functional scores than the measured resection technique (Singh et al., 2012). In addition, studies report post-TKA stability through stress tests and radiographic measurements (Seon et al. 2007, Ryan et al. 2023). However, systematic evaluation of the effect of ligament balancing on joint stability is not straightforward in these settings.

Cadaveric and computational studies can do parametric or probabilistic type studies systematically relating the degree of soft tissue balance and stability which is not possible on live patients. Salvadore et al. used ten cadaveric knees to replicate different soft tissue conditions and evaluated tibiofemoral contact forces and laxity to find conditions that replicated the natural knee (Salvadore et al., 2018). They were able to achieve implanted coronal laxity close to that natural coronal laxity by changing the medial to total force ratio on the tibial plateau (Compartmental load ratio) from 0.41 at full extension to 0.80 at 90° of flexion. Smith et al. used a subject-specific computational model to evaluate the medial-lateral compartmental loading during gait under the varying level of soft-tissue tightness (Smith et al., 2016). Their results showed tightness of the medial collateral ligament and iliotibial band had the largest effects on medial and lateral compartment loading, respectively. However, the literature needs studies evaluating and comparing stability metrics during different ADLs with varying soft-tissue balances.

Apart from surgical technique, the bearing surface type and geometry were reported to affect the stability of the TKA implant. In terms of bearing surface type, medial pivot TKA was observed to improve AP stability and anterior knee pain during revision surgery (Takagi et al. 2023). With medial pivot design, another group of studies reported improved knee scores during sit-to-stand and lunge activities (Alesi et al. 2021), improved joint scores, and range of motion (Scott et al. 2022). Even though medial pivot kinematics was observed to have favorable outcomes, over-constraining the medial side was reported to lead to lower outcome scores (Pizza et al. 2021). In terms of conformity, Thatcher et al. evaluated 14 implants with varying sagittal conformity and reported that a low-conforming implant would increase the risk of instability, soft tissue overloading, and edge-loading on components. In contrast, a high-conforming implant will lead to a reduced range of motion (Daniilidis et al. 2012) and increased interface stresses thereby increasing the risk of long-term loosening (Thatcher et al., 1987). In addition, an implant can show abnormal kinematics like paradoxical anterior motion and mid-flexion instability depending on whether it is a single radius (Grieco et al., 2016) dual radius (List et al., 2020), or multi-radius (Grieco et al., 2016) design. Such abnormal kinematics were reported to be at risk for reduction in quadriceps efficiency, anterior knee pain (Mahoney et al., 2002), and decreased range of motion (Banks et al., 1997, Heckmann et al. 2021).

Hence, this study aims to answer two questions. 1. Do high-demand ADLs like gait and stair-descent demonstrate instability differently than a DKB, depending on the level of soft-tissue balance? 2. Does implant conformity have a more significant influence on stability than the soft tissue balance during ADLs?

6.2 Methods

6.2.1 Experimental Laxity & ADL Evaluation

For experimental evaluation, four fresh frozen cadavers were implanted with the moderately conforming (ATTUNE™ CR, DePuy Synthes, Warsaw, IN) and low conforming (Triathlon™, Stryker Corporation, Kalamazoo, MI) implant by fellowship-trained board-certified orthopedic surgeons following the manufacturer's recommendation for implantation (Knees 1 & 2: PCL retained; Knees 3 & 4: PCL sacrificed). Following surgery, the knees were dissected from the cadaveric specimen prepared for experimental testing. Each knee was sequentially mounted into a verified joint simulator (Behnam et al. 2023) capable of dynamic 6 DoF knee loading via custom tubular metal fixturing, a linear actuator for simulated knee extensor loading, and potting resin. Following the completion of experimental loading for each knee with the ATTUNE™ implant, the knee implants were swapped with a size-matched Triathlon™ implant with custom fixation features to match the bone cuts of the prepared specimen.

Each knee underwent a panel of loading conditions, including varus-valgus laxity assessments followed by various dynamic activities. The varus-valgus laxity assessments torqued the knee from 5Nm valgus to 5Nm varus following a trapezoidal wave at 0°, 30°, and 60° constant knee flexion angles. Peak torques were held for 15 seconds in each direction while loading, and the following unloading ramps spanned 10 seconds each. A compressive load of 200N was applied while all the other DOFs were held in a 0 N load or torque condition for the duration of the laxity assessment. The resulting torque rotation responses were recorded. Additionally, each knee underwent dynamic simulations of activities of daily living (ADL), including gait, stair descent, and sit to stand, which

included simultaneous loading of the T-F and P-F joints. These profiles were developed experimentally on the VIVO joint simulator from *in vivo* fluoroscopic tracking data (List et al., 2020) of the ATTUNE™ knee system. For each activity, all loads were measured by a 6 DoF load cell mounted at the base of the tibial fixture and transformed to the T-F joint line. Although the joint simulator incorporates translational and rotation outputs, all translations and rotations were measured by an active-marker optical tracking system (OPTOTRAK, NDI Systems, Waterloo, ON) to define the relative transformational matrices between each implant. After experimental testing, each knee was optically scanned using a white-light laser scanner (Spyder, Artec 3D, Senningerberg, Luxembourg) for implant registration to the bony anatomy. Each ligament origin and insertion anatomical landmark was marked with permanent ink, allowing for digital identification during implant registration. The location of each origin and insertion site was then used to create an accurate virtual representation of the ligaments in the finite element model. Lastly, relative implant kinematics (Grood & Suntay, 1968) and femoral low point translations were calculated.

6.2.2 Finite Element Model

The implant CAD models were virtually implanted on the bone geometries derived from pre-operative CT scans (femur, tibia, fibula) by aligning them on the 3D scan geometry of the knees. The bones and implants were modeled as rigid bodies using triangular shell elements (average element size = 1mm) in Hypermesh (Altair Engineering Inc., Troy, MI). A nonlinear pressure-overclosure relationship with a friction coefficient of 0.04 was used to define the contact interaction between the femoral component and the

polyethylene insert (Halloran et al., 2005). Ligaments included: Anterior Lateral Structure (ALS), Lateral Collateral Ligament (LCL), PopliteoFibular Ligament (PFL), Medial Collateral Ligament (MCL), Posterior Oblique Ligament (POL), Posterior Cruciate Ligament – Anterior Lateral (PCL-AL), Posterior Cruciate Ligament – Posterior Medial (PCL-PM) and the posterior capsule (PCAP) (Figure 6.1). The collateral and cruciate ligaments were modeled using 1D nonlinear tension-only springs with their force-displacement response parametrized using prestrain (initial ligament strain) and stiffness. ALS, LCL, PFL, MCL, POL, PCL-AL, PCL-PM, and the PCAP were represented using 3, 3, 3, 3, 1, 2, 2, and 10 such springs for each side, respectively (Figure 6.1a). All springs in the ligament were considered uniform force-displacement responses except for the MCL. The anterior, mid, and posterior spring of the MCL was considered to have the same stiffness but different pre-strain (Harris et al. 2016). The PCAP was modeled using quadrilateral membrane elements with a hyperelastic material model and 1D tension-only springs embedded for reinforcement. The contact between femoral condyles and the PCAP was defined with a friction coefficient of 0.01. The attachment locations of the ligaments were considered based on specimen-specific digitized geometry. Forces were applied for all DOFs except flexion and the specimen-specific finite element (FE) models were set up in Abaqus/ Explicit (Dassault Systèmes Simulia Corp, Johnston, RI). The resulting tibiofemoral kinematics were calculated using the Grood-Suntay conventions (Grood et al., 1983).

6.2.3 Ligament Calibration

Specimen-specific ligament representation was calibrated for each knee for ligament parameters (stiffness, prestrain) and attachment locations. The calibration minimized the sum of squared differences between experimental kinematics and model predictions during VV and AP laxity assessments. Using simulated annealing optimization, calibration was performed in Isight (Dassault Systèmes Simulia Corp, Johnston, RI). Initial guesses for the ligament stiffness and prestrain values were based on literature, and they were allowed to vary within the reported range for each ligament structure (Harris et al., 2016). Ligament attachment locations were allowed to vary up to 5 mm from the reference location and only in directions that allowed the footprints to stay on the bone surface.

To ensure that the ligaments were only recruited during their intended physiological function, the calibration was performed using a sequential three-step process (Figure 6.1 b). In step one, the knee model only had ALS, LCL, PFL, MCL, and POL structures as active. A constant compressive load of 200 N load was applied via the tibia during all laxity simulations to provide a baseline joint compression replicating the experiment. Linearly increasing VV torque with a maximum of 5Nm was applied to the tibia while maintaining flexion of 0°, 30° and 60°. The Internal-External (IE), Medial-Lateral (ML), and Anterior-Posterior (AP) degrees of freedom (DOFs) were kinematically unconstrained. The parameters corresponding to active ligaments were calibrated such that the sum of squared differences between the resulting VV rotations and the VV laxity experimental dataset at an interval of 1Nm input torque (Figure 6.1 b). In the second step, the PCAP was made active in addition to the existing structures. AP laxity simulation was performed at 0° flexion with an AP load of 50 N while the VV DOF was kinematically unconstrained. The

parameters corresponding to the PCAP were calibrated such that the sum of squared differences between the resulting AP translations and the PCL resected AP laxity experimental dataset at an interval of 10 N input AP load. In the final step, PCL-AL and PCL-PM were made active in addition to the existing structures. AP laxity simulation was again performed at 30° and 60° flexion with an AP load of 50N. The parameters corresponding to both PCL bundles were calibrated such that the sum of squared differences between the resulting AP translations and the PCL intact AP laxity experimental dataset at an interval of 10 N input AP load. Thus, all ligament structures were calibrated utilizing a comprehensive experimental dataset for all four knees.

6.2.4 Replicating varying levels of Imbalance & ADL Stability Evaluation

The calibrated knee models were later used to induce varying levels of imbalance in the model representing the medial, lateral, and bicondylar gaps. The femoral component was adjusted, replicating a modified bone cut in decrements of 0.5° from 4.0° such that the femur didn't dislocate during flexion or the laxity assessment replication (Table 6.2). For instance, to induce a medial gap, the femoral component was rotated externally about the posterior-most point in the lateral condyle, and valgus rotation was applied about the inferior most point in the lateral condyle (Figure 6.3). A 4° rotation VV or ER/IR was applied, and the resulting varus-valgus laxity response was evaluated at 0° (extension) and 90° flexion. If the knee dislocated, the femoral component malrotation was reduced by 0.5° until a stable transition between flexion angles was achieved and the resulting VV laxity response was recorded. However, to achieve the bicondylar slack condition, the femoral component was translated by each amount in the anterior and superior directions.

The validated FE model of the experimental configuration (Behnam et al. 2023) was virtually implanted with these knee models with varying degrees of imbalance. Stability was evaluated on all configurations during different ADLs by replicating the boundary conditions used in testing the cadaveric specimens (Figure 6.5). The anteroposterior translation of the nearest point between the femoral component and tibial polyethylene insert for the medial and lateral sides was evaluated. The range of motion of these points was considered the measure of stability and reported. In addition, the ligament recruitment patterns were compared. Later, the moderate conforming implant was virtually replaced with a lower conforming implant, and the above-mentioned ADL evaluation process was repeated.

6.3 Results

Figure 6.2 shows that the varus-valgus laxity closely matched the model kinematics predictions with experimental data for all four knees. The VV laxity root means square error (RMSE) between model predictions and experimental data for knees 1 to 4 were 0.73°, 0.73°, 0.23°, and 1.26° respectively. Similarly, the AP laxity root means square error (RMSE) between model predictions and experimental data for knees 1 to 4 were 1.5 mm, 1.9 mm, 2.1 mm, and 1.7 mm respectively. Qualitatively, the calibrated knees were able to capture the slacker medial sides in knees 1 and 2, a well-balanced response in knee three, and a relatively slacker bicondylar VV response in knee 4. The level of femoral component rotation used to achieve different levels of balance is shown in Table 6.2. The resulting ligament response for varying levels of imbalance was shown for one of the representative knees in Figure 6.4. The corresponding comparison between experimental and model-

predicted AP-ROM for both condyles of all four knees during ADLs was reported in Figure 6.6. Across activities, Stair descent showed the highest AP-ROM for both MC (6.5±2.0 mm) and LC (10.0±1.8 mm) implants. In addition, when compared to a given activity, LC implant consistently showed higher AP-ROM than the MC implant. Both trends were tracked well by the calibrated models for MC (RMSE=2.8 mm) and LC (RMSE=2.0 mm) implants when averaged across activities.

When comparing different balance cases, the medial slack condition consistently shows increased medial ROM across all activities for both implants (an average increase of 47% and 15% for MC and LC implants respectively) (Figure 6.7). The lateral slack case shows a higher-level increase in the lateral condyle compared to the medial slack case implants (an average increase of 55% and 21% for MC and LC implants respectively compared to the baseline model). Compared to the baseline (calibrated model), bicondylar slack showed the highest increase in AP-ROM for both condyles across activities and implants (an average increase of 107% and 8% for MC and LC implants respectively compared to the baseline model). Across implants, LC implant showed higher ROM compared to MC implant regardless of the activity and level of ligament imbalance. When averaged across the condyles and ligament imbalance, it showed 26%, 39%, and 46% higher ROM for the LC implant for gait, stair descent, and sit to stand respectively. These observations were substantiated by the ligament recruitment patterns across the four knees which consistently show decreased collateral ligament recruitment for the bicondylar slack case compared to the baseline model and increased recruitment of cruciate ligament in the LC design compared to the MC design (Figure 6.8).

6.4 Discussion

A comprehensive understanding of TKA stability is essential for its long-term success. Soft tissue balance, the primary factor affecting stability, was predominantly evaluated postoperatively during deep knee bending-type activities. During surgery, balancing is achieved by combining ligament releases, component sizing, and bone resections (Griffin et al., 2000, Whiteside., 2002; Winemaker., 2002). We realigned femoral components replicating a varying levels of ligament imbalance, thereby inducing a range of unbalanced states. It has been reported that well-balanced knees exhibit superior performance compared to unbalanced knees (Unitt et al., 2008; Siddiqi et al., 2018; Romero et al., 2007). However, these studies evaluate performance using different functional knee scores. Our main contribution is establishing a relationship between varying levels of soft-tissue balance and their resulting kinematic metrics across daily activities.

The use of subject-specific models was justified by the variability in experimental laxity data captured by the models. We used a three-step calibration process to capture the contribution of individual structures through an isolated resection in the experiment and addition in the modeling. The average RMSE for VV and AP laxity for both knees were 0.73° and 2.8 mm, which were less than ~2 deg and ~3mm reported by Harris et al. in their specimen-specific FE models (Harris et al., 2016). The AP laxity errors were less than the range of 3-5mm reported by Blankevoort et al. in their 3D mathematical models (Blankevoort et al., 1996). This wider variability in modeling could highlight the inherent difficulty in capturing the response of distinct and interconnected capsular structures in all DOFs using computational models. Even though the models did not include wrapping except for the PCAP, the calibration was still a 3 to 4-day process (Step 1 = 2 days, Step 2

= 0.5 day, Step 3 = 1 day) to achieve converged models. This lengthy process might not be practically applicable if we decide to develop real-time soft tissue representations in the operating room for intraoperative guidance. Future work will use statistical/ machine learning models to build real-time representations from experimental laxity curves measured simultaneously.

The MC implant has a gradually varying sagittal radius design, while the LC implant has a single sagittal radius design. MC implant's sagittal conformity ratio (femoral sagittal radius of curvature / insert sagittal radius of curvature at the dwell point - SCR) was higher than LC implant's SCR at 0°, 30°, 60°, and 90° flexion by 133.2% 256.6%, 199.0%, and 206.5% respectively (Sintini et al. 2018). In addition, MC implant's coronal conformity ratio (CCR) was higher than LC implant's CCR at the 0°-90° flexion range by 83.2% (Sintini et al., 2018). This low SCR and CCR explain why LC implant exhibited an average of 37% higher AP-ROM than MC implant for the same ligament balance conditions regardless of the ADL (Figure 6.7). However, one of the main takeaways from this study is that stabilization provided by the condylar surfaces overpowered the stability provided by balancing the soft tissue regardless of the activity.

Our predictions were supported by the study by Luger et al., which showed that, in LC designs, soft tissues reduced laxity by up to 30%, with little to no effect for high conformity designs during their cycling loading-based laxity testing (Luger et al.,1997). Our studies show an overall average reduction of 26%, 39%, and 46% reduction in AP ROM during gait, stair descent, and sit to stand respectively for the MC design compared to the LC design. DesJardins et al. also reported a decreased AP-ROM trend in high congruity compared to low congruity design under gait loading in a 6 DOF force-controlled

simulator (DesJardins et al., 2000). For instance, they reported that Insall-Burstein I (Zimmer) implant with SCR of 0.958 and 0.416 compared to Press-Fit Condylar (Johnson & Johnson)'s SCR of 0.246 and 0.144 at 0° and 60° flexion showed a reduced AP-ROM of 3.51 mm compared to 5.74 mm by its low congruity counterpart (39% reduction). On the other hand, during gait loading, the MC design showed a reduction of 20% compared to the LC design. Detailed quantitative comparisons across the reported literature are not possible as they use ISO or ASTM-type standard loadings while we use loading derived from fluoroscopic studies.

After unbalancing, the position of the femoral ligament attachment sites relative to the femoral center of rotation changes, resulting in ligament extension leading to altered ligament recruitment. This decreased recruitment decreases joint stability, as corroborated by the soft tissue balancing study by Willing et al., showing balanced LCL and MCL exhibit reduced AP-ROM compared to slack LCL and MCL during both stance and swing phases of the gait (Willing et al., 2018). The increased ligament recruitment is extenuated by the LC implant, which offers less resistance to laxity leading to the surrounding soft tissues taking up the load (Figure 6.8). Regardless of the level of balancing, the predicted ligament recruitment patterns were qualitatively comparable to the ligament length change patterns reported in the literature for collateral (Hosseini Nasab et al., 2020a) and cruciate ligaments (Hosseini Nasab et al., 2020b).

Our study has some limitations. The ADL boundary conditions were derived based on the fluoroscopy-based low point kinematic data available for Attune (Figure 6.5). Due to the lack of fluoroscopic data for Triathlon and to exclude the effect of loading conditions, we applied the same loading to evaluate both designs. Still, our study is an accurate

representation of realistic loading conditions as the loadings were derived by matching implant-specific experimentally observed kinematics, unlike other studies that used loading based on the Orthoload database (Willing et al., 2018), cyclic loading (Sintini et al., 2018), or motion capture kinematic data (Smith et al., 2016) to evaluate stability and balancing. The study compared only two different sagittal conformity levels and reported the relative trends and their implications. Future studies will further explore the complex interplay between implant congruency and soft tissue laxity. This has potential to inform new implant designs and surgical planning that could work together to recreate kinematics closer to the natural knee.

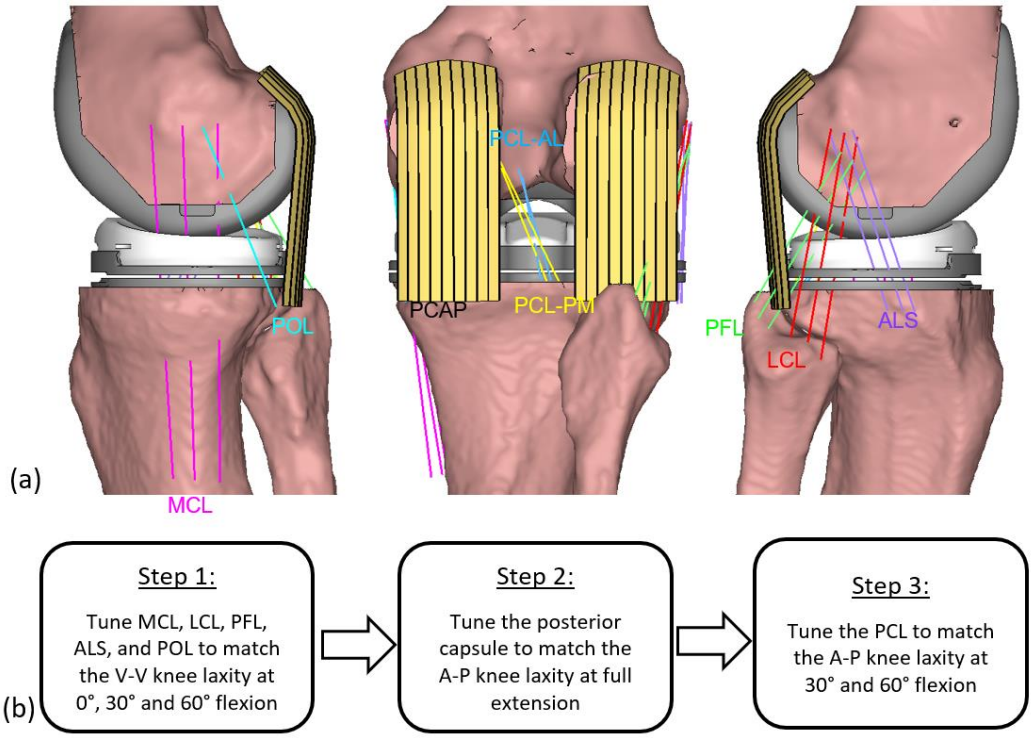

Figure 6.1: (a) FE model of a representative knee implanted with a moderate sagittal conformity showing all the ligaments used in the model calibration. (b) Flowchart showing the sequential calibration of the ligament structures.

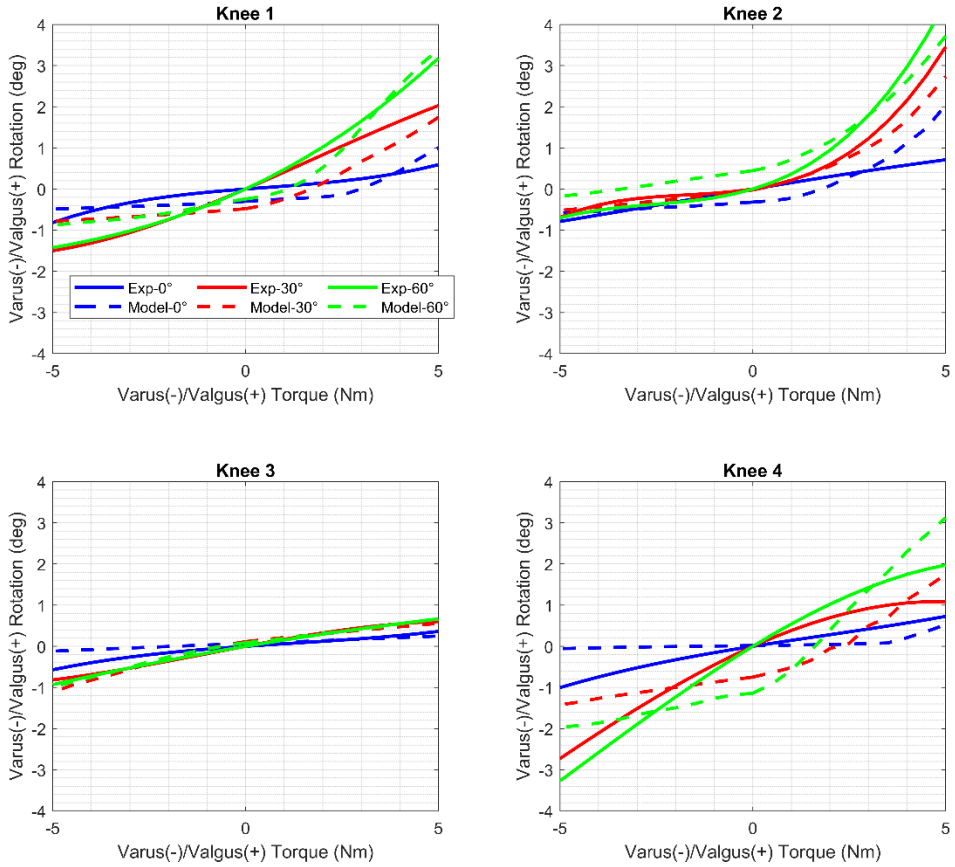

Figure 6.2: Experimental and calibrated model VV laxity curves.

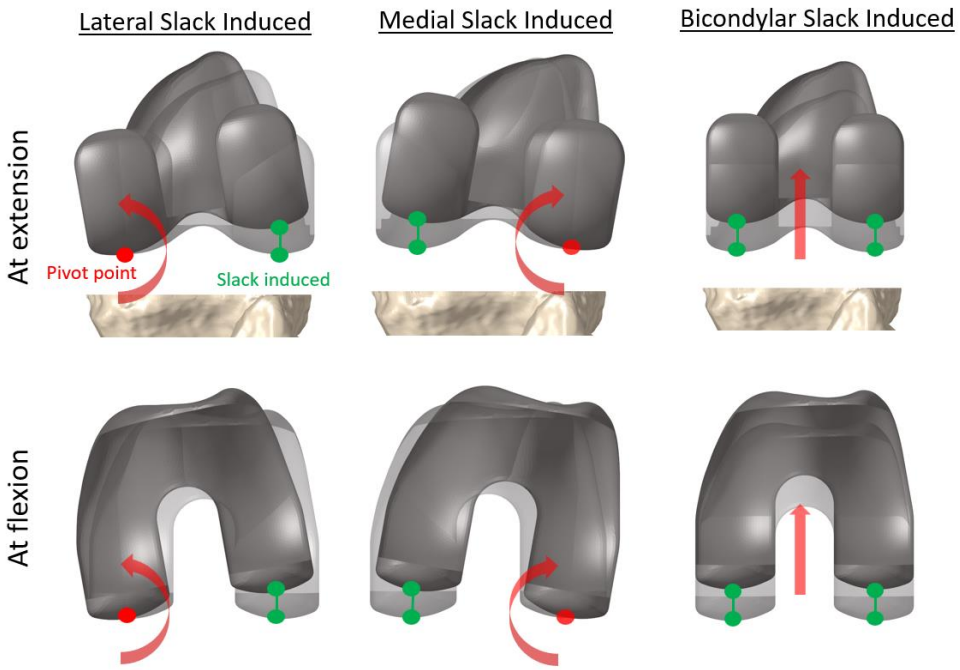

Figure 6.3: Realignment of the femoral component to achieve different levels of imbalances.

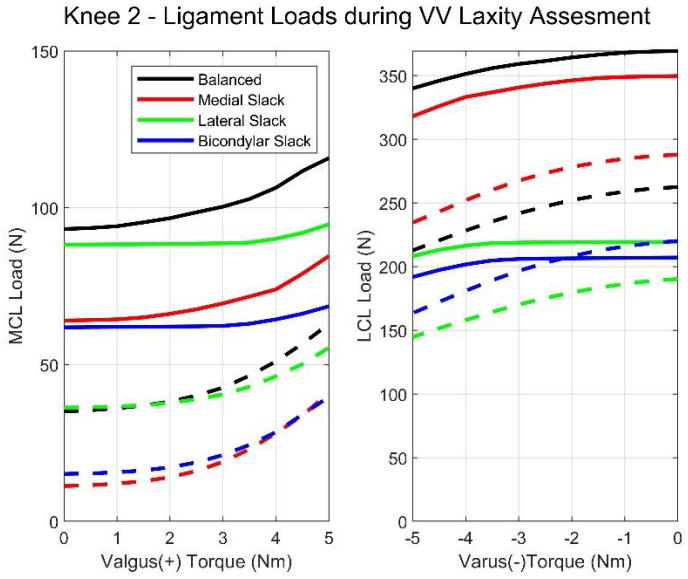

Figure 6.4: VV laxity for alternate ligament conditions for a representative model. Solid lines represent the VV laxity response at 0° flexion while the dashed lines represent the VV laxity response at 90° flexion.

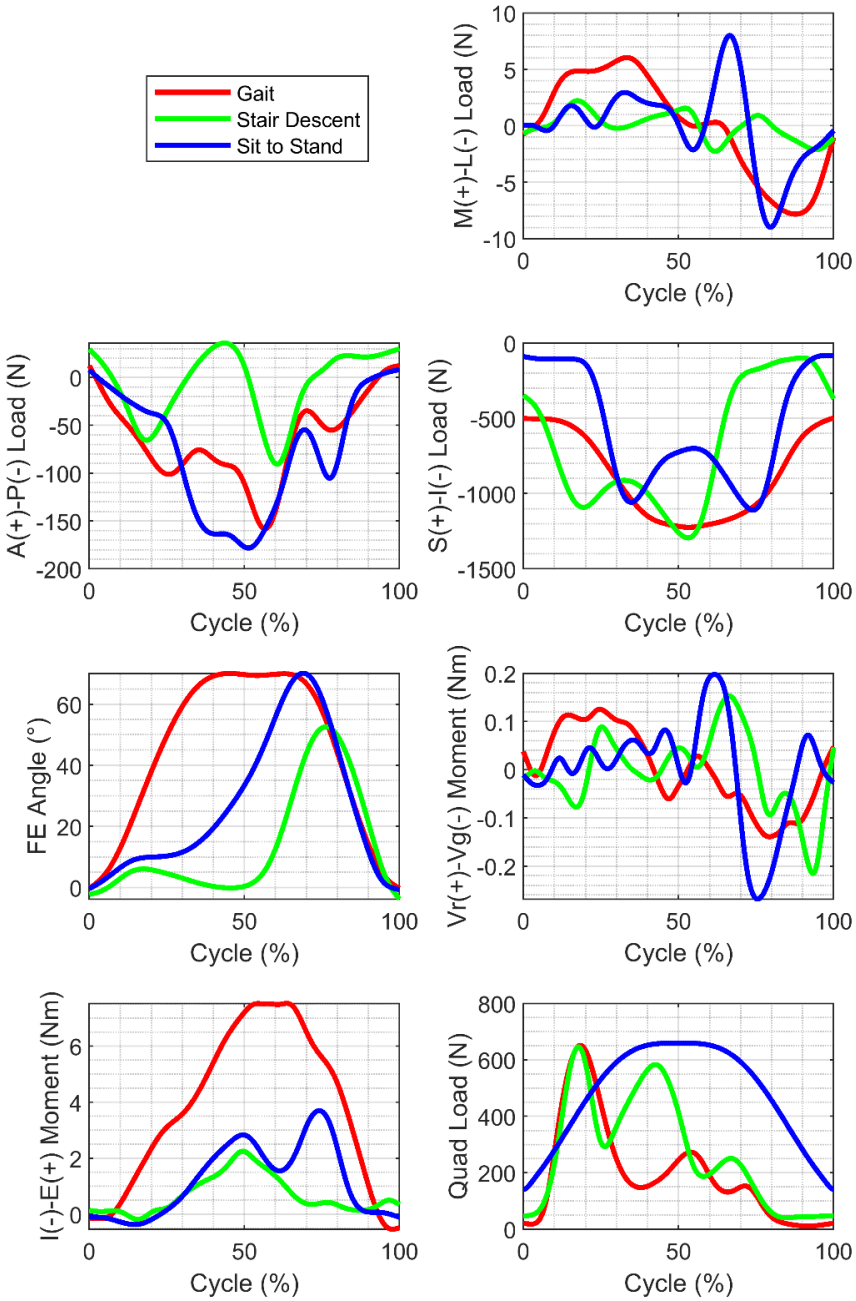

Figure 6.5: Averaged profiles of the loading that were applied to the cadaveric knees.

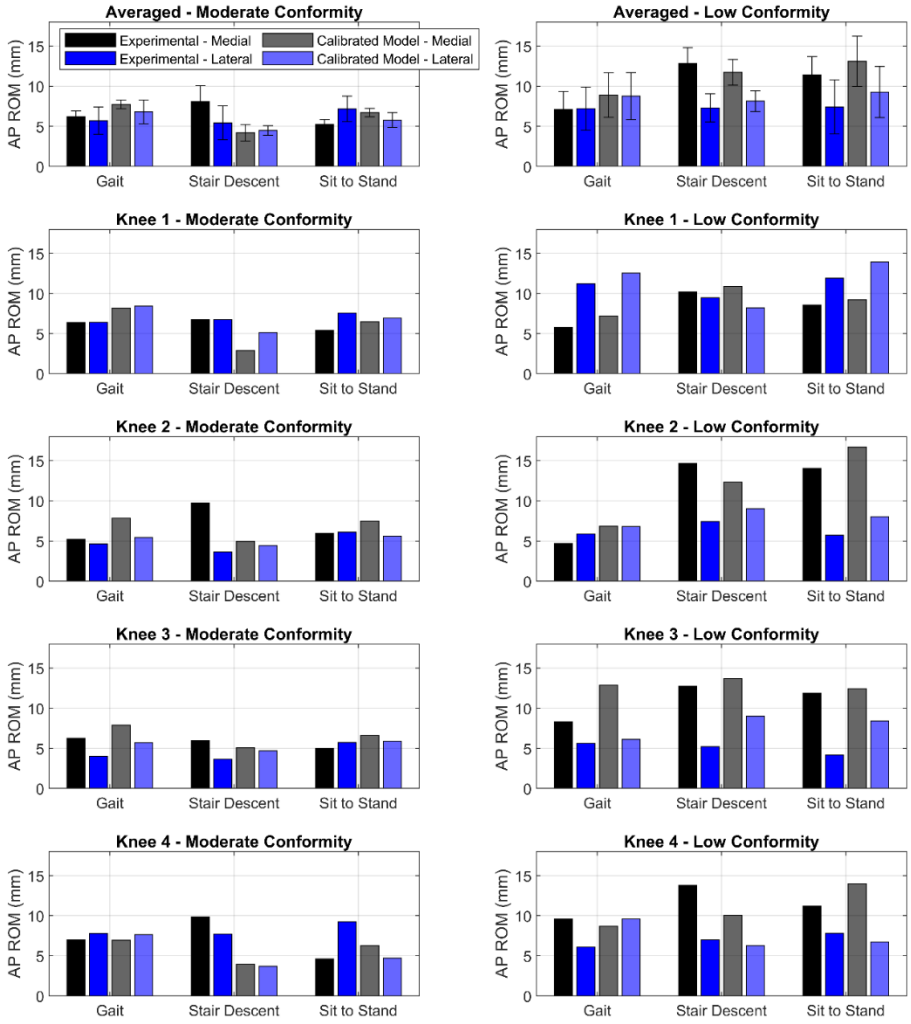

Figure 6.6: Bar chart showing mean, variation in A-P condylar translations of medial and lateral condyles of the cadaveric knees and their calibrated counterparts during gait, stair descent, and sit-to-stand.

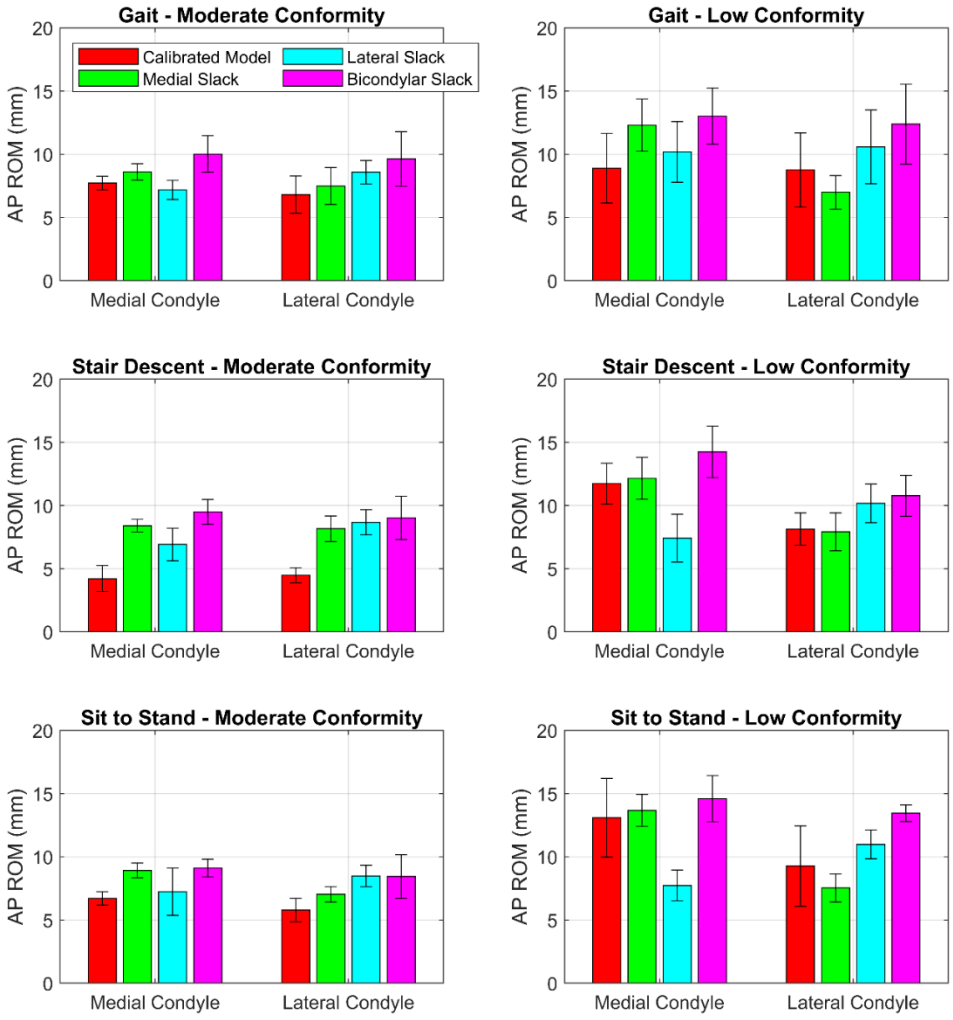

Figure 6.7: Changes in AP condylar translation for each of the ligament conditions.

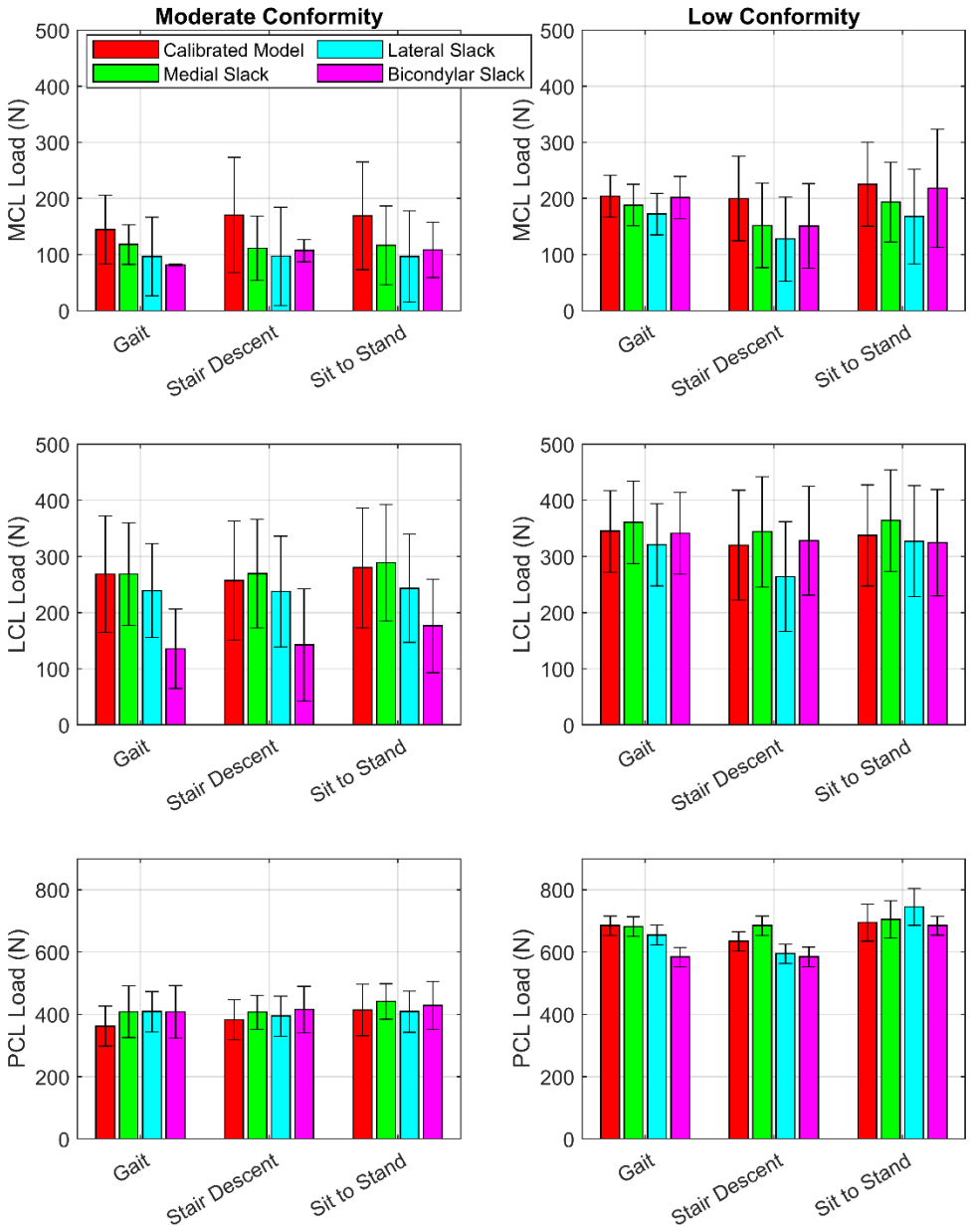

Figure 6.8: Ligament recruitment pattern during ADLs

Table 6.1: RMS error (VV laxity) for ligament calibration.

Knee Id	RMSE (°)			
	0° Flexion	30° Flexion	60° Flexion	Mean
Knee 1	0.52	1.01	0.67	0.73
Knee 2	0.82	0.49	0.89	0.73
Knee 3	0.36	0.21	0.11	0.23
Knee 4	0.83	1.35	1.60	1.26

Table 6.2: Implant alignment changes to create alternate ligament responses for each specimen. The alignment conditions were used in both the implants (Vg = Valgus, Vr = Varus, ER = External Rotation, IR = Internal Rotation).

	Knee 1	Knee 2	Knee 3	Knee 4
Medial slack	Vg & ER: 3.0°	Vg & ER: 3.0°	Vg & ER: 2.0°	Vg & ER: 2.5°
Lateral slack	Vr & IR: 2.5°	Vr & IR: 3.0°	Vr & IR: 4.0°	Vr & IR: 3.0°
Bicondylar slack	Ant & Sup: 2.0 mm	Ant & Sup: 2.0 mm	Ant & Sup: 3 mm	Ant & Sup: 1.5mm

CHAPTER 7. SUMMARY & FUTURE DIRECTIONS

7.1 Summary

This dissertation addressed four aspects of modeling specimen-specific soft tissue structures contributing to more extensive knowledge in the context of joint replacement surgery. **Chapter 3** developed specimen-specific finite element models that replicate the torque-rotational response of the implanted hip capsule. Ten cadaveric hips were characterized for internal-external laxity response at 0°, 30°, 60°, and 90° flexion, in addition to anterior and posterior dislocation resistance. Specimen-specific bone and implant geometries were used to create finite element models and capsule properties (stiffness and pre-strain) of the models were calibrated to minimize the root sum of the squared differences between model predictions and experimental torques and validated using anterior and posterior dislocation loading. The averaged calibration root mean square error (RMSE) across ten specimens was 1.02 ± 0.21 Nm (averaged range of motion: 97.2 ± 17.2°), while the validation error was 0.78 ± 0.33 Nm and 1.10 ± 0.48 Nm during the anterior and posterior dislocation, respectively. The improved accuracy of specimen-specific models was quantified by applying calibration averaged material property to the specimen-specific geometries and higher RMSE of 2.39 ± 0.68 Nm when evaluated for I-E laxity response. Ligament recruitment patterns were evaluated through the flexion range

at 5Nm of internal-external torques and were consistent with previous studies. The specimen-specific models demonstrated the importance of the hip capsule in hip stability and have relevance in surgical planning and evaluating new implant designs.

Chapter 4 addressed the main limitation of the study discussed in chapter 3. This involved calibrating the capsule's mechanical properties to match patient-specific laxities, which can require several days using traditional optimization techniques. It developed a framework for generating instantaneous subject-specific finite element models using the implanted hip capsules' statistical shape function model. The study utilized a validated FE model of the implanted hip capsule and performed probabilistic analysis to generate a dataset of 500 independent trials relating 16 capsule geometry and ligament property parameters to 40 laxity metrics. Multivariate regression models were trained using this dataset (90% data) to predict ligament parameters based on laxity metrics and attachment site information. The models were validated using the left-out 10% data and the lowest validation RMSE was 1.8° with RMSEs ranging between 1.8° and 2.3° depending on the type of laxity metrics used to train the models. The models were tested using experimental data from cadaveric specimens that had undergone a total hip replacement, and the resulting test RMSE of 4.5°. In addition, models trained only on Internal-External (IE) and adduction-abduction (Ad-Ab) laxity at 0° and 90° flexion were able to achieve high accuracy implying the minimal test data required to build subject-specific models. In addition, the approach was able to reduce the model generation from days to milliseconds. The results demonstrate the potential of regression-based training to generate instant subject-specific FE models and have implications for integrating subject-specific capsule

models into the surgical planning and decision-making workflow for improved outcomes in total hip arthroplasty.

Chapter 5 developed a computation model of commercially available wear simulator that was retrofitted with custom fixturing to evaluate whole-knee TKA mechanics with varying patella heights during a simulated deep knee bend. The model was verified for kinematic and kinetic predictions against experimental measurements. Strong agreement was observed between the experiment and model predictions with root mean square errors (RMSE) for P-F kinematics ranging from 0.8° to 3.3° and 0.7 mm to 1.4 mm. RMSE for P-F forces ranged from 7.4 N to 53.6 N. The verified model was used in the subsequent study.

Chapter 6 addressed the questions: (1). how soft tissue balance in the knee affects stability during activities of daily living and (2). if implant congruency significantly contributes to stability. Specimen-specific finite element models of four knees implanted with cruciate-retaining/cruciate sacrificing moderate conformity (MC) & low conformity (LC) implants were calibrated for ligament representation based on comprehensive experimental laxity data. Root means square error between the model and experiments for Varus/Valgus (VV) and Anterior/Posterior (AP) laxity for both knees was 0.73° and 2.8mm**,** respectively. Different levels of imbalance (medial, lateral, and bicondylar) were then achieved by virtually realigning the femoral component. The models underwent loading corresponding to activities of daily living (ADLs: gait, stair descent, and stand-sit-stand) derived from fluoroscopy-based kinematics of subjects with the same MC implant. The AP Range of motion (AP-ROM) of the low point of femoral condyles was measured to evaluate stability and compared across different levels of balancing and against

experimentally measured cadaveric test data. The RMSE errors in AP-ROM were 2.8° and 2.0° for MC and LC implants when averaged across activities. Activity-wise, stair descent showed the highest AP-ROM for both implants, while imbalance induced higher AP-ROM depending on the medial or lateral direction, with bicondylar slack condition showing the highest AP-ROM. LC implant showed higher AP-ROM than the MC implant, substantiated by higher ligament loads for the LC implant across ADLs. In conclusion, design conformity has a larger influence on ADL stability than soft tissue balancing. The results demonstrated implications for implant design, soft tissue balancing, and future testing protocols.

7.2 Future directions

Two potential areas for directing the current work are identified, and the possible research outcomes, and their clinical significance are discussed.

7.2.1 Using specimen-specific hip models to evaluate implant and surgical conditions.

The subject-specific hip capsule models developed in this dissertation have the potential to significantly contribute to the field of joint function and stability evaluation. With their comprehensive representation of variability, these models not only capture individualized characteristics but also have the potential to represent a broader range of the population. The practical implications of these subject-specific models are particularly promising, especially when combined with the expedited calibration approach. The availability of such models in clinical settings could revolutionize and help improve patient outcomes. One area where these models could be instrumental is in assessing the efficacy

of new implant types. For instance, they could evaluate the performance differences between single-mobility and dual-mobility implants to understand how the capsule stability contribution changes. Furthermore, these subject-specific models could facilitate the evaluation of implant dimension changes, such as variations in head diameter and offsets. Researchers and clinicians can assess how these modifications may impact joint function and stability by incorporating different dimensions into the models. This potential enables them to make informed decisions when selecting the most suitable implant for a given patient when aided with subject-specific models intraoperatively. Several other possible applications include implant positioning and capsule management, including incision and repair techniques.

7.2.2 Develop expedited calibration protocol for developing patient-specific knee models.

Another potential area for future work is in expediting patient-specific ligament models. Unlike the hip with limited DOFs, the knee, with its coupled, complex DOFs, makes them highly challenging to calibrate laxity response with reasonable accuracy promptly to use in a clinical setting. With the emergence of machine learning algorithms in recent years, two studies have explored the possibility of expediting the calibration process. Razu et al. employed a Bayesian calibration methodology to predict unknown ligament properties along with uncertainty bounds, using tibiofemoral kinematics and ACL force measurements from cadaver knees with different degrees of laxity (Razu et al., 2023). Their calibrated predictor of tibiofemoral kinematics and ACL force, developed through this Bayesian approach, demonstrated improved accuracy compared to a standard

optimization technique, with unique ligament slack lengths identified for each knee model. However, their scope was limited to ACL properties and resulting kinematics. Bartsoen et al. used a similar methodology to estimate the ligament material properties and attachment sites in a non-linear musculoskeletal knee model using kinematic data from a knee rig experiment in a broader set of DOFs. However, their study identified additional challenges associated with a small range of representative ligament properties for the patient population, emphasizing the need for patient-specific uncertainty ranges or alternative methods to enhance accuracy in clinical applications. Future work extending the current dissertation could explore building a sequential and step-by-step statistical approach that will understand ligament structure-function relationships with population variability, attempt to isolate individual DOFs and build an expedited calibration approach strategically.

BIBLIOGRAPHY

Abrams, G., Hart, M., Takami, K., Bayne, C., Kelly, B., Espinoza Orías, A., & Nho, S. (2015). Biomechanical Evaluation of Capsulotomy, Capsulectomy, and Capsular Repair on Hip Rotation. Arthroscopy: The Journal of Arthroscopic & Related Surgery, 31(8), 1511-1517.

Aguirre-Pastor, A., Ortolá, D. J., Lizaur-Utrilla, A., Rosa, M. A., and Lopez-Prats, F. A., 2020, "Is Pseudo-Patella Baja Really a Serious Complication of Total Knee Arthroplasty?," J. Arthroplasty, 35(2), pp. 557–562.

Alesi, D., Marcheggiani Muccioli, G. M., Roberti di Sarsina, T., Bontempi, M., Pizza, N., Zinno, R., ... & Bragonzoni, L. (2021). In vivo femorotibial kinematics of medial-stabilized total knee arthroplasty correlates to post-operative clinical outcomes. Knee Surgery, Sports Traumatology, Arthroscopy, 29, 491-497.

Ali, A. A., Harris, M. D., Shalhoub, S., Maletsky, L. P., Rullkoetter, P. J., & Shelburne, K. B. (2017). Combined measurement and modeling of specimen-specific knee mechanics for healthy and ACL-deficient conditions. Journal of biomechanics, 57, 117-124.

Ali, A. A., Shalhoub, S. S., Cyr, A. J., Fitzpatrick, C. K., Maletsky, L. P., Rullkoetter, P. J., & Shelburne, K. B. (2016). Validation of predicted patellofemoral mechanics in a finite element model of the healthy and cruciate-deficient knee. Journal of biomechanics, 49(2), 302-309.

Amis, A. A., & Dawkins, G. P. (1991). Functional anatomy of the anterior cruciate ligament. Fibre bundle actions related to ligament replacements and injuries. The Journal of Bone & Joint Surgery British Volume, 73(2), 260-267.

Anantha Krishnan, A., Myers, C. A., Scinto, M., Marshall, B. N., & Clary, C. W. (2023). Specimen-specific finite element representations of implanted hip capsules. Computer Methods in Biomechanics and Biomedical Engineering, 1-14.

Anijs, T., Eemers, S., Minoda, Y., Wolfson, D., Verdonschot, N., and Janssen, D., 2022, "Computational Tibial Bone Remodeling over a Population after Total Knee Arthroplasty: A Comparative Study," J. Biomed. Mater. Res. - Part B Appl. Biomater., 110(4), pp. 776–786.

Argenson, J., Scuderi, G., Komistek, R., Scott, W., Kelly, M., & Aubaniac, J. (2005). In vivo kinematic evaluation and design considerations related to high flexion in total knee arthroplasty. Journal of Biomechanics, 38(2), 277-284.

Aunan, E., Kibsgård, T. J., Diep, L. M., & Röhrl, S. M. (2015). Intraoperative ligament laxity influences functional outcome 1 year after total knee arthroplasty. Knee Surgery, Sports Traumatology, Arthroscopy, 23, 1684-1692.

Australian Orthopaedic Association National Joint Replacement Registry (AOANJRR)., 2018, "Hip, Knee & Shoulder Arthroplasty: 2018 Annual Report. Adelaide: AOA, 2018."

Babazadeh, S. (2009). The relevance of ligament balancing in total knee arthroplasty: how important is it? A systematic review of the literature. Orthopedic Reviews, 1(1), 26.

Badarudeen, S., Shu, A., Ong, K., Baykal, D., Lau, E., & Malkani, A. (2017). Complications After Revision Total Hip Arthroplasty in the Medicare Population. The Journal of Arthroplasty, 32(6), 1954-1958. doi: 10.1016/j.arth.2017.01.037

Bah, M. T., Nair, P. B., Taylor, M., & Browne, M. (2011). Efficient computational method for assessing the effects of implant positioning in cementless total hip replacements. Journal of biomechanics, 44(7), 1417-1422.

Baldwin, M. A., Laz, P. J., Stowe, J. Q., & Rullkoetter, P. J. (2009). Efficient probabilistic representation of tibiofemoral soft tissue constraint. Computer methods in biomechanics and biomedical engineering, 12(6), 651–659.

Baldwin, M. A., Clary, C. W., Fitzpatrick, C. K., Deacy, J. S., Maletsky, L. P., & Rullkoetter, P. J. (2012). Dynamic finite element knee simulation for evaluation of knee replacement mechanics. Journal of biomechanics, 45(3), 474-483.

Banks, S., Markovich, G., & Hodge, W. (1997). In vivo kinematics of cruciate-retaining and -substituting knee arthroplasties. The Journal of Arthroplasty, 12(3), 297-304

Barrack, R. (2003). Dislocation After Total Hip Arthroplasty: Implant Design and Orientation. Journal Of the American Academy of Orthopaedic Surgeons, 11(2), 89-99.

Batailler, C., Fary, C., Verdier, R., Aslanian, T., Caton, J., & Lustig, S. (2017). The evolution of outcomes and indications for the dual-mobility cup: a systematic review. International orthopaedics, 41, 645-659.

Bates, N. A., Nesbitt, R. J., Shearn, J. T., Myer, G. D., and Hewett, T. E., 2015, "A Novel Methodology for the Simulation of Athletic Tasks on Cadaveric Knee Joints with Respect to In Vivo Kinematics," Ann. Biomed. Eng., 43(10), pp. 2456–2466.

Bedi, A., Galano, G., Walsh, C., & Kelly, B. T. (2011). Capsular management during hip arthroscopy: from femoroacetabular impingement to instability. Arthroscopy: The Journal of Arthroscopic & Related Surgery, 27(12), 1720-1731.

Behrend, H., Graulich, T., Gerlach, R., Spross, C., and Ladurner, A., 2019, "Blackburne–Peel Ratio Predicts Patients' Outcomes after Total Knee Arthroplasty," Knee Surgery, Sport. Traumatol. Arthrosc., 27(5), pp. 1562–1569.

Beidokhti, H. N., Janssen, D., van de Groes, S., Hazrati, J., Van den Boogaard, T., & Verdonschot, N. (2017). The influence of ligament modelling strategies on the predictive capability of finite element models of the human knee joint. Journal of biomechanics, 65, 1-11.

Benos, L., Stanev, D., Spyrou, L., Moustakas, K., & Tsaopoulos, D. E. (2020). A review on finite element modeling and simulation of the anterior cruciate ligament reconstruction. Frontiers in Bioengineering and Biotechnology, 8, 967.

Bergmann, G., Bender, A., Graichen, F., Dymke, J., Rohlmann, A., & Trepczynski, A. et al. (2014). Standardized Loads Acting in Knee Implants. Plos ONE, 9(1), e86035.

Bermel, E. A., Thakral, S., Claeson, A. A., Ellingson, A. M., & Barocas, V. H. (2020). Asymmetric in-plane shear behavior of isolated cadaveric lumbar facet capsular ligaments: Implications for subject specific biomechanical models. Journal of biomechanics, 105, 109814.

Bischoff, J. E., Dai, Y., Goodlett, C., Davis, B., & Bandi, M. (2014). Incorporating population-level variability in orthopedic biomechanical analysis: a review. Journal of biomechanical engineering, 136(2), 021004.

Bischoff, J. E., Siggelkow, E., Sieber, D., Kersh, M., Ploeg, H., & Münchinger, M. (2008, March). Advanced material modeling in a virtual biomechanical knee. In Abaqus Users' Conference (pp. 1-15).

Blankevoort, L., & Huiskes, R. (1991). Ligament-bone interaction in a three-dimensional model of the knee. Journal of biomechanical engineering, 113(3), 263–269.

Blankevoort, L., & Huiskes, R. (1996). Validation of a three-dimensional model of the knee. Journal of biomechanics, 29(7), 955-961.

Bowman Jr, K. F., & Sekiya, J. K. (2010). Anatomy and biomechanics of the posterior cruciate ligament, medial and lateral sides of the knee. Sports medicine and arthroscopy review, 18(4), 222-229.

Browne, C., Hermida, J. C., Bergula, A., Colwell, C. W., and D'Lima, D. D., 2005, "Patellofemoral Forces after Total Knee Arthroplasty: Effect of Extensor Moment Arm," Knee, 12(2), pp. 81–88.

Brynskog, E., Iraeus, J., Reed, M. P., & Davidsson, J. (2021). Predicting pelvis geometry using a morphometric model with overall anthropometric variables. Journal of biomechanics, 126, 110633.

Bugelli, G., Ascione, F., Cazzella, N., Franceschetti, E., Franceschi, F., Dell'Osso, G., Svantesson, E., Samuelsson, K., and Giannotti, S., 2018, "Pseudo-Patella Baja: A Minor yet Frequent Complication of Total Knee Arthroplasty," Knee Surgery, Sport. Traumatol. Arthrosc., 26(6), pp. 1831–1837.

Bunn, A., Colwell Jr, C. W., & D'Lima, D. D. (2014). Effect of head diameter on passive and active dynamic hip dislocation. Journal of Orthopaedic Research, 32(11), 1525-1531.

Burkhart, T. A., Baha, P., Blokker, A., Petrov, I., Holdsworth, D. W., Drangova, M., ... & Degen, R. M. (2020). Hip capsular strain varies between ligaments dependent on both hip position-and applied rotational force. Knee Surgery, Sports Traumatology, Arthroscopy, 28(10), 3393-3399.

Charles, M. N., Bourne, R. B., Davey, J. R., Greenwald, A. S., Morrey, B. F., & Rorabeck, C. H. (2005). Soft-tissue balancing of the hip: the role of femoral offset restoration. Instructional course lectures, 54, 131-141.

Cho, J. M., Suh, J. S., Na, J. B., Cho, J. H., Kim, Y., Yoo, W. K., ... & Chung, I. H. (1999). Variations in meniscofemoral ligaments at anatomical study and MR imaging. Skeletal radiology, 28, 189-195.

Chonko, D. J., Lombardi, A. V. J., and Berend, K. R., 2004, "Patella Baja and Total Knee Arthroplasty (TKA): Etiology, Diagnosis, and Management.," Surg. Technol. Int., 12, pp. 231–238.

Clary, C. W., Fitzpatrick, C. K., Maletsky, L. P., & Rullkoetter, P. J. (2013). The influence of total knee arthroplasty geometry on mid-flexion stability: an experimental and finite element study. Journal of biomechanics, 46(7), 1351-1357.

Colombi, A., Schena, D., & Castelli, C. C. (2019). Total hip arthroplasty planning. EFORT Open Reviews, 4(11), 626.

Courtney, P. M., & Lee, G. C. (2017). Early outcomes of kinematic alignment in primary total knee arthroplasty: a meta-analysis of the literature. The Journal of arthroplasty, 32(6), 2028-2032.

D'Ambrosi, R., Ursino, N., Messina, C., Della Rocca, F., & Hirschmann, M. T. (2021). The role of the iliofemoral ligament as a stabilizer of the hip joint. EFORT Open Reviews, 6(7), 545-555.

D'Lima, D. D., Townsend, C. P., Arms, S. W., Morris, B. A., and Colwell, C. W., 2005, "An Implantable Telemetry Device to Measure Intra-Articular Tibial Forces," J. Biomech., 38(2), pp. 299–304.

Daniilidis, K., Skwara, A., Vieth, V., Fuchs-Winkelmann, S., Heindel, W., Stückmann, V., & Tibesku, C. O. (2012). Highly conforming polyethylene inlays reduce the in vivo variability of knee joint kinematics after total knee arthroplasty. The Knee, 19(4), 260-265.

DesJardins, J., Walker, P., Haider, H., & Perry, J. (2000). The use of a force-controlled dynamic knee simulator to quantify the mechanical performance of total knee replacement designs during functional activity. Journal Of Biomechanics, 33(10), 1231-1242

Donaldson, F. E., Nyman Jr, E., & Coburn, J. C. (2015). Prediction of contact mechanics in metal-on-metal Total Hip Replacement for parametrically comprehensive designs and loads. Journal of Biomechanics, 48(10), 1828-1835.

Dreyer, M. J., Trepczynski, A., Hosseini Nasab, S. H., Kutzner, I., Schütz, P., Weisse, B., Dymke, J., Postolka, B., Moewis, P., Bergmann, G., Duda, G. N., Taylor, W. R., Damm, P., and Smith, C. R., 2022, "European Society of Biomechanics S.M. Perren Award 2022: Standardized Tibio-Femoral Implant Loads and Kinematics," J. Biomech., 141(June).

Drury, N. J., Ellis, B. J., Weiss, J. A., McMahon, P. J., & Debski, R. E. (2011). Finding consistent strain distributions in the glenohumeral capsule between two subjects: implications for development of physical examinations. Journal of biomechanics, 44(4), 607-613.

Elkins, J. M., Stroud, N. J., Rudert, M. J., Tochigi, Y., Pedersen, D. R., Ellis, B. J., ... & Brown, T. D. (2011). The capsule's contribution to total hip construct stability–a finite element analysis. Journal of Orthopaedic Research, 29(11), 1642-1648.

Emara, A. K., Samuel, L. T., Acuña, A. J., Kuo, A., Khlopas, A., & Kamath, A. F. (2021). Robotic-arm assisted versus manual total hip arthroplasty: Systematic review and meta-analysis of radiographic accuracy. The International Journal of Medical Robotics and Computer Assisted Surgery, 17(6), e2332.

Emodi, G. J., Callaghan, J. J., Pedersen, D. R., & Brown, T. D. (1999). Posterior cruciate ligament function following total knee arthroplasty: the effect of joint line elevation. The Iowa orthopaedic journal, 19, 82–92.

Erdemir, A., Guess, T. M., Halloran, J., Tadepalli, S. C., & Morrison, T. M. (2012). Considerations for reporting finite element analysis studies in biomechanics. Journal of biomechanics, 45(4), 625-633.

Ewing, J. A., Kaufman, M. K., Hutter, E. E., Granger, J. F., Beal, M. D., Piazza, S. J., & Siston, R. A. (2016). Estimating patient-specific soft-tissue properties in a TKA knee. Journal of Orthopaedic Research, 34(3), 435-443.

Ezquerro, F., Vacas, F. G., Postigo, S., Prado, M., & Simón, A. (2011). Calibration of the finite element model of a lumbar functional spinal unit using an optimization technique based on differential evolution. Medical engineering & physics, 33(1), 89-95.

Fitzpatrick, C. K., Baldwin, M. A., Rullkoetter, P. J., & Laz, P. J. (2011). Combined probabilistic and principal component analysis approach for multivariate sensitivity evaluation and application to implanted patellofemoral mechanics. Journal of biomechanics, 44(1), 13-21.

Fitzpatrick, C. K., Hemelaar, P., & Taylor, M. (2014). Computationally efficient prediction of bone–implant interface micromotion of a cementless tibial tray during gait. Journal of biomechanics, 47(7), 1718-1726.

Fitzpatrick, C. K., Maag, C., Clary, C. W., Metcalfe, A., Langhorn, J., and Rullkoetter, P. J., 2016, “Validation of a New Computational 6-DOF Knee Simulator during Dynamic Activities,” J. Biomech., 49(14), pp. 3177–3184.

Fitzpatrick, C., Baldwin, M., & Rullkoetter, P. (2010). Computationally Efficient Finite Element Evaluation of Natural Patellofemoral Mechanics. Journal Of Biomechanical Engineering, 132(12).

Fitzpatrick, C., Baldwin, M., Clary, C., Maletsky, L., and Rullkoetter, P., 2014, "Evaluating Knee Replacement Mechanics during ADL with PID-Controlled Dynamic Finite Element Analysis," Comput. Methods Biomech. Biomed. Engin., 17(4).

Flandry, F., & Hommel, G. (2011). Normal anatomy and biomechanics of the knee. Sports medicine and arthroscopy review, 19(2), 82-92.

Flato, R., Passanante, G. J., Skalski, M. R., Patel, D. B., White, E. A., & Matcuk, G. R. (2017). The iliotibial tract: imaging, anatomy, injuries, and other pathology. Skeletal radiology, 46, 605-622.

Flores, C., Celik, H., Hoenecke, H., & D'Lima, D. D. (2023). Subject-specific computational modeling of acromioclavicular and coracoclavicular ligaments. Journal of Shoulder and Elbow Surgery, 32(3), 526-532.

Fontalis, A., Kayani, B., Thompson, J. W., Plastow, R., & Haddad, F. S. (2022). Robotic total hip arthroplasty: Past, present and future. Orthopaedics and Trauma, 36(1), 6-13.

Frank, C. B. (2004). Ligament structure, physiology and function. Journal of Musculoskeletal and Neuronal Interactions, 4(2), 199.

Fu, F. H., Harner, C. D., Johnson, D. L., Miller, M. D., & Woo, S. L. Y. (1993). Biomechanics of knee ligaments: basic concepts and clinical application. JBJS, 75(11), 1716-1727.

Gaillard, R., Bankhead, C., Budhiparama, N., Batailler, C., Servien, E., and Lustig, S., 2019, "Influence of Patella Height on Total Knee Arthroplasty: Outcomes and Survival," J. Arthroplasty, 34(3), pp. 469–477.

Galbusera, F., Freutel, M., Dürselen, L., D'Aiuto, M., Croce, D., Villa, T., ... & Innocenti, B. (2014). Material models and properties in the finite element analysis of knee ligaments: a literature review. Frontiers in bioengineering and biotechnology, 2, 54.

Gardiner, J. C., & Weiss, J. A. (2003). Subject-specific finite element analysis of the human medial collateral ligament during valgus knee loading. Journal of orthopaedic research, 21(6), 1098-1106.

Gibbons, K. D., Clary, C. W., Rullkoetter, P. J., & Fitzpatrick, C. K. (2019). Development of a statistical shape-function model of the implanted knee for real-time prediction of joint mechanics. Journal of Biomechanics, 88, 55-63.

Goldblatt, J. P., & Richmond, J. C. (2003). Anatomy and biomechanics of the knee. Operative techniques in sports medicine, 11(3), 172-186.

Grantham, W. J., Aman, Z. S., Brady, A. W., Rosenberg, S. I., Lee Turnbull, T., Storaci, H. W., Dornan, G. J., and LaPrade, R. F., 2020, "Medial Patellotibial Ligament Reconstruction Improves Patella Tracking When Combined With Medial Patellofemoral Reconstruction: An In Vitro Kinematic Study," Arthrosc. - J. Arthrosc. Relat. Surg., 36(9), pp. 2501–2509.

Grieco, T., Sharma, A., Komistek, R., & Cates, H. (2016). Single Versus Multiple-Radii Cruciate-Retaining Total Knee Arthroplasty: An In Vivo Mobile Fluoroscopy Study. The Journal of Arthroplasty, 31(3), 694-701.

Griffin, F., Insall, J., & Scuderi, G. (2000). Accuracy of soft tissue balancing in total knee arthroplasty. The Journal of Arthroplasty, 15(8), 970-973.

Grood, E. S., & Suntay, W. J. (1983). A joint coordinate system for the clinical description of three-dimensional motions: application to the knee. Journal of biomechanical engineering, 105(2), 136-144.

Halloran, J. P., Easley, S. K., Petrella, A. J., and Rullkoetter, P. J., 2005, "Comparison of Deformable and Elastic Foundation Finite Element Simulations for Predicting Knee Replacement Mechanics," J. Biomech. Eng., 127(5), pp. 813–818.

Halloran, J. P., Petrella, A. J., & Rullkoetter, P. J. (2005). Explicit finite element modeling of total knee replacement mechanics. Journal of biomechanics, 38(2), 323-331.

Halloran, J., Easley, S., Petrella, A., & Rullkoetter, P. (2005). Comparison of Deformable and Elastic Foundation Finite Element Simulations for Predicting Knee Replacement Mechanics. Journal Of Biomechanical Engineering, 127(5), 813-818.

Harris, M. D., Cyr, A. J., Ali, A. A., Fitzpatrick, C. K., Rullkoetter, P. J., Maletsky, L. P., & Shelburne, K. B. (2016). A combined experimental and computational approach to subject-specific analysis of knee joint laxity. Journal of biomechanical engineering, 138(8).

Hassebrock, J. D., Gulbrandsen, M. T., Asprey, W. L., Makovicka, J. L., & Chhabra, A. (2020). Knee ligament anatomy and biomechanics. Sports medicine and arthroscopy review, 28(3), 80-86.

Haynes, J. A., Hopper Jr, R. H., Ho, H., McDonald III, J. F., Parks, N. L., & Hamilton, W. G. (2022). Direct anterior approach for primary total hip arthroplasty lowers the risk of dislocation compared to the posterior approach: a single institution experience. The Journal of Arthroplasty, 37(3), 495-500.

Heckmann, N. D., Steck, T., Sporer, S. M., & Meneghini, R. M. (2021). Conforming Polyethylene Inserts in Total Knee Arthroplasty: Beyond the Posterior-Stabilized and Cruciate-Retaining Debate. JAAOS-Journal of the American Academy of Orthopaedic Surgeons, 29(22), e1097-e1104.

Heimann, T., & Meinzer, H. P. (2009). Statistical shape models for 3D medical image segmentation: a review. Medical image analysis, 13(4), 543-563.

Heinlein, B., Graichen, F., Bender, A., Rohlmann, A., & Bergmann, G. (2007). Design, calibration and pre-clinical testing of an instrumented tibial tray. Journal of biomechanics, 40, S4-S10.

Henak, C. R., Anderson, A. E., & Weiss, J. A. (2013). Subject-specific analysis of joint contact mechanics: application to the study of osteoarthritis and surgical planning. Journal of biomechanical engineering, 135(2), 021003.

Herrmann, S., Woernle, C., Kaehler, M., Rachholz, R., Souffrant, R., Zierath, J., Kluess, D., and Bader, R., 2012, “HiL Simulation for Testing Joint Stability after Total Knee Arthroplasty,” Multibody Syst. Dyn., 28(1–2), pp. 55–67.

Hidaka, E., Aoki, M., Izumi, T., Suzuki, D., & Fujimiya, M. (2014). Ligament strain on the iliofemoral, pubofemoral, and ischiofemoral ligaments in cadaver specimens: biomechanical measurement and anatomical observation. Clinical Anatomy, 27(7), 1068-1075.

Hollenbeck, J. F., Cain, C. M., Fattor, J. A., Rullkoetter, P. J., & Laz, P. J. (2018). Statistical shape modeling characterizes three-dimensional shape and alignment variability in the lumbar spine. Journal of biomechanics, 69, 146-155.

Hosseini Nasab, S., Smith, C., Schütz, P., Damm, P., Trepczynski, A., List, R., & Taylor, W. (2020). Length-Change Patterns of the Collateral Ligaments During Functional

Activities After Total Knee Arthroplasty. Annals Of Biomedical Engineering, 48(4), 1396-1406.

Hosseini Nasab, S., Smith, C., Schütz, P., Postolka, B., Ferguson, S., Taylor, W., & List, R. (2020). Elongation Patterns of the Posterior Cruciate Ligament after Total Knee Arthroplasty. Journal Of Clinical Medicine, 9(7), 2078.

Hume, D. R., Navacchia, A., Rullkoetter, P. J., and Shelburne, K. B., 2019, "A Lower Extremity Model for Muscle-Driven Simulation of Activity Using Explicit Finite Element Modeling," J. Biomech., 84, pp. 153–160.

Jiang, C., Liu, Z., Wang, Y., Bian, Y., Feng, B., & Weng, X. (2016). Posterior cruciate ligament retention versus posterior stabilization for total knee arthroplasty: a meta-analysis. PloS one, 11(1), e0147865.

Johnston, H., Abdelgaied, A., Pandit, H., Fisher, J., & Jennings, L. (2019). The effect of surgical alignment and soft tissue conditions on the kinematics and wear of a fixed bearing total knee replacement. Journal of the Mechanical Behavior of Biomedical Materials, 100, 103386.

Kallemeyn, N., Gandhi, A., Kode, S., Shivanna, K., Smucker, J., & Grosland, N. (2010). Validation of a C2–C7 cervical spine finite element model using specimen-specific flexibility data. Medical engineering & physics, 32(5), 482-489.

Kaplan, E. B. (1961). The fabellofibular and short lateral ligaments of the knee joint. JBJS, 43(2), 169-179.

Karunaseelan, K. J., Dandridge, O., Muirhead-Allwood, S. K., van Arkel, R. J., & Jeffers, J. R. (2021). Capsular ligaments provide a passive stabilizing force to protect the hip against edge loading. Bone & Joint Research, 10(9), 594.

Kenney, C., Dick, S., Lea, J., Liu, J., & Ebraheim, N. (2019). A systematic review of the causes of failure of Revision Total Hip Arthroplasty. Journal Of Orthopaedics, 16(5), 393-395. doi: 10.1016/j.jor.2019.04.011

Khair, M., Grzybowski, J., Kuhns, B., Wuerz, T., Shewman, E., & Nho, S. (2017). The Effect of Capsulotomy and Capsular Repair on Hip Distraction: A Cadaveric Investigation. Arthroscopy: The Journal of Arthroscopic & Related Surgery, 33(3), 559-565.

Khasian, M., Sharma, A., Fehring, T., Griffin, W., Mason, J., & Komistek, R. (2020). Kinematic Performance of Gradually Variable Radius Posterior-Stabilized Primary

TKA During Various Activities: An In Vivo Study Using Fluoroscopy. The Journal of Arthroplasty, 35(4), 1101-1108.

Kia, M., Schafer, K., Lipman, J., Cross, M., Mayman, D., Pearle, A., ... & Imhauser, C. (2016). A multibody knee model corroborates subject-specific experimental measurements of low ligament forces and kinematic coupling during passive flexion. Journal of Biomechanical Engineering, 138(5), 051010.

Kunutsor, S., Barrett, M., Beswick, A., Judge, A., Blom, A., Wylde, V., & Whitehouse, M. (2019). Risk factors for dislocation after primary total hip replacement: a systematic review and meta-analysis of 125 studies involving approximately five million hip replacements. The Lancet Rheumatology, 1(2), e111-e121. doi: 10.1016/s2665-9913(19)30045-1

LaPrade, M. D., Kennedy, M. I., Wijdicks, C. A., & LaPrade, R. F. (2015). Anatomy and biomechanics of the medial side of the knee and their surgical implications. Sports Medicine and Arthroscopy Review, 23(2), 63-70.

LaPrade, R. F., Morgan, P. M., Wentorf, F. A., Johansen, S., & Engebretsen, L. (2007). The anatomy of the posterior aspect of the knee. An anatomic study. The Journal of bone and joint surgery. American volume, 89(4), 758–764. https://doi.org/10.2106/JBJS.F.00120

Lee, T. Q., 2014, "Biomechanics of Hyperflexion and Kneeling before and after Total Knee Arthroplasty," Clin. Orthop. Surg., 6(2), pp. 117–126.

List, R., Schütz, P., Angst, M., Ellenberger, L., Dätwyler, K., & Ferguson, S. et al. (2020). Videofluoroscopic Evaluation of the Influence of a Gradually Reducing Femoral Radius on Joint Kinematics During Daily Activities in Total Knee Arthroplasty. The Journal of Arthroplasty, 35(10), 3010-3030.

List, R., Schütz, P., Angst, M., Ellenberger, L., Dätwyler, K., Ferguson, S. J., von Eisenhart-Rothe, R., and Schwaller, C., 2020, "Videofluoroscopic Evaluation of the Influence of a Gradually Reducing Femoral Radius on Joint Kinematics During Daily Activities in Total Knee Arthroplasty," J. Arthroplasty, 35(10), pp. 3010–3030.

Loitz, B. J., & Frank, C. B. (1993). Biology and mechanics of ligament and ligament healing. Exercise and Sport Sciences Reviews, 21(1), 33-64.

Luger, E., Sathasivam, S., & Walker, P. (1997). Inherent differences in the laxity and stability between the intact knee and total knee replacements. The Knee, 4(1), 7-14.

Luyckx, T., Didden, K., Vandenneucker, H., Labey, L., Innocenti, B., and Bellemans, J., 2009, "Is There a Biomechanical Explanation for Anterior Knee Pain in Patients with Patella Alta? Influence of Patellar Height on Patellofemoral Contact Force, Contact Area and Contact Pressure," J. Bone Jt. Surg. - Ser. B, 91(3), pp. 344–350.

Mahoney, O., McClung, C., dela Rosa, M., & Schmalzried, T. (2002). The effect of total knee arthroplasty design on extensor mechanism function. The Journal of Arthroplasty, 17(4), 416-421.

Malagelada, F., Tayar, R., Barke, S., Stafford, G., & Field, R. E. (2015). Anatomy of the zona orbicularis of the hip: a magnetic resonance study. Surgical and Radiologic Anatomy, 37, 11-18.

Maletsky, L. P., & Hillberry, B. M. (2005). Simulating dynamic activities using a five-axis knee simulator. J. Biomech. Eng., 127(1), 123-133.

Maletsky, L. P., and Hillberry, B. M., 2005, "Simulating Dynamic Activities Using a Five-Axis Knee Simulator," J. Biomech. Eng., 127(1), pp. 123–133.

Maratt, J. D., Gagnier, J. J., Butler, P. D., Hallstrom, B. R., Urquhart, A. G., & Roberts, K. C. (2016). No difference in dislocation seen in anterior vs posterior approach total hip arthroplasty. The Journal of arthroplasty, 31(9), 127-130.

Marchand, R., Sodhi, N., Bhowmik-Stoker, M., Scholl, L., Condrey, C., & Khlopas, A. et al. (2018). Does the Robotic Arm and Preoperative CT Planning Help with 3D Intraoperative Total Knee Arthroplasty Planning?. The Journal of Knee Surgery, 32(08), 742-749.

Martin, H. D., Khoury, A. N., Schröder, R., Johnson, E., Gómez-Hoyos, J., Campos, S., & Palmer, I. J. (2017). Contribution of the pubofemoral ligament to hip stability: a biomechanical study. Arthroscopy: The Journal of Arthroscopic & Related Surgery, 33(2), 305-313.

Martin, H. D., Savage, A., Braly, B. A., Palmer, I. J., Beall, D. P., & Kelly, B. (2008). The function of the hip capsular ligaments: a quantitative report. Arthroscopy: The Journal of Arthroscopic & Related Surgery, 24(2), 188-195.

McLawhorn, A., Christ, A., Morgenstern, R., Burge, A., Alexiades, M., & Su, E. (2020). Prospective Evaluation of the Posterior Tissue Envelope and Anterior Capsule After Anterior Total Hip Arthroplasty. The Journal of Arthroplasty, 35(3), 767-773.

Melvin, J., Karthikeyan, T., Cope, R., & Fehring, T. (2014). Early Failures in Total Hip Arthroplasty — A Changing Paradigm. The Journal of Arthroplasty, 29(6), 1285-1288. doi: 10.1016/j.arth.2013.12.024

Mercuri, J., Pepper, A., Werner, J., & Vigdorchik, J. (2019). Gap Balancing, Measured Resection, and Kinematic Alignment. JBJS Reviews, 7(3), e2-e2.

Mihalko, W. M., & Whiteside, L. A. (2004). Hip mechanics after posterior structure repair in total hip arthroplasty. Clinical Orthopaedics and Related Research®, 420, 194-198.

Mihalko, W. M., Whiteside, L. A., & Krackow, K. A. (2003). Comparison of ligament-balancing techniques during total knee arthroplasty. JBJS, 85(suppl_4), 132-135.

Mizuno, Y., Kumagai, M., Mattessich, S. M., Elias, J. J., Ramrattan, N., Cosgarea, A. J., and Chao, E. Y. S., 2001, "Q-Angle Influences Tibiofemoral and Patellofemoral Kinematics," J. Orthop. Res., 19(5), pp. 834–840.

Mjaaland, K. E., Svenningsen, S., Fenstad, A. M., Havelin, L. I., Furnes, O., & Nordsletten, L. (2017). Implant survival after minimally invasive anterior or anterolateral vs. conventional posterior or direct lateral approach: an analysis of 21,860 total hip arthroplasties from the Norwegian Arthroplasty Register (2008 to 2013). JBJS, 99(10), 840-847.

Moro-oka, T., Shiraishi, H., Iwamoto, Y., & Banks, S. (2009). Modified gap-balancing technique in total knee arthroplasty: evaluation of the post-operative coronal laxity. Knee Surgery, Sports Traumatology, Arthroscopy, 18(3), 375-380.

Myers, C. A., Fitzpatrick, C. K., Huff, D. N., Laz, P. J., & Rullkoetter, P. J. (2020). Development and calibration of a probabilistic finite element hip capsule representation. Computer Methods in Biomechanics and Biomedical Engineering, 23(11), 755-764.

Nakamura, S., Ito, H., Yoshitomi, H., Kuriyama, S., Komistek, R., & Matsuda, S. (2015). Analysis of the Flexion Gap on In Vivo Knee Kinematics Using Fluoroscopy. The Journal of Arthroplasty, 30(7), 1237-1242.

Navacchia, A., Bates, N. A., Schilaty, N. D., Krych, A. J., & Hewett, T. E. (2019). Knee abduction and internal rotation moments increase ACL force during landing through the posterior slope of the tibia. Journal of Orthopaedic Research®, 37(8), 1730-1742.

Navacchia, A., Bates, N. A., Schilaty, N. D., Krych, A. J., and Hewett, T. E., 2020, "Force During Landing Through the Posterior Slope of the Tibia," 37(8), pp. 1730–1742.

Navacchia, A., Clary, C. W., Han, X., Shelburne, K. B., Wright, A. P., and Rullkoetter, P. J., 2018, "Loading and Kinematic Profiles for Patellofemoral Durability Testing," J. Mech. Behav. Biomed. Mater., 86(June), pp. 305–313.

Navacchia, A., Hume, D. R., Rullkoetter, P. J., and Shelburne, K. B., 2019, "A Computationally Efficient Strategy to Estimate Muscle Forces in a Finite Element Musculoskeletal Model of the Lower Limb," J. Biomech., 84, pp. 94–102.

Navacchia, A., Rullkoetter, P. J., Schütz, P., List, R. B., Fitzpatrick, C. K., and Shelburne, K. B., 2016, "Subject-Specific Modeling of Muscle Force and Knee Contact in Total Knee Arthroplasty," J. Orthop. Res., 34(9), pp. 1576–1587.

Ng, K. G., Jeffers, J. R., & Beaulé, P. E. (2019). Hip joint capsular anatomy, mechanics, and surgical management. The Journal of Bone and Joint Surgery. American Volume, 101(23), 2141.

Noble, L. D., Colbrunn, R. W., Lee, D. G., Van Den Bogert, A. J., and Davis, B. L., 2010, "Design and Validation of a General Purpose Robotic Testing System for Musculoskeletal Applications," J. Biomech. Eng., 132(2).

Nyland, J., Lachman, N., Kocabey, Y., Brosky, J., Altun, R., & Caborn, D. (2005). Anatomy, function, and rehabilitation of the popliteus musculotendinous complex. Journal of Orthopaedic & Sports Physical Therapy, 35(3), 165-179.

Owens, J. S., Jimenez, A. E., Shapira, J., Saks, B. R., Glein, R. M., Maldonado, D. R., ... & Domb, B. G. (2021). Capsular repair may improve outcomes in patients undergoing hip arthroscopy for femoroacetabular impingement: a systematic review of comparative outcome studies. Arthroscopy: The Journal of Arthroscopic & Related Surgery, 37(9), 2975-2990.

P.M., B., A., K., M., C., C., C., C.U., G., S.F., H., B., W., D.E., O., and J.E., D., 2017, "Unusually High Rate of Early Failure of Tibial Component in ATTUNE Total

Knee Arthroplasty System at Implant-Cement Interface," J. Knee Surg., 30(5), pp. 435–439.

Padgett, D., & Warashina, H. (2004). The Unstable Total Hip Replacement. Clinical Orthopaedics and Related Research, 420, 72-79.

Papaioannou, G., Nianios, G., Mitrogiannis, C., Fyhrie, D., Tashman, S., & Yang, K. H. (2008). Patient-specific knee joint finite element model validation with high-accuracy kinematics from biplane dynamic Roentgen stereogrammetric analysis. Journal of Biomechanics, 41(12), 2633-2638.

Pedersen, D. R., Callaghan, J. J., & Brown, T. D. (2005). Activity-dependence of the "safe zone" for impingement versus dislocation avoidance. Medical engineering & physics, 27(4), 323-328.

Pedneault, C., Tanzer, D., Nooh, A., Smith, K., & Tanzer, M. (2020). Capsular closure outweighs head size in preventing dislocation following revision total hip arthroplasty. HIP International, 30(2), 141-146.

Pellicci, P., Bostrom, M., & Poss, R. (1998). Posterior Approach to Total Hip Replacement Using Enhanced Posterior Soft Tissue Repair. Clinical Orthopaedics and Related Research, 355, 224-228.

Piedade, S. R., Pinaroli, A., Servien, E., and Neyret, P., 2009, "Revision after Early Aseptic Failures in Primary Total Knee Arthroplasty," Knee Surgery, Sport. Traumatol. Arthrosc., 17(3), pp. 248–253.

Pillet, H., Bergamini, E., Rochcongar, G., Camomilla, V., Thoreux, P., Rouch, P., ... & Skalli, W. (2016). Femur, tibia and fibula bone templates to estimate subject-specific knee ligament attachment site locations. Journal of Biomechanics, 49(14), 3523-3528.

Pitta, M., Esposito, C., Li, Z., Lee, Y., Wright, T., & Padgett, D. (2018). Failure After Modern Total Knee Arthroplasty: A Prospective Study of 18,065 Knees. The Journal of Arthroplasty, 33(2), 407-414.

Pizza, N., Di Paolo, S., Zinno, R., Marcheggiani Muccioli, G. M., Agostinone, P., Alesi, D., ... & Bragonzoni, L. (2021). Over-constrained kinematic of the medial compartment leads to lower clinical outcomes after total knee arthroplasty. Knee Surgery, Sports Traumatology, Arthroscopy, 1-7.

Razu, S. S., and Guess, T. M., 2018, “Electromyography-Driven Forward Dynamics Simulation to Estimate in Vivo Joint Contact Forces during Normal, Smooth, and Bouncy Gaits,” J. Biomech. Eng., 140(7), pp. 1–8.

Razu, S. S., Jahandar, H., Zhu, A., Berube, E. E., Manzi, J. E., Pearle, A. D., ... & Imhauser, C. W. (2023). Bayesian Calibration of Computational Knee Models to Estimate Subject-Specific Ligament Properties, Tibiofemoral Kinematics, and Anterior Cruciate Ligament Force With Uncertainty Quantification. Journal of Biomechanical Engineering, 145(7), 071003.

Reyneke, C. J. F., Lüthi, M., Burdin, V., Douglas, T. S., Vetter, T., & Mutsvangwa, T. E. (2018). Review of 2-D/3-D reconstruction using statistical shape and intensity models and X-ray image synthesis: Toward a unified framework. IEEE reviews in biomedical engineering, 12, 269-286.

Riddick, A., Smith, A., & Thomas, D. P. (2014). Accuracy of preoperative templating in total hip arthroplasty. Journal of Orthopaedic Surgery, 22(2), 173-176.

Rivière, C., Harman, C., Parsons, T., Villet, L., Cobb, J., & Maillot, C. (2019). Kinematic alignment versus conventional techniques for total hip arthroplasty: a retrospective case control study. Orthopaedics & Traumatology: Surgery & Research, 105(5), 895-905.

Rodriguez-Merchan, E. C. (2011). Instability following total knee arthroplasty. HSS Journal, 7(3), 273-278.

Romero, J., Stähelin, T., Binkert, C., Pfirrmann, C., Hodler, J., & Kessler, O. (2007). The Clinical Consequences of Flexion Gap Asymmetry in Total Knee Arthroplasty. The Journal of Arthroplasty, 22(2), 235-240.

Ryan, S. P., Cochrane, N. H., Jiranek, W. A., Seyler, T. M., Wellman, S. S., & Bolognesi, M. P. (2023). Evaluation of anterior translation in total knee arthroplasty utilizing stress radiographs. Journal of Orthopaedic Surgery and Research, 18(1), 1-5.

Salem, K. H., and Sheth, M. R., 2021, “Variables Affecting Patellar Height in Patients Undergoing Primary Total Knee Replacement,” Int. Orthop., 45(6), pp. 1477–1482.

Salvadore, G., Meere, P. A., Verstraete, M. A., Victor, J., & Walker, P. S. (2018). Laxity and contact forces of total knee designed for anatomic motion: a cadaveric study. The Knee, 25(4), 650-656.

Sarkalkan, N., Weinans, H., & Zadpoor, A. A. (2014). Statistical shape and appearance models of bones. Bone, 60, 129-140.

Schleifenbaum, S., Prietzel, T., Hädrich, C., Möbius, R., Sichting, F., & Hammer, N. (2016). Tensile properties of the hip joint ligaments are largely variable and age-dependent–An in-vitro analysis in an age range of 14–93 years. Journal of biomechanics, 49(14), 3437-3443.

Schwartz, A. M., Goel, R. K., Sweeney, A. P., & Bradbury Jr, T. L. (2021). Capsular management in direct anterior total hip arthroplasty: a randomized, single-blind, controlled trial. The Journal of Arthroplasty, 36(8), 2836-2842.

Scott, D. F., & Gray, C. G. (2022). Outcomes are better with a medial-stabilized vs a posterior-stabilized total knee implanted with kinematic alignment. The Journal of Arthroplasty, 37(8), S852-S858.

Seon, J. K., Song, E. K., Yoon, T. R., Bae, B. H., Park, S. J., & Cho, S. G. (2007). In vivo stability of total knee arthroplasty using a navigation system. International Orthopaedics, 31, 45-48.

Shahane, S. A., Ibbotson, C., Strachan, R., & Bickerstaff, D. (1999). The popliteofibular ligament: an anatomical study of the posterolateral corner of the knee. The Journal of Bone & Joint Surgery British Volume, 81(4), 636-642.

Shalhoub, S., Cyr, A., & Maletsky, L. P. (2022). Correlation between knee anatomy and joint laxity using principal component analysis. Journal of Orthopaedic Research®, 40(11), 2502-2509.

Shalhoub, S., Lawrence, J., Keggi, J., Randall, A., DeClaire, J., & Plaskos, C. (2019). Imageless, robotic-assisted total knee arthroplasty combined with a robotic tensioning system can help predict and achieve accurate postoperative ligament balance. Arthroplasty Today, 5(3), 334-340.

Sharkey, P. F., Hozack, W. J., Rothman, R. H., Shastri, S., and Jacoby, S. M., 2002, “Insall Award Paper. Why Are Total Knee Arthroplasties Failing Today?,” Clin. Orthop. Relat. Res., (404), pp. 7–13.

Sharkey, P., Lichstein, P., Shen, C., Tokarski, A., & Parvizi, J. (2014). Why Are Total Knee Arthroplasties Failing Today—Has Anything Changed After 10 Years?. The Journal of Arthroplasty, 29(9), 1774-1778.

Sharma, A., Leszko, F., Komistek, R. D., Scuderi, G. R., Cates, H. E., and Liu, F., 2008, "In Vivo Patellofemoral Forces in High Flexion Total Knee Arthroplasty," J. Biomech., 41(3), pp. 642–648.

Sheth, N. P., Husain, A., & Nelson, C. L. (2017). Surgical techniques for total knee arthroplasty: measured resection, gap balancing, and hybrid. JAAOS-Journal of the American Academy of Orthopaedic Surgeons, 25(7), 499-508.

Shoji, T., Yamasaki, T., Izumi, S., Kenji, M., Sawa, M., Yasunaga, Y., & Adachi, N. (2018). The effect of cup medialization and lateralization on hip range of motion in total hip arthroplasty. Clinical Biomechanics, 57, 121-128.

Siddiqi, A., White, P. B., Kaplin, L., Bono, J. V., & Talmo, C. T. (2018). Effects of coronal limb alignment and ligament balance on pain and satisfaction following total knee arthroplasty at short-term follow up. Surg Technol Int, 33, 271-276.

Singh, J. A., Yu, S., Chen, L., & Cleveland, J. D. (2019). Rates of total joint replacement in the United States: future projections to 2020–2040 using the national inpatient sample. The Journal of rheumatology, 46(9), 1134-1140.

Singh, Vinay Kumar, et al. "Functional outcome after computer-assisted total knee arthroplasty using measured resection versus gap balancing techniques: a randomised controlled study." Journal of orthopaedic surgery 20.3 (2012): 344-347.

Sintini, I., Fitzpatrick, C. K., Clary, C. W., Castelli, V. P., & Rullkoetter, P. J. (2018). Computational evaluation of TKR stability using feedback-controlled compressive loading. Journal of Orthopaedic Research, 36(7), 1901-1909.

Sintini, I., Fitzpatrick, C., Clary, C., Castelli, V., & Rullkoetter, P. (2018). Computational evaluation of TKR stability using feedback-controlled compressive loading. Journal of Orthopaedic Research, 36(7), 1901-1909.

Smith, C. R., Vignos, M. F., Lenhart, R. L., Kaiser, J., & Thelen, D. G. (2016). The influence of component alignment and ligament properties on tibiofemoral contact forces in total knee replacement. Journal of biomechanical engineering, 138(2), 021017.

Smoger, L. M., Fitzpatrick, C. K., Clary, C. W., Cyr, A. J., Maletsky, L. P., Rullkoetter, P. J., & Laz, P. J. (2015). Statistical modeling to characterize relationships between

knee anatomy and kinematics. Journal of Orthopaedic Research®, 33(11), 1620-1630.

Subramanian, P., Wainwright, T. W., Bahadori, S., & Middleton, R. G. (2019). A review of the evolution of robotic-assisted total hip arthroplasty. Hip International, 29(3), 232-238.

Suh, K. T., Park, B. G., & Choi, Y. J. (2004). A posterior approach to primary total hip arthroplasty with soft tissue repair. Clinical Orthopaedics and Related Research®, 418, 162-167.

Sun, X., Zhu, X., Zeng, Y., Zhang, H., Zeng, J., Feng, W., ... & Zeng, Y. (2020). The effect of posterior capsule repair in total hip arthroplasty: a systematic review and meta-analysis. BMC musculoskeletal disorders, 21(1), 1-11.

Suzuki, K., Hara, N., Mikami, S., Tomita, T., Iwamoto, K., & Yamazaki, T. et al. (2014). In vivo kinematic analysis of posterior-stabilized total knee arthroplasty for the valgus knee operated by the gap-balancing technique. The Knee, 21(6), 1124-1128.

Swanson, T. V., Kukreja, M. M., Ballard, J. C., Calleja, H. G., & Brown, J. M. (2019). The "capsular noose": A new capsular repair technique to diminish dislocation risk after the posterior approach total hip arthroplasty. International Journal of Surgery Open, 17, 8-14.

Takao, M., Nishii, T., Sakai, T., & Sugano, N. (2016). Postoperative limb-offset discrepancy notably affects soft-tissue tension in total hip arthroplasty. JBJS, 98(18), 1548-1554.

Tamaki, Y., Goto, T., Wada, K., Hamada, D., Tsuruo, Y., & Sairyo, K. (2020). Anatomic evaluation of the insertional footprints of the iliofemoral and ischiofemoral ligaments: a cadaveric study. BMC Musculoskeletal Disorders, 21(1), 1-8.

Tannast, M., Kubiak-Langer, M., Langlotz, F., Puls, M., Murphy, S.B., Siebenrock, K.A., 2007. Noninvasive three-dimensional assessment of femoroacetabular impingement. Journal of Orthopaedic Research 25, 122–131.

Taylor, M., Perilli, E., & Martelli, S. (2017). Development of a surrogate model based on patient weight, bone mass and geometry to predict femoral neck strains and fracture loads. Journal of biomechanics, 55, 121-127.

Teeter, M., Perry, K., Yuan, X., Howard, J., & Lanting, B. (2017). Contact Kinematic Differences Between Gap Balanced vs Measured Resection Techniques for Single

Radius Posterior-Stabilized Total Knee Arthroplasty. The Journal of Arthroplasty, 32(6), 1834-1838.

Telleria, J. J., Lindsey, D. P., Giori, N. J., & Safran, M. R. (2014). A quantitative assessment of the insertional footprints of the hip joint capsular ligaments and their spanning fibers for reconstruction. Clinical Anatomy, 27(3), 489-497.

Terrier, A., Latypova, A., Guillemin, M., Parvex, V., & Guyen, O. (2017). Dual mobility cups provide biomechanical advantages in situations at risk for dislocation: a finite element analysis. International orthopaedics, 41(3), 551-556.

Thatcher, J. C., Zhou, X. M., & Walker, P. S. (1987). Inherent laxity in total knee prostheses. The Journal of Arthroplasty, 2(3), 199-207.

Tischer, T., Geier, A., Lutter, C., Enz, A., Bader, R., and Kebbach, M., 2022, "Patella Height Influences Patellofemoral Contact and Kinematics Following Cruciate-Retaining Total Knee Replacement," J. Orthop. Res., (September 2021).

Tsutsumi, M., Nimura, A., Honda, E., Utsunomiya, H., Uchida, S., & Akita, K. (2019). An anatomical study of the anterosuperior capsular attachment site on the acetabulum. The Journal of Bone and Joint Surgery. American Volume, 101(17), 1554.

Twiggs, J., Miles, B., Roe, J., Fritsch, B., Liu, D., Parker, D., Dickison, D., Shimmin, A., BarBo, J., McMahon, S., Solomon, M., Boyle, R., & Walter, L. (2021). Can TKA outcomes be predicted with computational simulation? Generation of a patient specific planning tool. The Knee, 33, 38–48.

Unitt, L., Sambatakakis, A., Johnstone, D., & Briggs, T. W. R. (2008). Short-term outcome in total knee replacement after soft-tissue release and balancing. The Journal of bone and joint surgery. British volume, 90(2), 159-165.

Unwin, A. (2010). (iii) What's new in anterior cruciate ligament surgery?. Orthopaedics and Trauma, 24(2), 100-106.

Vajapey, S. P., Fideler, K. L., Lynch, D., & Li, M. (2020). Use of dual mobility components in total hip arthroplasty: indications and outcomes. Journal of Clinical Orthopaedics and Trauma, 11, S760-S765.

van Arkel, R. J., Amis, A. A., & Jeffers, J. R. (2015). The envelope of passive motion allowed by the capsular ligaments of the hip. Journal of Biomechanics, 48(14), 3803-3809.

Van Arkel, R. J., Amis, A. A., Cobb, J. P., & Jeffers, J. R. T. (2015). The capsular ligaments provide more hip rotational restraint than the acetabular labrum and the ligamentum teres: an experimental study. The bone & joint journal, 97(4), 484-491.

van Arkel, R. J., Ng, K. G., Muirhead-Allwood, S. K., & Jeffers, J. R. (2018). Capsular ligament function after total hip arthroplasty. The Journal of Bone and Joint surgery. American Volume, 100(14), e94.

Van Oevelen, A., Duquesne, K., Peiffer, M., Grammens, J., Burssens, A., Chevalier, A., ... & Audenaert, E. (2023). Personalized statistical modeling of soft tissue structures in the knee. Frontiers in Bioengineering and Biotechnology, 11, 1055860.

Vandeputte, F. J., Vanbiervliet, J., Sarac, C., Driesen, R., & Corten, K. (2021). Capsular resection versus capsular repair in direct anterior approach for total hip arthroplasty: a randomized controlled trial. The Bone & Joint Journal, 103(2), 321-328.

Victor, J., Banks, S., & Bellemans, J. (2005). Kinematics of posterior cruciate ligament-retaining and-substituting total knee arthroplasty: a prospective randomised outcome study. The Journal of Bone & Joint Surgery British Volume, 87(5), 646-655.

Wagner, F. V., Negrão, J. R., Campos, J., Ward, S. R., Haghighi, P., Trudell, D. J., & Resnick, D. (2012). Capsular ligaments of the hip: anatomic, histologic, and positional study in cadaveric specimens with MR arthrography. Radiology, 263(1), 189-198.

Wagner, H., Boström, K. J., de Lussanet, M. H. E., de Graaf, M. L., Puta, C., and Mochizuki, L., 2022, “Optimization Reduces Knee-Joint Forces During Walking and Squatting: Validating the Inverse Dynamics Approach for Full Body Movements on Instrumented Knee Prostheses,” Motor Control, pp. 1–18.

Ward, S. R., Terk, M. R., and Powers, C. M., 2005, “Influence of Patella Alta on Knee Extensor Mechanics,” J. Biomech., 38(12), pp. 2415–2422.

Warren, L. F., & Marshall, J. L. (1979). The supporting structures and layers on the medial side of the knee: an anatomical analysis. Jbjs, 61(1), 56-62.

Weisse, B., Aiyangar, A. K., Affolter, C., Gander, R., Terrasi, G. P., & Ploeg, H. (2012). Determination of the translational and rotational stiffnesses of an L4–L5 functional spinal unit using a specimen-specific finite element model. Journal of the mechanical behavior of biomedical materials, 13, 45-61.

Whiteside, L. (2002). Soft tissue balancing: The knee. The Journal of Arthroplasty, 17(4), 23-27.

Willing, R., & Walker, P. (2018). Measuring the sensitivity of total knee replacement kinematics and laxity to soft tissue imbalances. Journal of Biomechanics, 77, 62-68.

Willing, R., Moslemian, A., Yamomo, G., Wood, T., Howard, J., and Lanting, B., 2019, "Condylar-Stabilized TKR May Not Fully Compensate for PCL-Deficiency: An In Vitro Cadaver Study," J. Orthop. Res., 37(10), pp. 2172–2181.

Winemaker, M. (2002). Perfect balance in total knee arthroplasty: The elusive compromise. The Journal of Arthroplasty, 17(1), 2-10.

Wingstrand, H., & Wingstrand, A. (1997). Biomechanics of the hip joint capsule -- a mathematical model and clinical implications. Clinical biomechanics (Bristol, Avon), 12(5), 273–280.

Wittek, A., Grosland, N. M., Joldes, G. R., Magnotta, V., & Miller, K. (2016). From finite element meshes to clouds of points: a review of methods for generation of computational biomechanics models for patient-specific applications. Annals of biomedical engineering, 44, 3-15.

Wyles, C. C., Maradit-Kremers, H., Larson, D. R., Lewallen, D. G., Taunton, M. J., Trousdale, R. T., ... & Sierra, R. J. (2022). Creation of a total hip arthroplasty patient-specific dislocation risk calculator. JBJS, 104(12), 1068-1080.

Yang, J. S., Fulkerson, J. P., Obopilwe, E., Voss, A., Divenere, J., Mazzocca, A. D., and Edgar, C. M., 2017, "Patellofemoral Contact Pressures After Patellar Distalization: A Biomechanical Study," Arthrosc. - J. Arthrosc. Relat. Surg., 33(11), pp. 2038–2044.

Yue, B., Varadarajan, K. M., Rubash, H. E., & Li, G. (2012). In vivo function of posterior cruciate ligament before and after posterior cruciate ligament-retaining total knee arthroplasty. International orthopaedics, 36, 1387-1392.

Zavatsky, A. B. (1997). A kinematic-freedom analysis of a flexed-knee-stance testing rig. Journal of biomechanics, 30(3), 277-280.

Zaylor, W., Stulberg, B. N., & Halloran, J. P. (2019). Use of distraction loading to estimate subject-specific knee ligament slack lengths. Journal of biomechanics, 92, 1-5.

Zhang, J., Malcolm, D., Hislop-Jambrich, J., Thomas, C. D. L., & Nielsen, P. M. (2014). An anatomical region-based statistical shape model of the human femur. Computer Methods in Biomechanics and Biomedical Engineering: Imaging & Visualization, 2(3), 176-185.

Zhang, R. Y., Su, X. Y., Zhao, J. X., Li, J. T., Zhang, L. C., & Tang, P. F. (2020). Three-dimensional morphological analysis of the femoral neck torsion angle—an anatomical study. Journal of Orthopaedic Surgery and Research, 15(1), 1-8.

Ziaeipoor, H., Martelli, S., Pandy, M., & Taylor, M. (2019). Efficacy and efficiency of multivariate linear regression for rapid prediction of femoral strain fields during activity. Medical Engineering & Physics, 63, 88-92.

Ziegler, J. G., and Nichols, N. B., 1993, "Optimum Settings for Automatic Controllers," J. Dyn. Syst. Meas. Control. Trans. ASME, 115(2B), pp. 220–222.

Zijlstra, W. P., De Hartog, B., Van Steenbergen, L. N., Scheurs, B. W., & Nelissen, R. G. (2017). Effect of femoral head size and surgical approach on risk of revision for dislocation after total hip arthroplasty: An analysis of 166,231 procedures in the Dutch Arthroplasty Register (LROI). Acta orthopaedica, 88(4), 395-401.